ALMA MATER STUDIORUM · UNIVERSITÀ DI BOLOGNA

FACOLTÀ DI SCIENZE MATEMATICHE, FISICHE E NATURALI
Corso di Laurea Magistrale in Fisica del Sistema Terra

Characterisation and calibration of optical counters for airborne particulate matter

Relatore:
Prof. Vincenzo Levizzani

Presentata da:
Agostino Rappazzo

Co-relatori:
Dott. Franco Belosi
Dott. Fabrizio Ravegnani

I Sessione
Anno Accademico 2014-2015

Sommario

Con il termine aerosol, o particolato ambientale (PM), si definisce una sospensione colloidale di particelle solide o liquide in aria. Gli aerosol sono parte integrante dell'atmosfera, hanno un ruolo importante in diversi processi atmosferici e influenzano il clima terrestre e la salute umana con effetti di diminuzione dell'aspettativa di vita. E' pertanto di primaria importanza il loro monitoraggio in tempo reale in termini di concentrazione e distribuzione dimensionale.

I contatori ottici di particolato ambientale (OPC) sono largamente usati in monitoraggi in ambienti sia outdoor che indoor. Si basano sullo scattering di un fascio luminoso collimato per classificare le particelle e fornire concentrazioni in numero di aerosol in tempo reale. Misurano dimensionalmente particelle di dimensioni comprese tra 0.3 e 20 μm e concentrazioni in numero fino a 10^7 # L^{-1}. Recenti progressi nella tecnica hanno permesso la commercializzazione di OPC portatili di dimensione e costo ridotti; tali strumenti sono adatti per valutazioni di esposizione personale al particolato ambientale, nonché per implementare reti di monitoraggio diffuse (smart cities).

Gli OPC richiedono calibrazioni frequenti, che vengono solitamente effettuate producendo aerosol di dimensione controllata e testando la risposta dell'OPC da calibrare con uno strumento di riferimento (ad esempio, uno strumento già calibrato) o con valori assoluti di concentrazione ottenuti tramite osservazione diretta di particelle tramite un microscopio elettronico a scansione (SEM).

Gli obiettivi di questo lavoro sono:

1) la caratterizzazione delle prestazioni di un OPC di nuova concezione (CompactOPC N1, prodotto da Alphasense; in seguito COPC) confrontando l'output con quello di un OPC standard commerciale (Portable Laser Aerosolspectrometer Dust Monitor Model 1.108, prodotto da GRIMM AEROSOL Technik GmbH & Co.; in seguito GRM);

2) la realizzazione di un banco di prova per la calibrazione di un OPC utilizzato in camere bianche e ambienti sanitari (Laser Particle Sensor mod. 3715-00, prodotto da Kanomax; in seguito LPS).

La ditta Pollution Clean Air Systems S.p.A (Budrio, BO), il distributore italiano del LPS, è interessata a effettuare la calibrazione di tale OPC per i propri clienti, dal momento che tale attività non viene effettuata in Italia. Pertanto, la ditta ha manifestato interesse per i risultati di questo lavoro per migliorare potenzialmente il proprio servizio ai clienti.

Le prove sono state effettuate con aerosol indoor e con particelle monodisperse di latex polistirene (PSL) di dimensioni differenti campionando in parallelo con i diversi OPC e su filtro per osservazioni al SEM. In questo modo si è ottenuto un valore assoluto di riferimento per la concentrazione di aerosol. I risultati indicano un buon accordo tra il GRM e i dati ottenuti dalle analisi al SEM, confermando pertanto una buona affidabilità del setup sperimentale e del GRM. Dai risultati si evince anche che se munito di una pompa, invece che di una ventola come nella configurazione standard, il COPC fornisce le migliori prestazioni.

Per il secondo scopo, il LPS è stato calibrato generando aerosol monodisperso e confrontando l'output con quello di un altro LPS calibrato di recente.

Il lavoro sperimentale relativo a questa tesi è stato effettuato presso il Laboratorio di Aerosol e Fisica delle Nubi dell'Istituto di Scienze dell'Atmosfera e del Clima (ISAC) del Consiglio Nazionale delle Ricerche (CNR) a Bologna.

Abstract

The term aerosol, or particulate matter (PM), defines a colloidal mixture where liquid and solid particles are suspended in the air. Aerosols are therefore an integral part of the atmosphere, play an important role in most of the atmospheric processes and affect the Earth's climate and human health with decreases in life expectancy. Therefore, it is of primary importance to monitor aerosol concentrations and size distributions on a real-time basis.

Optical Particle Counters (OPCs) are widely used for monitoring outdoor and indoor ambient air. They rely upon light scattering to classify aerosol particles and return particle number concentrations on a real-time basis. They can measure particle sizes from 0.3 up to 20 μm and particle number concentrations up to 10^7 # L^{-1}. Recent progresses in technique have allowed the commercialisation of smaller, cheaper and portable OPCs, which are well suited for personal exposure assessment to airborne particles or for diffused monitoring networks (e.g., smart cities). OPCs require frequent calibrations, which are usually performed by producing aerosol particles of controlled size and testing the response of the OPC under calibration against a reference device (which may be a calibrated instrument) or against absolute particle concentration values obtained by means of direct observation of particles at a scanning electron microscope (SEM)

The aims of this work are:

1) to characterise the performances of a novel OPC (CompactOPC N1, produced by Alphasense; hereafter COPC) against a standard commercial OPC (Portable Laser Aerosolspectrometer Dust Monitor Model 1.108, produced by GRIMM AEROSOL Technik GmbH & Co.; hereafter GRM);

2) to build up a test bench for calibrating an OPC used in clean room and sanitary environments (Laser Particle Sensor mod. 3715-00, produced by Kanomax; hereafter LPS).

Pollution Clean Air Systems S.p.A (Budrio, BO), the Italian distributor of the LPS, is keen on carrying out the calibration of the LPS, since such activity is not performed in

Italy. Therefore, the company is interested in the results of this work as a potential improvement of its customer service.

Tests were carried out with both indoor and monodisperse polystyrene latex (PSL) particles of several sizes and sampling in parallel with the different OPCs and, furthermore, collecting particles on a filter for SEM observation, thus obtaining an absolute reference value for the aerosol concentration. Results indicated a good agreement between the GRM's output and data obtained from SEM analysis, thus ensuring a good reliability of the experimental setup and the GRM; they also showed that, when equipped with a pump, instead of the fan as in the standard configuration, the COPC provided the best performances.

For the second aim the LPS was calibrated by generating monodisperse aerosol and testing the output against another LPS device recently calibrated.

The experimental work relating to this dissertation project was carried out in the Laboratory for Aerosol and Cloud Physics of the Institute for Atmospheric and Climate Science (ISAC) at the Italian National Research Council (CNR) in Bologna.

Table of contents

Sommario III

Abstract V

Table of contents VII

List of figures XI

List of tables XV

Introduction 1

Chapter 1: Aerosol sources and properties 5

1.1 Introduction 5

1.2 Atmospheric aerosol 7

1.2.1 Natural aerosol 7

1.2.1.1 Marine aerosol 8

1.2.1.2 Mineral dust 9

1.2.1.3 Volcanic ash 10

1.2.1.4 Primary Biological Aerosol Particles (PBAP) 11

1.2.2 Anthropogenic aerosol 12

1.2.3 Background and secondary aerosol 12

1.3 Indoor aerosol 14

1.4 Aerosol effects 15

1.4.1 Climate effects 15

1.4.2 Health effects 17

Chapter 2: Aerosol physics and applications 25

2.1 Aerosol mechanics and behaviour 25

2.1.1 Ideal gas law and Reynolds number 25

2.1.2 Stokes's resistance law, Stokes number and settling velocity 27
2.1.3 Brownian diffusion 32
2.2 Aerosol optics 33
2.2.1 Aerosol scattering 34
2.2.2 Extinction and Beer law 37
2.3 Aerosol filtration and deposition 39
2.3.1 Filtration 39
2.3.2 Pulmonary deposition 43
2.4 Measurement devices for aerosol size: impactors, electrostatic precipitators, mobility analysers 46
2.4.1 Impactors 46
2.4.2 Electrostatic precipitators 49
2.4.3 Mobility analysers 50
2.5 Light scattering instruments 51
2.5.1 Photometers 52
2.5.2 Optical Particle Counters (OPCs) 52
2.5.2.1 Measurement principle 52
2.5.2.2 Critical aspects 53
2.5.2.3 Applications 55
2.5.3 Microscopy 56

Chapter 3: Materials and methods 59
3.1 Aerosol generation 59
3.2 Aerosol generators used for this study 61
3.3 Optical Particle Counters used for this study 63
3.4 Reference method 67
3.4.1 Description 67
3.4.2 Particle concentrations obtained through SEM observations 68
3.4.3 Reading out the number concentration from the OPCs 69
3.5 Data handling 70
3.5.1 The lognormal distribution 70
3.5.2 Normalised histograms 71

Chapter 4: Experimental results 73
4.1 Indoor measurements 73
4.1.1 Background concentration 73
4.1.2 Samplings in indoor environment 74
4.2 Response time 80
4.3 Measurements with PSL particles 81
4.3.1 Experimental setup 82
4.3.2 Tests with 0.5 μm calibrated particles 82
4.3.3 Test with 0.95 μm PSL 88
4.3.4 Generating PSL with the AGK 2000 aerosol generator 93
4.4 Simulation of an indoor campaign 98
4.5 Conclusions 104

Chapter 5: Building up a test bench for calibrating the LPS counter 105
5.1 Standard practice for OPC calibration: procedure 105
5.2 Experimental part 106
5.2.1 Flow calibration 107
5.2.2 Counting efficiency 110
5.3 Conclusions 113

Conclusions 115

List of acronyms 117

Bibliography 119

Acknowledgements 123

List of figures

1.1: Particulate matter size distribution (from Hinds, 1999). 6

1.2: Yearly average aerosol optical thickness over Europe (at 0.55 μm) measured by MODIS (from Koelemeijer, 2006). 6

1.3: Major types, sources and mass burdens of particulate matter (adapted from Andreae and Rosenfeld, 2008). 7

1.4: Marine aerosol formation: picture of bubble bursting (1.4a) and schematic (1.4b). 9

1.5: Example of Saharan dust transport as reported by the Moderate Resolution Imaging Spectroradiometer (MODIS) on 16th July 2003. 10

1.6: Volcanic ash being erupted by Eyjafjallajökull (Iceland) in April 2010. 11

1.7: Schematic description of secondary aerosol formation and processing in the marine environment (from Quinn and Bates, 2011). 14

1.8: Global mean radiative forcings as estimated by the fifth Assessment Report of the Intergovernmental Panel for Climate Change (IPCC) in 2013. 17

1.9: Atmospheric aerosol particle modes (adapted from Hinds, 1999). 20

1.10: Potential general pathophysiological pathways linking PM exposure with cardiopulmonary morbidity and mortality (from Pope and Dockery, 2006). 22

1.11: Average $PM_{2.5}$ (left) and predicted average gain in life expectancy (months) for persons 30 years of age and older in 25 Aphekom cities for a decrease in the average annual level of PM2.5 to 10 μg m^{-3} (right). Picture from Aphekom (2011). 22

1.12: Percentage of population with chronic diseases due to living near busy streets and roads in 10 Aphekom cities (from Aphekom, 2011). 23

2.1: Variation of the drag coefficient with the particle Reynolds number (adapted from Hinds, 1999). 28

2.2: Schematic of an impactor. Adapted from Vincent (1989). 31

2.3: Particle dispersion due to Brownian motion (from Hinds, 1999). 33

2.4: Difference in visibility due to different aerosol concentrations in Beijing. 34

2.5: Schematic of scattered light including scattering angle, scattering plane and polarised components (i_1 and i_2). Adapted from Hinds (1999). 34

2.6: Mie intensity parameters versus scattering angle for water droplets (m=1.33) having α=0.8, 2.0 and 10.0 (adapted from Hinds, 1999). 37

2.7: Relative scattering (Mie intensity parameter: i_1+i_2) versus size parameter for water droplets (m=1.33) at scattering angles of 30° and 90° (adapted from Hinds, 1999). 37

2.8: Extinction efficiency versus particle size (adapted from Hinds, 1999). 39

2.9: Capture by interception (from Hinds, 1999). 42

2.10: Capture by impaction (from Hinds, 1999). 42

2.11: Capture by diffusion (from Hinds, 1999). 42

2.12: Filter efficiency versus particle size for different face velocities, t = 1 mm, $\alpha = 0.05$ and d = 2 μm (from Hinds, 1999). 43

2.13: Predicted alveolar, tracheo-bronchial, head airways and total deposition for light exercise (nose breathing) based on a deposition model (from Hinds, 1999). 45

2.14: American conference of governmental industrial hygenists sampling criteria for inhalable, thoracic and respirable fractions (adapted from Hinds, 1999). 45

2.15: Particle deposition along the respiratory apparatus. 46

2.16: Example of an impactor cutoff curve: it represents the plot of the impactor's collection efficiency versus the square root of Stk (from Hinds, 1999). 47

2.17: Schematic of a cascade impactor (from Hinds, 1999). 48

2.18: Schematic of a virtual impactor (from Hinds, 1999). 48

2.19: PM sampling station. 49

2.20: Schematic of a Differential Mobility Analyser (from Hinds, 1999). 51

2.21: Scanning Mobility Particle Sizer. 51

2.22: Schematic of an OPC. Adapted from Colombi et al. (2012). 53

2.23: Theoretical response and experimental calibration curve of the Bausch and Lomb 40-1A particle counter (from Liu, 1976). 55

3.1: Diagram of the DeVilbiss mod. 40 nebuliser. Adapted from Hinds (1999). 60

3.2: Projet aerosol generator, Artsana S.p.a. 62

3.3: AGK 2000 aerosol generator, Palas GmbH. 63

3.4: Schematic of AGK 2000, Palas GmbH. 63

3.5: Portable Laser Aerospectrometer Dust Monitor. 65

3.6: Compact OPC N1, Alphasense. 66

3.7: Laser Particle Sensor mod. 3715-00, Kanomax. 67

4.2: Experimental setup for measuring the background concentration in clean air conditions. 73

4.3: Schematic of Test 1. 75

4.3: Particle size distribution as read out from the COPC during Test 2. 75

4.4: Same as Figure 4.3, read out from the GRM. 76

4.5: Experimental setup of Test 4, 5 and 6 76

4.6: Trend of the LPS/GRM ratio in the 0.5-5 μm size range versus the particle number concentration recorded by the GRM during different tests. 77

4.7: Same as Figure 4.6, for COPC/GRM ratio. 78

4.8: Same as Figure 4.7, in the 0.4-0.5 μm size range. 78

4.9: Same as Figure 4.6, for COPC/LPS ratio. 79

4.10: Diagram of the experimental apparatus. 82

4.11: Experimental setup. 83

4.12: Particular of a filter's sample. 83

4.13: PSL particle size distribution as read out from the GRM in different channels. 85

4.14: Same as Figure 4.12, for the following test. 86

4.15: Averaged particle size distribution reported by the GRM during the generation of 0.5 μm PSL spheres. 86

4.16: Same as Figure 4.15, reported by the COPC. 87

4.17: Plot of the COPC/GRM ratio in the 0.4-0.5 um size range as a function of the PSL number concentration measured by the GRM in the same range during tests with 0.5 μm PSL. 88

4.18: sample of a stub: a PSL particle of 1 μm in size. 89

4.19: 0.95 μm PSL size distribution as read out from the GRM. 90

4.20: Averaged particle size distribution reported by the COPC during the generation of 0.95 μm PSL spheres. 91

4.21: Same as Figure 4.20, reported by the GRM. 91

4.22: Plot of the normalised particle number concentations reported by the COPC and the GRM as read out from each channel against the corresponding particle size during the test with 0.5 μm PSL spheres conducted with the Projet nebuliser. 92

4.23: Same as Figure 4.22, during tests with 0.95 μm PSL spheres. 92

4.24: LPS, COPC and GRM during the sampling. 93

4.25: 0.5 μm PSL particle size distribution achieved with the AGK 2000 generator as reported by the GRM. 94

4.26: Same as Figure 4.25, reported by the COPC. 94

4.27: Same as 4.17, with results from the AGK 2000 generator too. 95

4.28: 1.03 μm PSL particle size distribution achieved with the AGK 2000 generator as reported by the COPC. 95

4.29: Same as Figure 4.28, reported by the GRM. 96

4.30: Same as Figure 4.22, during tests conducted with the AGK 2000 generator. 97

4.31: Same as Figure 4.23, during tests conducted with the AGK 2000 generator. 97

4.32: Time-series of the particle number concentrations in the 0.4-5 um size range during Test A. 99

4.33: Scatterplot of the GRM output against the COPC output for the 0.5-5 um size range during Test A. 99

4.34: Same as Figure 4.32, during Test B. 100

4.35: Same as Figure 4.33, during Test B. 101

4.36: Time-series of the particle number concentrations in the 1-5 um size range during Test A. 102

4.37: Same as Figure 4.36, during Test B. 102

4.38: Scatterplot of COPC/GRM as a function of the GRM particle number concentration during Test A for the 0.4-5 μm size range. 103

4.39: Same as Figure 4.38, during Test B. 103

5.1: Electronic components of the Laser Particle Sensor mod. 3715-00. 107

5.2: Measuring the voltage between TP3 and TP GND (V_3). 108

5.3: Laser Particle Sensor mod. 3715-00 connected to mini-BUCK calibrator mod. M-5. 109

5.4: Particular of the LPS's internal circuit: pins. 110

5.5: Experimental setup for the calibration of the LPS's counting efficiency. 112

5.6 Plot of the counting efficiency against V_{PIN2} for the 0.5-5 μm size range while generating 0.5μm PSL spheres. 113

List of tables

1.1: EU Standards for Particulate Matter for PM10 and PM2.5 (from Air Quality Standards). 18

3.1: Specifics of the Portable Laser Aerospectrometer Dust Monitor. 65

3.2: Channel division of the Portable Laser Aerospectrometer Dust. 65

3.3: Specifics of the CompactOPC N1, Alphasense. 66

3.4: Channel division of the Compact OPC N1, Alphasense. 66

3.5: Specifics of the Laser Particle Sensor, mod. 3714-00 and 3715-00. 67

4.1: Particle number concentration measured by each OPC in clean air conditions. 73

4.2: Configuration setup of each indoor sampling. 74

4.3: Particle number concentrations as read out from each instrument in the 0.4-0.5 μm and 0.5-5 μm size ranges in each sampling. 77

4.4: Response times of each OPC in different size ranges. 81

4.5: Particle counts in each observed field of the three filter's samples. 84

4.6: Particle number concentrations measured by each OPC and obtained by counting the particles deposited onto the filter. 87

4.7: COPC/GRM, LPS/GRM and COPC/LPS ratios for the 0.4-0.5 μm and 0.5-5 μm size ranges during the nebulisation of PSL spheres of 0.5 μm in diameter. 87

4.8: Comparing the PSL number concentration evaluated from filter data with the ones read out from each OPC. 90

4.9: Particle number concentrations reported by each instrument in several size ranges during the test with 1.03 μm PSL spheres conducted with the AGK 2000 generator. 96

5.1: LPS's sample flow rate after the calibration: details on the single measurements. 109

5.2: Voltage output and note of each pin. 111

Introduction

The term aerosol, or particulate matter (PM), defines a colloidal mixture where liquid and solid particles are suspended in the air. Atmospheric aerosol particles, in particular, have different physical and chemical properties, which depend on sources and atmospheric transformation. Classifications of atmospheric aerosols are based on the particle size, the origin (i.e., where the aerosol was generated) and the source (i.e., whether it is a primary or a secondary aerosol). From the physical viewpoint the size, typically ranging from 0.001 up to 100 μm, is the most important parameter for the characterisation of an aerosol particle.

Atmospheric aerosols may be of natural or anthropogenic origin and may either be directly emitted by the source (primary aerosol) or result from chemical transformations in the atmosphere (secondary aerosol).

Marine aerosol, mineral dust, volcanic ash and primary biological particles are classified as natural aerosols. The main compositions of such aerosols are: inorganic salts (marine aerosol), crustal elements (mineral dust and volcanic ash), natural microorganisms such as fungi or spores (primary biological organic particles), nitrates and sulphates (volcanic ash).

Anthropogenic aerosols are the result of several human activities, such as agriculture, industrial processes, transports, waste disposal and heating systems. Such aerosols mostly contain carbon, sulphates, nitrates and mineral elements.

Secondary aerosols may be either organic or inorganic and are particles resulting from transformation processes of substances of both natural and anthropogenic origin.

Aerosols are also found in indoor environment: cigarette smoke, wood-burning stoves, kerosene heaters, carpets, pressed wood furniture and household cleaning products are typical sources of indoor aerosols. Particles from such sources are mostly composed by carbon, nitrogen and metals.

Aerosols play an important role in most of the atmospheric microphysical, chemical and photochemical processes, thus affecting the Earth's climate. Due to their sizes, aerosol interact with the incoming solar radiation, thus yielding the so-called aerosol's direct effect; as aerosols mostly scatter rather than absorb the solar radiation, the global net effect is a cooling at the Earth's surface. Aerosols can also act as condensation and ice

nuclei for cloud formation, thus changing their radiative properties and lifetime. This is called the aerosol's indirect effect.

Aerosols can be inhaled by the human airways apparatus and have therefore an important effect on human health, with decreases in life expectancy observed in places with huge aerosol concentrations, such as big cities. Smaller particles are associated with the strongest impairing effects as they can penetrate inside the airways system more deeply than coarse particles. Therefore, it is of primary importance to monitor aerosol concentration and size distribution on a real-time basis to assess their effects on both climate and human health.

Optical Particle Counters (OPCs) can classify particles from 0.3 μm up to 20 μm; they rely upon light scattering to measure particle size distributions and particle number concentrations (i.e., particles amount per unit volume) on a real-time basis. As they are small and handy, they are widely used for sampling aerosols.

New generation OPCs are even smaller and cheaper with respect to the traditional devices deployed so far in air quality studies and are therefore best suited for personal exposure assessment to particulate and for indoor aerosol characterisation. They might also be used in participatory monitoring networks or in distributed sensor networks (smart cities).

However, OPCs require frequent calibrations, which are usually performed by producing aerosol particles of controlled size by means of a nebuliser and testing the response of the OPC against a reference device (which may be a calibrated instrument) or against an absolute particle concentration value. The latter is obtained by directly counting particles deposited onto filters sampling in parallel to the OPC at a Scanning Electron Microscope (SEM).

The aims of this thesis are:

1) to characterise a novel OPC (CompactOPC N1, produced by Alphasense; hereafter COPC) in terms of counting efficiency and size classification against a standard commercial OPC (Portable Laser Aerosolspectrometer Dust Monitor Model 1.108, produced by GRIMM AEROSOL Technik GmbH & Co.; hereafter GRM);

2) to set up a test bench for calibrating an OPC used in clean room and sanitary environments (Laser Particle Sensor mod. 3715-00, produced by Kanomax; hereafter LPS).

The LPS is distributed in Italy by Pollution Clean Air Systems S.p.A and at the present day its calibration is not carried out in Italy. Pollution Clean Air Systems S.p.A (Budrio, BO) is keen on carrying out this activity for its customers. Therefore, the company is interested in the results of this work as a potential improvement of its customer service and as an example of cooperation between research centres and small or medium enterprises.

The work is divided in five chapters. Chapter 1 provides a summary of aerosol sources and the effects of aerosols on climate and human health. Chapter 2 includes a review of aerosol physics and instrumentation for measuring and characterising aerosol particles, with a special focus on OPCs. Chapter 3 deals with the instrumentation used to perform the experimental part of the work: aerosol generators, OPCs used in the research and SEM analysis protocol are described. The methodology to determine mean values and experimental errors from OPC and SEM output is also provided. In Chapter 4 results are shown for tests with indoor aerosol and calibrated aerosol particles. An improvement of deploying the COPC in terms of aerosol sampling efficiency is also included. Finally, Chapter 5 provides details and experimental results for the calibration bench of the LPS.

Chapter 1: Aerosol sources and properties

1.1 Introduction

The term aerosol defines a colloidal mixture where liquid and solid particles are suspended in a gas. Atmospheric aerosol particles, in particular, have different physical and chemical properties (size, shape, chemical composition, refractive index, etc…), which depend on sources and atmospheric transformation.

From the physical viewpoint the size is the most important parameter for the characterisation of a particle. Particle sizes can range from 0.001 up to 100 μm, which accounts for five magnitude orders between the smallest and the biggest particles. The common reference for particle size is the particle *diameter* (Hinds, 1999).

The concentration of aerosols in the atmosphere can be defined as *particle mass concentration* (the total mass of the particles per air unit volume, expressed in $\mu g\ m^{-3}$), or *particle number concentration* (the number of particles per unit volume).

Common classifications of the aerosol particles are in terms of particle size, origin (i.e., where the aerosol was generated) and source (i.e., whether it is a primary or a secondary aerosol). Nevertheless further classifications may exist if required in special problems.

Figure 1.1 reports the size of some of the main aerosol types and provides insight into their relative weight in contributing to the total particulate mass fraction. Figure 1.2 reports the yearly average aerosol optical thickness at $\lambda = 0.55$ μm over Europe as measured by the Moderate-Resolution Image Spectroradiometer (MODIS). As the picture suggests, the greatest aerosol emissions are mostly correspondent to industrialised areas (e.g., the Po Valley) and deserts. The main types, sources and mass burdens of particulate matter are finally summarised in Figure 1.3.

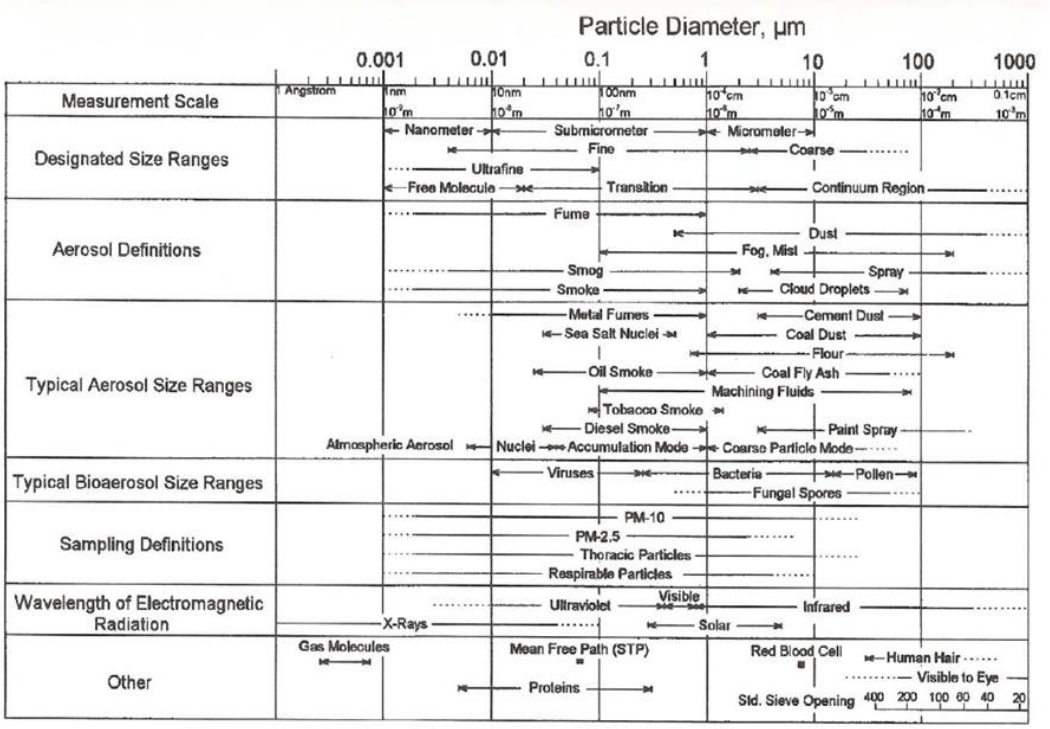

Figure 1.1: Particulate matter size distribution (from Hinds, 1999).

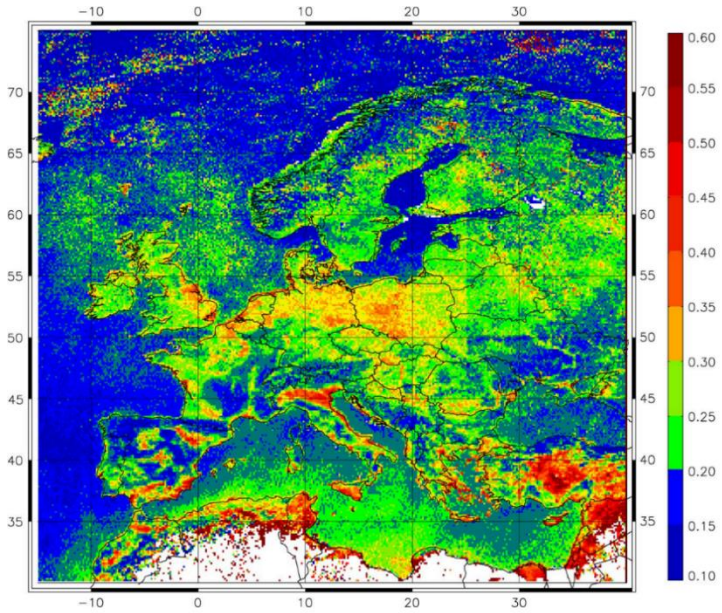

Figure 1.2: Yearly average aerosol optical thickness over Europe (at 0.55 µm) measured by MODIS in 2003. White: missing data. Picture from Koelemeijer et al. (2006).

	Mass emission			Mass Burden	Number Prod.	Number Burden
	"Best guess"	Min	Max			
		Tg a^{-1}		Tg	a^{-1}	
Carbonaceous aerosols						
Primary organic (0–2 µm)	95	40	150	1.2	–	$310 \cdot 10^{24}$
Biomass burning	54	26	70	–	$7 \cdot 10^{27}$	–
Fossil fuel	4	3	9	–	–	–
Biogenic	35	15	70	0.2	–	–
Black carbon (0–2 µm)	10	8	14	0.1	–	$270 \cdot 10^{24}$
Open burning and biofuel	6	5	7	–	–	–
Fossil fuel	4.5	3	6	–	–	–
Secondary organic	28	2.5	83	0.8	–	–
Biogenic	25	2.5	79	0.7	–	–
Anthropogenic	3.5	0.05	4.0	0.08	–	–
Sulfates	200	107	374	2.8	$2 \cdot 10^{28}$	–
Biogenic	57	28	118	1.2	–	–
Volcanic	21	9	48	0.2	–	–
Anthropogenic	122	69	214	1.4	–	–
Nitrates	18	12	27	0.49	–	–
Industrial dust, etc.	100	40	130	1.1	–	–
Sea salt						
$d<1$ µm	180	60	500	3.5	$7.4 \cdot 10^{26}$	–
$d=1–16$ µm	9940	3000	20,000	12	$4.6 \cdot 10^{26}$	–
Total	10,130	3000	20,000	15	$1.2 \cdot 10^{27}$	$27 \cdot 10^{24}$
Mineral (soil) dust						
<1 µm	165	–	–	4.7	$4.1 \cdot 10^{25}$	–
1–2.5 µm	496	–	–	12.5	$9.6 \cdot 10^{25}$	–
2.5–10 µm	992	–	–	6	–	–
Total	1600	1000	2150	18±5	$1.4 \cdot 10^{26}$	$11 \cdot 10^{24}$

Figure 1.3: Major types, sources and mass burdens of particulate matter (adapted from Andreae and Rosenfeld, 2008).

1.2 Atmospheric aerosol

Aerosols have either natural or anthropogenic sources and may either be emitted as primary particles (i.e., they are directly injected into the atmosphere) or result from secondary processes (i.e., by transformation of precursor gases).

1.2.1 Natural aerosol

The natural aerosol is commonly regrouped in four classes: marine aerosol, mineral dust, volcanic ash and primary biological aerosol particles (PBAP).

1.2.1.1 Marine aerosol

The marine aerosol is the aerosol confined in the marine boundary layer, mostly generated from sea spray. However, the marine environment also comprises other particles, such as sulphates from biogenic and anthropogenic sources (Andreae and Rosenfeld, 2008).

Sea salt or sea spray aerosols are generated by bubble bursting from breaking waves and capillary action at the ocean surface due to the stress exerted by the surface wind, which largely affects the production rate. The size of such particles ranges from the submicrometer interval up to some μm, the smallest particles being associated with film droplets (0.3 μm in diameter on average) and the biggest particles being associated with jet droplets (size greater than 2 μm). Figure 1.4b is a schematic of bubble bursting and shows the difference between film and jet droplets, while Figure 1.4a is a representation of the process.

The generated aerosol particles can scatter light and act as cloud condensation nuclei. Therefore, they may affect cloud physics and the radiation budget in the atmosphere. Furthermore, they interact with anthropogenic pollution and affect gas chemistry and biogeochemical cycles in marine and terrestrial ecosystems.

The primary component of sea spray is given by a mixture of inorganic salts, of which NaCl is the most prominent in mass concentration. An organic component is also present, coming from the sea surface and gas phase oxidation of volatile organic compounds (VOCs), that lead to formation of secondary organic aerosol.

Many organic compounds are found in the sea water, mostly originated by degradation of marine organisms and plants and therefore consists of amino- and fatty acids, carbohydrates, saccharides and cell fragments.

Marine aerosols can also serve as sink for reactive gases and small particles, as well as suppress new particle formation (Fuzzi, 2015).

Figure 1.4a: The wind's action causes bubble bursting at the sea surface and leads to the production of sea spray.

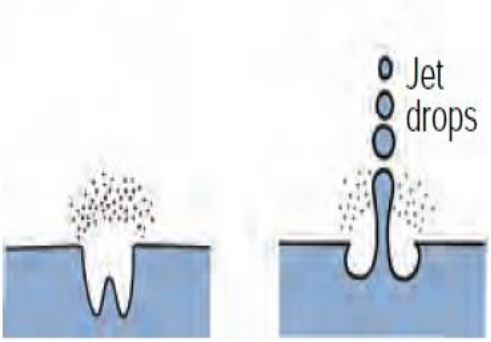

Figure 1.4b: Schematic of marine aerosol formation. Small particles (some tenths of µm on average) are associated with film drops (left), while big particles (some µm) are associated with jet drops (right).

1.2.1.2 Mineral dust

Mineral dust comprises all kinds of particles that are suspended in the atmosphere mostly originated by the action of the wind (erosion of rocks or updraft and transport of powders over long distances). According to Ginoux et al. (2012), this aerosol is mostly (75%) emitted by natural sources and the remaining part is due to anthropogenic emissions (primarily agricultural).

This kind of aerosol affects climate through direct and indirect effects, modifies marine biogeochemistry and affects human health. Specifically, the intrusion of Saharan dust accounts for some of the annual PM_{10} daily exceedances in Southern Spain and in general in the Mediterranean area (Rodriguez et al., 2001; Monks et al., 2008). Figure 1.5 shows an example of Saharan dust transport from Northern Africa to Southern Europe.

Typical components of mineral dust are crustal elements such as Fe, P, Na, Ba, Br, Mg, Al, K, Ca, Ti, Cu and V (Chen et al., 2008).

Aerosols in soil dust absorb visible radiation, thus yielding an atmospheric warming, while scattering by mineral dust leads to surface cooling Aerosols in soil dust absorb visible radiation, thus yielding an atmospheric warming, while scattering by mineral dust leads to surface cooling. These two processes affect climate and wind circulation on a regional scale through a reduction of downward mixing of momentum within the planetary boundary layer, the surface wind and, thus, dust emission (IPCC, 2013). As an example, atmospheric warming over the Sahara regions causes an intense heat pump effect that increases precipitation over the northern Sahel.

As mineral dust contains micronutrients like Fe and P, it intervenes in the ocean-carbon cycles, thus affecting the exchange of CO_2 and creating dust-climate feedback mechanisms.

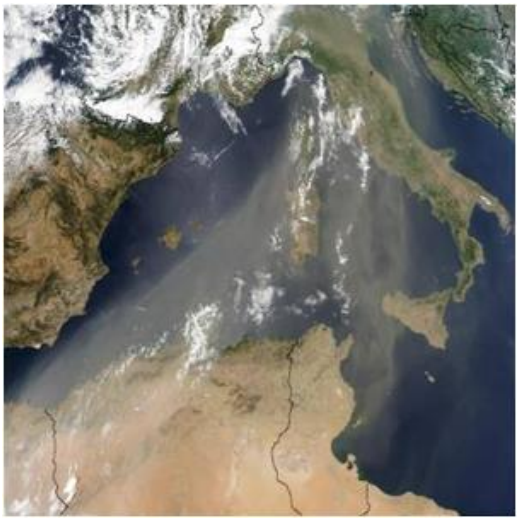

Figure 1.5: Example of Saharan dust transport as observed by the Moderate Resolution Imaging Spectroradiometer (MODIS) on 16th July 2003. This a clear demonstration of the combined action of the wind and the atmospheric circulation that may lead to severe outbreaks of Saharan dust towards Europe.

1.2.1.3 Volcanic ash

Volcanic ash is a particular type of mineral dust. It consists of pulverised materials (rocks, dust and volcanic glass) dispersed by explosive volcanic eruptions. Volcanic ash is formed when dissolved gases in magma expand and escape violently into the atmosphere, where they solidify and become aerosol.

Just like mineral dust, typical components of volcanic ash are crustal elements (mostly Ca, Na, Al and Fe), as well as nitrates and sulphates that are mainly suspended in the volcanic gases (Schleicher et al., 2010).

Volcanic dust from explosive eruptions is known to affect climate over periods ranging from a few months up to some year. During an explosive eruption, volcanic ash plumes can acquire velocities up to 100 m s^{-1}, reach the tropopause and enter the stratosphere.

An intense volcanic activity yields an increase in the atmospheric optical depth in the stratosphere, which results in a net cooling at the Earth's surface. Apart from large particles, which are removed by gravitational settling, most of the aerosol particles can remain in suspension above the tropopause for several months.

The atmospheric circulation can transport volcanic ash over long distances. For instance, some weeks after the Eyjafjallajökull (Iceland) eruption in 2010 (see Figure 1.6), PM measurements carried out in Bologna with a DMPS (see Chapter 2.4.3) and an OPC (see Chapter 2.5.2) revealed an increase in concentration of the accumulation and the coarse fraction during the transit of the ash cloud (Belosi et al., 2011).

The extent in time and space of a climate anomaly due to an eruption mostly depends on the amount of materials injected into the atmosphere, as well as where the eruption takes place. It is known that 1816 is considered "the year without summer" due to the eruption of Mount Tambora in 1815 (Stothers, 1984). Particularly in the northern hemisphere, the summer season was characterised by unusually low temperatures, often associated with severe weather events, in some cases snowfalls, like in New England (Canada).

Figure 1.6: Volcanic ash being erupted by Eyjafjallajökull (Iceland) in April 2010.

1.2.1.4 Primary Biological Aerosol Particles (PBAP)

PBAP includes components with a large range of size, such as microorganisms (bacteria, fungi, algae), fungal spores, pollen, viruses, biological fragments that are directly emitted to the atmosphere from their sources, as well as debris. Typical size ranges are: 0.05-0.15 µm for viruses, 0.1-4 µm for bacteria, 0.5-15 µm for fungal spores and 10-30 µm for pollen.

Bacteria and other bioaerosols may attach to other particles, be transported with them, and change the size distributions of such particles (Pastuszka et al., 2000).

PBAP intervene in ice nucleation and cloud drop formation and can affect climate and the hydrological cycle on regional and, perhaps, global scale. Moreover, they may cause harmful health effects (allergies, asthma, infectious diseases, etc.)

1.2.2 Anthropogenic aerosol

Anthropogenic aerosol can derive from: industrial processes, agricultural activity, transports (roads, ships, rail, air), and waste disposal. A significant part also derives from non-exhaust emissions, such as abrasion of tyre wear, brake wear, road wear and road dust suspension induced by road transport.

Exhaust particles mostly contain carbon compounds, sulphates and nitrates and are usually fairly smaller (they mostly account for the $PM_{2.5}$ mass fraction; see Chapter 1.4.2) compared to the non-exhaust ones. Instead, the latter mostly contain metals, metal oxides and mineral elements and present less carbonaceous material.

Wood combustion is a special case of exhaust emissions as it is mostly used for residential heating. Hence it gives an important contribution to the organic aerosol fraction and it is mostly responsible for high PM values in wintertime (e.g., Szidat et al., 2006). Most of these particles consists of highly soluble material and can therefore act as condensation nuclei.

Depending on the composition, the anthropogenic aerosol can either mostly absorb (as in the case of carbon compounds that account for the black carbon fraction) or scatter (nitrates and sulphates) solar radiation. Observations suggest that the net contribution to the radiation forcing is on average negative, although great uncertainties exist (Wang et al., 2013).

Datasets or inventories on each single source are not entirely available and are often incomplete as the amount of aerosol produced by such processes is not easy to evaluate and only partial estimates are available.

1.2.3 Background and secondary aerosol

The term secondary aerosol refers to the particles that are not directly injected into the atmosphere. Secondary aerosol can be inorganic and organic. Secondary inorganic aerosol is formed prevalently from oxidation reaction of NO_x and SO_2.

SO_2 sources can be anthropogenic and natural. Oxidation of SO_2 with formation of sulphuric acid can occur in the gas phase and in the liquid phase, e.g. cloud or fog.

Once formed in the atmosphere sulphuric and nitric acids show very different behaviour, both physically and chemically. Nitric acid is more volatile and hence exists in significant concentrations in the gas phase, while sulphuric acid has a very low vapour pressure. Once formed, vapour molecules rapidly transfer to the particulate phase by nucleation or condensation on existing aerosol surface. These processes are schematically represented in Figure 1.7.

Both sulphuric acid and nitric acid react with atmospheric ammonia. However gaseous ammonia first reacts with sulphuric acid to form ammonium bisulphate and ammonium sulphate, then the remaining free ammonia is depleted by reaction with nitric acid to form ammonium nitrate.

In addition to anthropogenic sources, in marine environment there is also a contribution to sulphates from the oxidation of dimethylsulphide (DMS) produced in seawater from the activity of various phyto- and zoo-planktonic species. Once released into the atmosphere DMS will follow an oxidation scheme controlled principally by hydroxyl radical ($OH^{\cdot}$) during the day and nitrate radical (NO_3) at night, thus producing sulphates and methanesulphonic acid (MSA). As a matter of a fact, MSA can be considered an indicator for DMS particulate oxidation products.

Secondary organic aerosol is formed in the atmosphere through reactions that transform volatile organic compounds (VOC) into low-vapour-pressure compounds, followed by condensation on existing particles, or by homogeneous nucleation (transition phase in the absence of a condensation nucleus).

The photochemical action of bright sunlight on nitrogen oxides (NO and NO_2) and VOCs leads to the formation of most of the ultrafine fraction. Both components are mostly of anthropogenic origin and the result of this process is called the photochemical smog and involves the interaction of sunlight with particles of different origins such as: exhaust emissions from vehicles and industries, forest fires, volcanic action, lightning, bacterial action in soil.

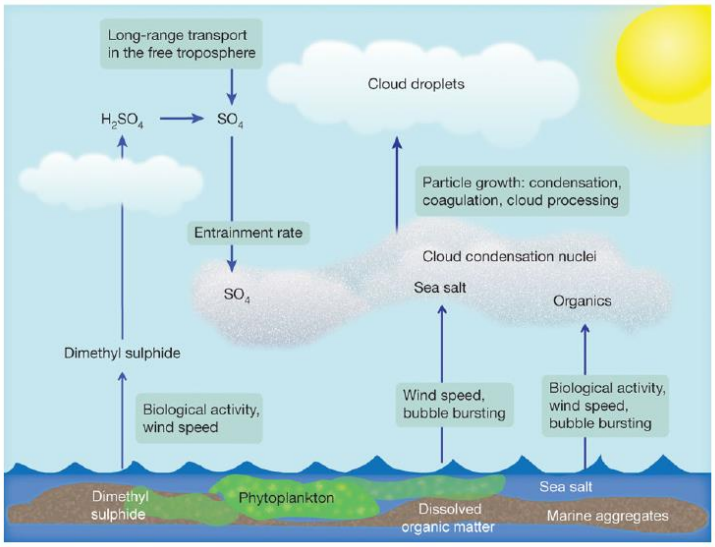

Figure 1.7: Schematic description of secondary aerosol formation and processing in the marine environment. Picture from Quinn and Bates (2011).

1.3 Indoor aerosol

The term indoor aerosol includes all kinds of suspended particulate matter that are found in indoor environments. In practice, the greatest difference between indoor and outdoor aerosol is given by the sources, while the chemical composition is often similar.

In developed countries, people spend most of their time indoors and several studies (Tan et al., 2012; Wang et al., 2007) have shown that indoor pollutant levels can be on average two to five times higher than their corresponding outdoor ones. As a matter of a fact, indoor air pollution is responsible for 2.7% of the total burden of disease and worldwide one million people per year die from pulmonary diseases due to the exposure to indoor smoke (Fang et al., 1999; Hetland et al., 2000).

Cigarette smoke, wood-burning stoves and kerosene heaters, carpets, pressed wood furniture and household cleaning products are typical sources of particulate matter in indoor environments (Daisey and Gundel, 1991; Tan et al., 2012). Emissions by these sources usually include organic carbon, elemental (black) carbon, nitrogen and metals (Fe, Na, Zn).

Bioaerosols such as fungi and bacteria are mostly found in mouldy and crowded environments: in conditions of high humidity rates and poor ventilation, microbiological

organisms can easily grow and develop (Pastuszka et al., 2000). Such particles are a major cause of respiratory diseases in indoor environments.

Ventilation and air-conditioning systems can favour microbial growth, while several types of microorganisms are used to produce pharmaceutical products, enzymes and food substitutes in commercial laboratories.

Indoor aerosol also includes biological emissions by plants, toner particles and suspensions from nebulising devices for medical or experimental (e.g., polystyrene latex) use. However, the most important sources of indoor particulate matter are probably cooking and heating. In particular, the exposure to indoor PM is higher in the dwellings of people with medium or low resources in developing countries, where solid fuels (biomass and coal) are widely deployed for cooking and heating purposes (Abdullahi et al., 2013).

Visible fumes are mostly submicrometer-sized particles mostly consisting of oil, combustion products, steam and condensed organic pollutants (Abdullahi et al., 2013); other products are volatile organic and nitrogen-related aerosols (Daisey and Gundel, 1991). The particulate matter relative to cooking processes is mostly in the ultrafine (less than 100 nm in diameter) and fine (aerodynamic diameter smaller than 2.5 μm) particle range. Particles from indoor combustion are a major cause of pulmonary diseases and most of them also possess mutagenic properties (Daisey and Gundel, 1991).

1.4 Aerosol effects

1.4.1 Climate effects

As already mentioned, aerosols are an integral part of the atmosphere and play an important role in most of the atmospheric microphysical, chemical and photochemical processes. Several feedback mechanisms are therefore established, most of which are complex and currently not fully understood.

Due to their sizes, aerosols interact with both longwave (LW) and shortwave (SW) radiation. In particular, they can always scatter and, in some cases, also absorb the incoming radiation. Physical properties of particles, like the extinction coefficient and the scattering phase function, depend on the wavelength of the incoming radiation and on the

atmospheric relative humidity, while the atmospheric loading and the geographic distribution of aerosols are determined by the atmospheric dynamics. As the result in terms of incoming radiation is directly determined by the interaction between aerosols and solar radiation, this is called the *aerosol's direct effect*.

Scattering aerosols always exert a negative radiative forcing (i.e., they cause a decrease in the incoming solar radiation at the ground, thus inducing a decrease in the temperature), while absorbing aerosols may exert both a positive or a negative radiative forcing, depending on whether they are located on a bright surface (like a snow-covered surface or a bright cloud, thus yielding a positive forcing) or a dark surface (such as oceans or forests, thus yielding a negative forcing).

If an aerosol is located at the top of the atmosphere (TOA), whether it can or cannot absorb, the net effect is always a reduction of SW irradiance at the surface. If it can absorb, the effects of the positive radiative forcing induced by the aerosol will be only observed in the layer where the aerosol lies. As an example, an increase in stratospheric SO_2 due to intense volcanic activity yields a net stratospheric warming, while the underlying layers will experience a net cooling.

The so-called *aerosol's indirect effect* refers to the mechanisms by which aerosols modify the microphysical and hence the radiative properties and the lifetime of clouds. Size, chemical composition, mixing ratio and surrounding environment determine if an aerosol can act as a condensation nucleus for clouds, as well as an ice nucleus.

By affecting the cloud droplet number concentration, the aerosol modifies the cloud albedo. By keeping the cloud liquid water content unaltered, a high aerosol concentration, as it might be found in polluted regions, can determine a high concentration of small cloud droplets, thus increasing the cloud reflectivity, i.e. the albedo.

By affecting the cloud liquid water content and the cloud height, the aerosol modifies the cloud lifetime. High concentration of small droplets leads to decreased drizzle production and reduced precipitation efficiency.

According to the 5th Assessment Report of the Intergovernmental Panel for Climate Change (IPCC), issued in 2013, on a global scale aerosols are estimated to account for the greatest cooling contributions (-0.27 W m^{-2} as a mean net contribution) and the level of confidence relating to the aerosol direct effect is classified as high. On the other hand, the aerosol indirect effect provides a greater cooling contribution (-0.55 W m^{-2}), but its

level of confidence is classified as low. Figure 1.8 reports the net contribution and the level of confidence associated with each forcing.

From a modelling perspective, the largest uncertainties in a model-predicted climate change are due to the aerosol emissions in future scenarios. Just like in the case of greenhouse gases, estimates of future aerosol concentrations can be made based on economical and political considerations. However, due to the limited knowledge of most of the aerosol-related feedback mechanisms, any prediction of future climate change should be taken with caution.

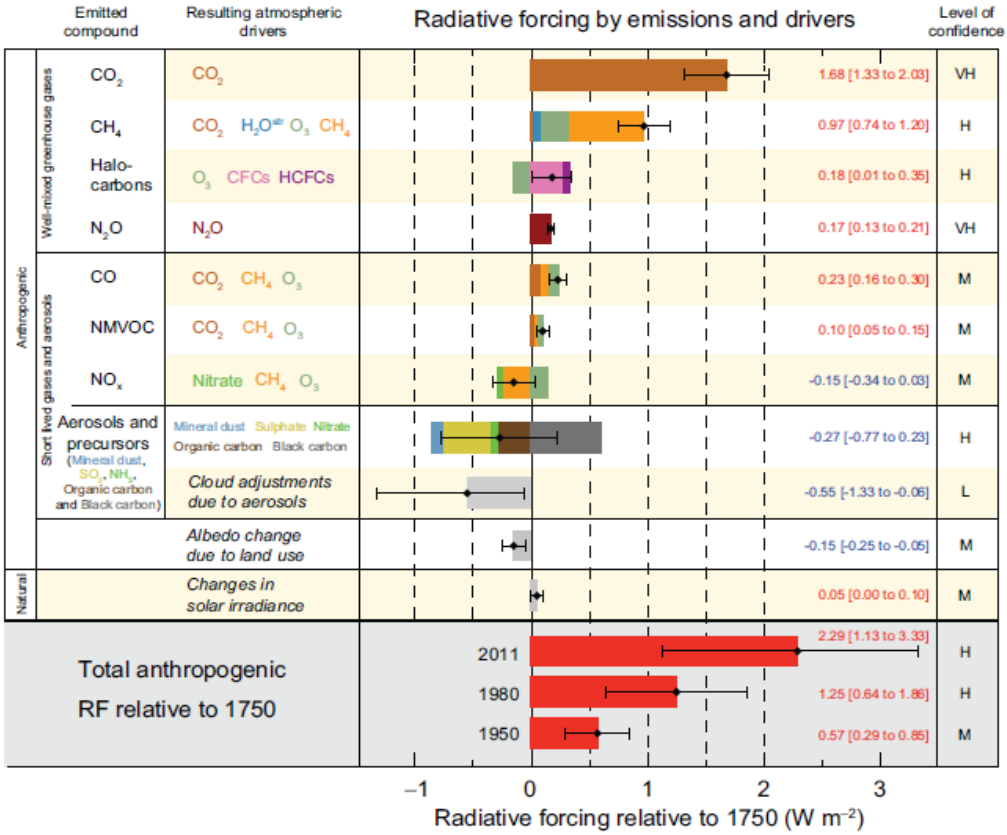

Figure 1.8: Global mean radiative forcings as estimated by the 5th Assessment Report of the Intergovernmental Panel for Climate Change (IPCC) in 2013. Diagrams bending on the right imply a positive forcing (warming), while diagrams bending on the left imply negative forcing (cooling). A level of confidence is associated with each forcing (from IPCC 5th Assessment Report, 2013).

1.4.2 Health effects

Since the Industrial Revolution it was realised that an increase in particulate emission was often associated with a decrease in the quality of life in terms of diseases. Before then, only miners or scavengers could be aware of the negative effects of inhaling large

amounts of dust or smoke. To the present day evidences suggest links between aerosols and cardiovascular, pulmonary and airway diseases (Pope and Dockery, 2006).

Due to the effects aerosols exert on the human health, the European Union and the U.S.A. have issued directives for aerosol standards: the EU Standards for Particulate Matter (PM_{10} and $PM_{2.5}$), reported in Table 1.1, and the National Ambient Air Quality Standards (Putaud, 2003; NAAQS; Air Quality Standards). These directives impose limits to the daily and yearly PM mass concentrations and therefore to the emissions of particulate matter by traffic and industries.

	Concentration [µg/m3]	**Averaging time**	**Entrance into force of the limit value**	**Permetted exceedances per year**
PM_{10}	50	24 hrs	01/01/2005	35
	40	1 year	01/01/2005	n/a
$PM_{2.5}$	25	1 year	01/01/2015	n/a

Table 1.1: EU Standards for Particulate Matter for PM_{10} and $PM_{2.5}$ (from Air Quality Standards).

The term PM_{10} ($PM_{2.5}$) refers to the mass concentration of particles with an aerodynamic size smaller than 10 µm (2.5 µm), whatever the particle origin, source and chemical composition. The classification of particles by their aerodynamic diameter is mostly for conventional and air monitoring purposes as the aerodynamic size determines the transport and removal of particles from air, the particle chemical composition and, most importantly, the particle deposition inside the respiratory system (CAFE, 2005).

In urban environments, particles are usually divided into two groups: coarse particles and fine particles. The border between these groups lies between 1 and 2.5 µm in aerodynamic diameter. For measurement purposes, the term $PM_{2.5}$ indicates the fine fraction, while the term PM_{10} refers to the coarse fraction.

Figure 1.9 reports the three modes by which atmospheric aerosol is usually classified. By looking at the particle volume, which is directly linked to the particle mass, the coarse mode and the accumulation mode are clearly visible. Particles of the coarse mode are generated by breakup of larger solid particles, mostly due to windblown dust from agricultural processes, mining operations and uncovered soil. Other sources of coarse particles are traffic emissions, sea spray, pollens and fungal spores.

Coarse particles (Valavanidis et al., 2008) account for 90-95% of the total mass of

suspended particulate, but when considering the particle number concentration they account for a very small fraction. On the contrary, while fine particles account for a very small fraction of the total PM mass (1-8%), they appear to be the most important contributor for the PM number concentration. Ultrafine particles (less than 0.1 μm in diameter), also known as Aitken mode particles, are mostly generated by gas-to-particle conversion and nucleation. An example of these processes is provided by Diesel engines, which are a major source of ultrafine particles in urban environments (Giechaskiel et al, 2014; Reşitoğlu and Altinişik, 2015).

Once formed, ultrafine particles grow by condensation (gas condensation onto the surface of existing molecules) or coagulation (two or more particles combining to form a bigger one) and generate the so-called accumulation mode (around 0.1 μm in diameter).

Fine particles ($PM_{2.5}$) appear to be strongly associated with mortality and hospitalisations due to cardio-vascular diseases; in particular, ultrafine particles (less than 0.1 μm in diameter) are associated with negative health effects.

Ultrafine particles are however thought to be the most harmful because of their porous surface and their large surface area due to their large number concentration, which allows them to adsorb toxic substances (Valavanidis et al., 2008). In particular, as they deposit by diffusion in all parts of the respiratory tract, through the blood and lymph circulation they can easily reach potentially sensitive target sites such as bone marrow, lymph nodes, spleen, and heart (Obersdörster et al., 2005).

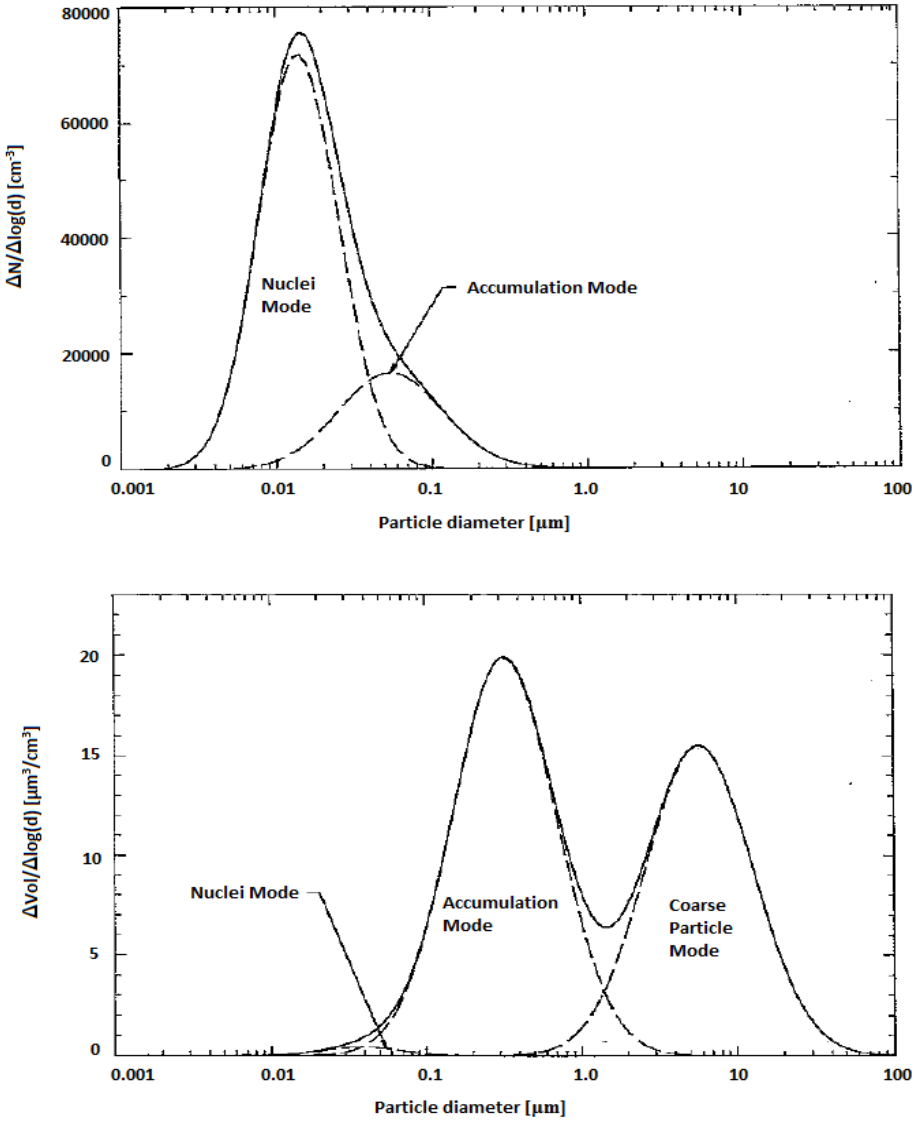

Figure 1.9: Atmospheric aerosol particle modes (adapted from Hinds, 1999).

A schematic of how PM is inhaled and interact with the human body is reported in Figure 1.10. In particular, it is thought that inhaled particles may affect the behaviour and characteristics of blood, lungs, heart, vasculature and brain.

As for the exposure period, short-term exposures to ambient PM in highly polluted areas may lead to general airways disturbances, the greatest effects being more remarkable in elderly subjects and people with pre-existing heart and lung diseases, who are usually more susceptible to the PM effects on mortality and morbidity (Fowler et al., 2012).

On the other hand, long-term exposures to high PM levels may lead to a reduction in life expectancy by a few months up to a few years due to cardio-pulmonary diseases, lung

cancer and generic reduced lung function. The Aphekom project has issued a summary report for the impact of the air pollution on health in Europe for the period 2008-2011. Figure 1.11 shows the average $PM_{2.5}$ level and describes the forecast increase in life expectancy in 25 cities of the survey in case of decrease of $PM_{2.5}$ concentration down to 10 $\mu g\ m^{-3}$, while Figure 1.12 shows the percentage of the population in 10 different cities affected by chronic diseases due to living near busy streets and roads (Aphekom, 2011).

As reported by Pope and Dockery (2006), major effects due to PM exposure are found in socially disadvantaged and poorly educated populations, with no differences between men and women and between smokers and non-smokers. In any case, a strict dependency of the death rates on the exposure's time-scale and the PM level is observed.

Some of the features contributing to toxicity are the metal content, the presence of polycyclic aromatic hydrocarbons and an extremely small size. Sources associated with health effects include combustion engines, coal burning and wood burning. Particles from these sources mostly belong the fine and ultrafine fraction and appear to have a strong inflammatory potential.

Finally, carbonaceous and metal particles often present mutagenic activity (Pastuszka et al., 2000; Valavanidis and Vlachogianni, 2008).

Biogenic particles such as fungi, fungal spores or bacteria are often associated with respiratory disturbances like asthma (Pastuszka et al., 2000), which can be exacerbated by a prolonged exposure.

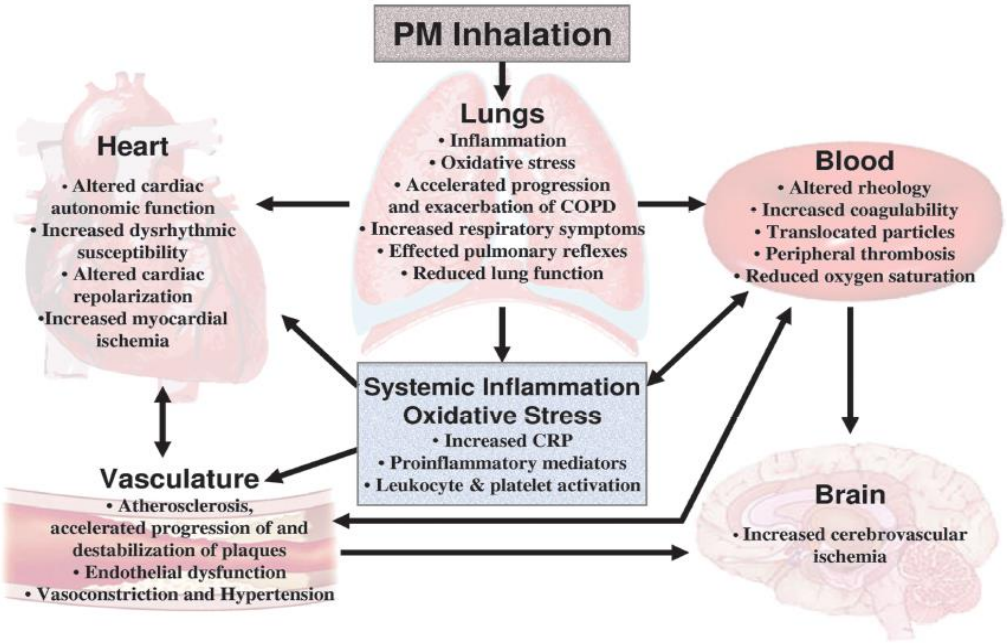

Figure 1.10: Potential general pathophysiological pathways linking PM exposure with cardiopulmonary morbidity and mortality (from Pope and Dockery, 2006).

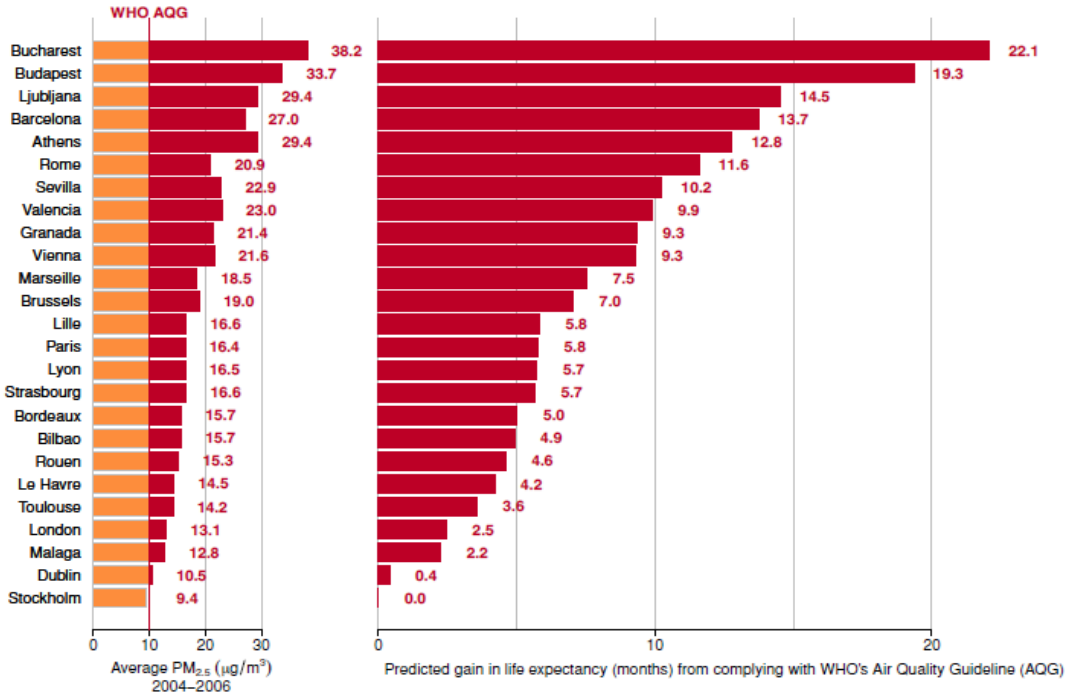

Figure 1.11: Average $PM_{2.5}$ (left) and predicted average gain in life expectancy (months) for persons 30 years of age and older in 25 Aphekom cities for a decrease in the average annual level of $PM_{2.5}$ to 10 µg m^{-3} (right). Picture from Aphekom (2011).

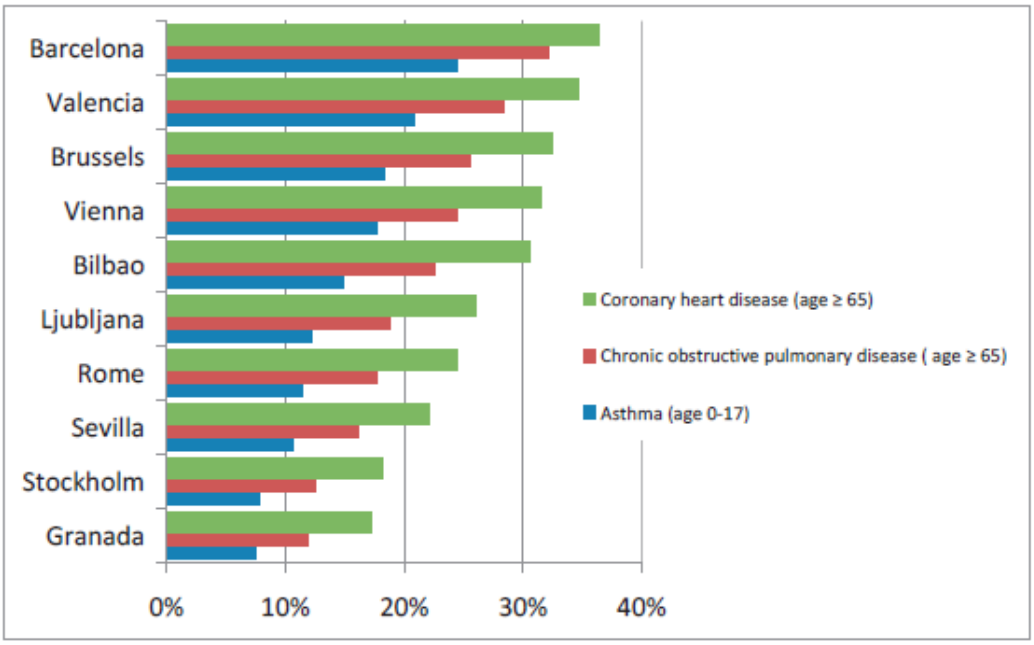

Figure 1.12: Percentage of population with chronic diseases due to living near busy streets and roads in 10 Aphekom cities (from Aphekom, 2011).

Chapter 2: Aerosol physics and applications

2.1 Aerosol mechanics and behaviour

In this chapter the main features of aerosol mechanics and behaviour are reviewed. Starting from kinetic gas theory, Stokes's resistance law will be enounced and concepts like settling velocity, Stokes number and Brownian diffusion will be introduced and described. Formulas are taken from Hinds (1999).

2.1.1 Ideal gas law and Reynolds number

The gas in which particles are suspended resists particle motion depending on the particle size. For a perfect gas, the kinetic theory of gases and therefore the ideal gas law are valid. The gas at issue is the air, which is approximately an ideal gas and to which the ideal gas law can apply.

The kinetic theory of gases assumes that:

1) gases contain a large number of molecules;
2) molecules are small compared with the distance between them;
3) molecules are rigid spheres travelling in straight lines between elastic collisions.

The ideal gas law follows from these assumptions. It states that at constant temperature T and number of molecules n, the product between pressure and the volume occupied by the gas is constant:

$$p\ v = constant$$

Equation 2.1

or

$$p\ v = n\ R\ T$$

Equation 2.2

where n is the molecular concentration and R = 8.314 J mol^{-1} K^{-1}. For the atmosphere, in the case of dry air, the ideal gas law can be re-written as follows:

$$p = \rho_a R_v T$$

Equation2.3

where ρ_a is the air density and R_v = 287 J kg^{-1} K^{-1}.
Due to the interaction of particles with the gas in which they are suspended, a *mean free path* λ is defined as the average distance travelled by a molecule between successive collisions.

$$\lambda = \frac{\bar{c}}{n_z}$$

Equation 2.4

where $\bar{c}$ is the mean molecular velocity and n_z is the number of interactions per unit time. The property that indicates how much the gas resists particle motion is called *viscosity* η. For an ideal gas viscosity is related to the mean free path according to:

$$\eta = \frac{1}{3} n m \bar{c} \lambda$$

Equation 2.5

where m is the mass of one gas molecule. In terms of molecular energy, viscosity is related to the absolute temperature T by:

$$\eta = \frac{2 (m k T)^{\frac{1}{2}}}{3 \pi^{3/2} d_m^2}$$

Equation 2.6

where k = 1.38 10^{-23} J K^{-1} is the Boltzmann constant and d_m is the collision diameter of the molecule, i.e., the distance between the centres of two molecules at the instant of collision; for air d_m is approximately 3.7 10^{-10} m.

Viscosity only depends on gas molecular constants; however Equation 2.6 is only exact for perfect sphere. For most of the temperature ranges of interest, the correct dependency between η and T is $T^{0.74}$.

When dealing with fluids, the quantity that provides insight on the flow regime (laminar or turbolent) is the *Reynolds number*, which is given by:

$$Re_g = \frac{\rho V d}{\eta}$$

Equation 2.7

where V is the relative speed between the fluid and a particle, ρ is the density of the fluid and d is a characteristic linear dimension, such as the diameter of a pipe the flow must pass through.

Re_g is the ratio of the fluid inertia to the fluid viscosity. Low Re_g (less than or approximately 1) indicates laminar flow, while high Re_g indicates turbolent flow.

2.1.2 Stokes's resistance law, Stokes number and settling velocity

When a particle travels in a gas, it will face a resistance force. The force the gas will exert on the particle is given by Newton's resistance law, whose general form is:

$$F_D = C_D \frac{\pi}{8} \rho_g d^2 V^2$$

Equation 2.8

where C_D is the drag coefficient and ρ_g is the density of the gas resisting particle motion. The Reynolds number of a particle Re_p is given by:

$$Re_p = \frac{\rho \left(V_p - V_g\right) d_p}{\eta}$$

Equation 2.9

where $V_p - V_g$ is the velocity difference between the particle and the gas and d_p is the particle size. For $Re_p > 1000$ Stokes's law is valid.

$$F_D = 3\,\pi\,\eta\,(V_p - V_g)\,d$$

Equation 2.10

For $Re_p < 1$, by equating Stokes's law to Newton's law, it may be seen that a relationship exists between C_D and Re_p.

$$C_D = \frac{24\,\eta}{\rho_g (V_p - V_g)\,d} = \frac{24}{Re_p}$$

Equation 2.11

Fig 2.1 shows the particle Reynolds number as a function of the drag coefficient. It is observed that at small Re_p (less than 1), C_D and Re are inversely proportional, while at high Re_p (greater than 1000), C_D assumes a nearly constant value of 0.44. Stokes's law is valid for perfect spheres and for incompressible fluids

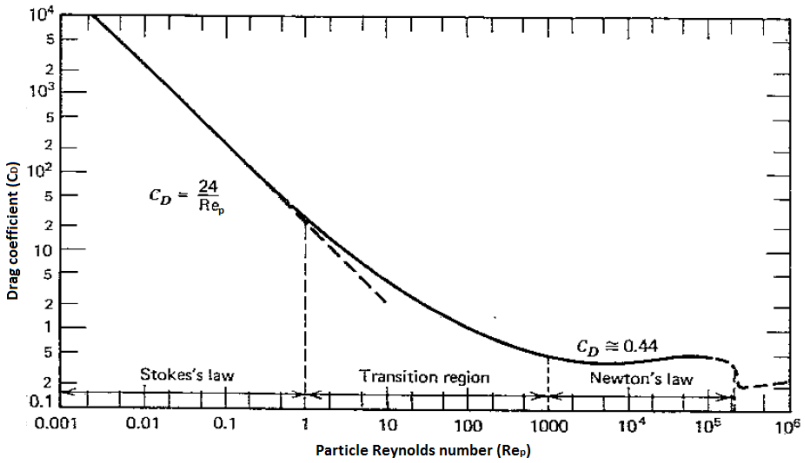

Figure 2.1: Variation of C_D with Re_p. For $Re_p < 1$ C_D is inversely proportional to Re_p (Stokes's region), while for $Re_p = 10^3$-10^5 C_D is nearly constant and equal to 0.44. In the middle lies the transition region (adapted from Hinds, 1999).

When a particle travels inside a gas that resists its motion, if the particle is subjected to an acceleration, at a certain point the resistance offered by the gas will equal the acceleration of the particle. At this point, the velocity of the particle will be constant
If the acceleration is provided by the gravitational force, Stokes's law predicts:

$$F_D = F_G = m\,g$$

Equation 2.12

$$3\,\pi\,\eta\,(V_p - V_g)\,d = \frac{(\rho_p - \rho_g)\pi\,d^3 g}{6}$$

Equation 2.13

By neglecting ρ_g as it is usually much smaller than the particle density ρ_p , one finds the *settling velocity* V_{TS}.

$$V_{TS} = \frac{\rho_p d^2 g}{18\,\eta}$$

Equation 2.14

V_{TS} rapidly increases with particle size and decreases with increasing viscosity.
Two important corrections to Stokes's law must be applied. As for the first one, it should be observed that Stokes's law assumes that the relative velocity of the gas at the surface of the particle is zero. This assumption is no longer valid when the particle size approaches the mean free path of the gas (i.e., when $d << \lambda$). These particles travel faster as they slip on the surface of the gas. The *Cunningham slip correction factor* C_c must therefore be added.

$$F_D = \frac{3\,\pi\,\eta\,V\,d}{C_c}$$

Equation 2.15

For oil droplets and solid particles C_c is given by:

$$C_c = 1 + \frac{\lambda}{d}\,[2.34 + 1.05\exp\left(-0.39\,\frac{d}{\lambda}\right)]$$

Equation 2.16

A second correction must be applied when considering that Stokes's law is only valid for perfect spheres. A *dynamic shape factor* χ is defined as the actual resistance force of the non-spherical particle to the resistance force of a sphere having the same volume and velocity as the non-spherical particle:

$$\chi = \frac{F_D}{3\,\pi\,\eta\,V\,d_e}$$

Equation 2.17

Therefore Stokes's law for irregular particles becomes:

$$F_D = \frac{3\,\pi\,\eta\,(V_p - V_g)\,d_e\,\chi}{C_c}$$

Equation 2.18

and the settling velocity is given by:

$$V_{TS} = \frac{\rho_p d^2 g\,C_c}{18\,\eta\,\chi}$$

Equation 2.19

Another equivalent diameter is the *aerodynamic diameter* d_a, which is defined as the diameter of the spherical particle with a density $\rho_0 = 1000$ kg m^{-3} that has the same settling velocity as the particle under observation. Related to Stokes's law is the *relaxation time* τ, i.e. the time required for a particle to adjust to a new condition of forces:

$$\tau = m\,B = \rho_p \frac{\pi}{6} d^3 \left(\frac{C_c}{3\,\pi\,\eta\,V\,d}\right) = \frac{\rho_p d^2 C_c}{18\,\eta} = \frac{\rho_0 d_a^2 C_c}{18\,\eta}$$

Equation 2.20

where B is the mechanical mobility, which is defined as the ratio of V_{TS} to the drag force F_D. In other words, the relaxation time states how long it will take to a particle to reach steady state conditions.

The relaxation time is present in the definition of the *Stokes number* Stk, which is a measure of the particle inertia. If airstream lines encounter an obstacle on its path, they will bend aside in order to avoid it. Particles with small inertia, i.e. small relaxation time, will follow the streamlines and avoid the obstacle; particles with greater inertia, i.e.

greater relaxation time, will be unable to avoid the obstacle and collide with it.

Given S, the stopping distance of the particle (the distance at which a particle will be steady), U_0, the air velocity far from the obstacle and d_c, the characteristic size of the obstacle, Stk is given by:

$$Stk = \frac{S}{d_c} = \frac{\tau\, U_0}{d_c}$$

Equation 2.21

Stk provides an important tool to capture big particles (i.e., particles with great inertia) from a flow. This is the working principle of an impactor, which is schematically represented in Figure 2.2. If the flow bends due to the presence of an obstacle (impaction plate), particles with small inertial will be able to follow the flow, while particles with great inertia will finally be captured by the impaction plate. Therefore, there will exist a particular trajectory establishing the inertia a particle should have in order to avoid being captured by the impaction plate (limiting trajectory).

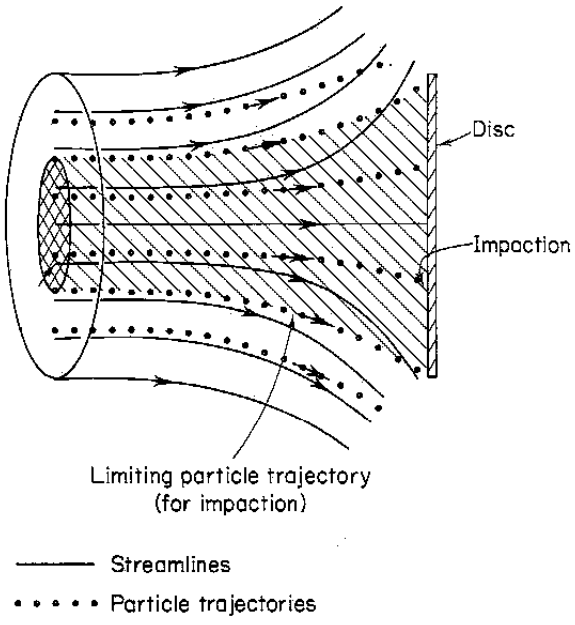

Figure 2.2: Schematic of an impactor. Adapted from Vincent (1989).

2.1.3 Brownian diffusion

In presence of a concentration gradient particles will tend to move apart in the opposite direction of the concentration gradient. This process is called Brownian motion and the net transport of particles subjected to Brownian motion is called *diffusion*. It is governed by Fick's law, which relates the particle flux to the particle concentration gradient dn/dx.

$$J = -D \frac{dn}{dx}$$

Equation 2.22

From this equation, it can be inferred that the larger the diffusion coefficient D, the stronger the Brownian motion and the more rapid the mass transfer will be. It can be shown that D is given by (Hinds, 1999):

$$D = \frac{k\ T\ C_c}{3\ \pi\ \eta\ d} = k\ T\ B$$

Equation 2.23

The smaller the particle, the more efficient the transport by diffusion will be.

The motion of a particle subjected to Brownian diffusion depends on the interactions with the gas molecules and is therefore related to the mean free path. If at one moment the particle is travelling in one direction, the moment later is travelling in another direction. The net displacement over a long time depends on statistical combinations of many of these small-scale motions.

It can be shown that the root mean square displacement of the particle x_{rms} along any axis is given by:

$$x_{rms} = \sqrt{2\ D\ t}$$

Equation 2.24

Hence it turns out that the fraction of the total number of particles originally released that lie between x and x + dx at time t is given by:

$$\frac{dn(x,t)}{n_0} = \frac{1}{(4\,\pi\,D\,t)^{\frac{1}{2}}} \exp\left(-\frac{x^2}{4\,D\,t}\right) dx$$

Equation 2.25

where n_0 is the number of particles released at t = 0.

Particles adhere when they collide with a surface. Therefore the aerosol concentration at the surface is zero and a gradient is created in the region close to the surface. The concentration gradient yields a continuous diffusion of aerosol particles to the surfaces, which leads to a gradual decrease in concentration. As time passes, the concentration gradient becomes less steep, but extends farther and farther away from the surface. Figure 2.3 schematises the process.

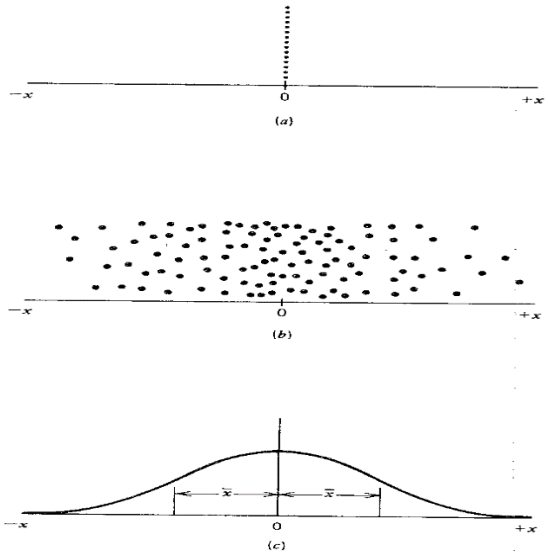

Figure 2.3: Particle dispersion due to Brownian motion. (a): initial condition (t=0); (b): particle distribution at times t > 0; (c): frequency distribution at time t > 0. Picture from Hinds (1999).

2.2 Aerosol optics

Due to their size, aerosols interact with the electromagnetic radiation emitted by the Sun and the Earth. As aerosols are able to scatter and partially absorb the incoming radiation, they play an important role in the optical branch of atmospheric physics in terms of radiation budget (as mentioned in Chapter 1.4.1) and visibility. Low visibility is mostly due to high scattering rates owing to great aerosol concentrations. An example of the aerosol effect on visibility is provided by Figure 2.4.

Figure 2.4: Difference in visibility due to different aerosol concentrations in Beijing.

2.2.1 Aerosol scattering

The term scattering refers to the process where light photons are forced to deviate and change their initial trajectory as they encounter an obstacle (i.e., a particle) along their path. When a particle passes through a light beam, the resulting scattering process is a function of the light wavelength, the particle size, the particle refractive index and the relative angle between the particle and the beam. As previously remarked, if the particle size is considerably small compared with the light wavelength Rayleigh scattering occurs. If the particle size is considerably greater than the light wavelength, the process can be easily described by geometric optics. In the intermediate situation Mie scattering occurs. Figure 2.5 includes a schematic of the scattering process.

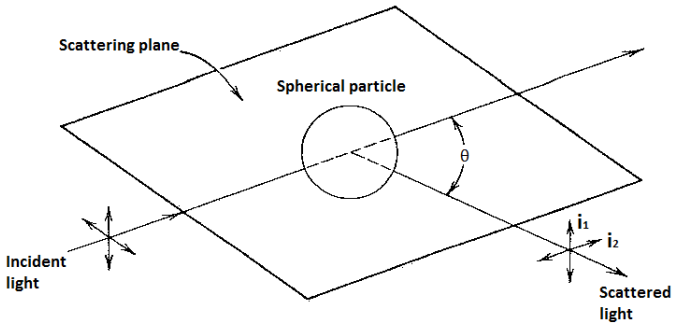

Figure 2.5: Schematic of scattered light including scattering angle, scattering plane and polarised components (i_1 and i_2). Adapted from Hinds (1999).

Considering the incoming solar radiation in terms of the *wavelength* λ, the scattering of light by particles smaller than 0.05 μm (i.e., $d << \lambda$) is well described by Rayleigh's theory (molecular scattering), while scattering by particles greater than about 100 μm (i.e., $d >> \lambda$) can be described by geometric optics. Between these sizes, the most important range

of interest in terms of aerosol studies is the Mie scattering region, where d and λ are of the same magnitude order. Although the extreme importance of Mie scattering when dealing with aerosol, care must be taken as Mie's theory, which leads to a particular solution of Maxwell's equation, is only exact for spheres.

The speed of light in the vacuum c is a constant and is about $3\ 10^8$ m s^{-1}. The wavelength λ and c are linked together by the following relation:

$$c = \lambda \nu$$

Equation 2.26

where ν is called the radiation *frequency*.

The ratio between the speed of light in the vacuum c to the speed of light in a given material V is the *absolute index of refraction* m, which is always greater than 1.

$$m = \frac{c}{V}$$

Equation 2.27

The index of refraction for absorbing materials is expressed as complex number:

$$m = m_R + iam_I$$

Equation 2.28

where m_R and m_I are respectively the real and the imaginary part of the refractive index. Non-absorbing particles always have the imaginary part of the refractive index equal to zero. It should be noted that both the real and the imaginary part of the refractive index are strong functions of the wavelength λ.

For particles with a two-phase system, a *relative refractive index* m_r is used, which is defined as the ratio of the velocity of light in the suspending medium V_m to the velocity of light in the particle V_p.

The refractive index of air is almost identical to that of a vacuum, therefore the absolute and relative refractive indices are equal for aerosol particles. Differences arise when dealing with particles suspended in liquids.

As mentioned before, the scattering of light depends on the particle size. A *size parameter*

α is therefore defined as follows:

$$\alpha = \frac{\pi\, d}{\lambda}$$

Equation 2.29

If α is much smaller than 1, Rayleigh scattering occurs, while geometric optics is the case of α >> 1. Mie scattering lies in the intermediate region.
The light intensity resulting from Rayleigh scattering is given by (Hinds, 1999):

$$I(\theta) = \frac{I_0\, \pi^4 d^6}{8\, R^2\, \lambda^4} \left(\frac{m^2-1}{m^2+2}\right)(1 + \cos^2\theta)$$

Equation 2.30

This equation indicates that the resulting intensity is inversely proportional to the square distance from the radiation source, is a very strong function of the particle diameter (d^6) and an inverse strong function of the wavelength (λ^{-4}).
This equation holds for all particles with size smaller than 0.05 μm.
For greater particles Mie's theory must be used. As previously mentioned, this theory is only exact for perfect spheres. The scattered intensity from unpolarised light is given by:

$$I(\theta) = \frac{I_0 \lambda^2\, (i_1 + i_2)}{8\, \pi^2 R^2}$$

Equation 2.31

The Mie intensity parameters (or polarised components) i_1 and i_2 for scattered light with perpendicular and parallel polarisation respectively are complicated functions of m, α and θ (see Figure 2.6 and Figure 2.7 for details). Due to the difficulties relating to the calculations of these functions, scattered light intensities are usually estimated from i_1 and i_2 and tabulated as functions of m, α and θ or calculate the functions using a computer.
Due to the sizes of aerosol particles and the typical wavelengths (usually visible light) of the laser beam of an optical instrument measuring aerosol parameters, Mie scattering is the most exploited process to count and classify particles. However, at large particle sizes,

the Mie scattering intensity is no longer a monotonic function of the particle diameter, but rather it presents oscillations that become more numerous at higher scattering angles. This is a serious drawback as a given scattering intensity may correspond to more than one particle sizes.

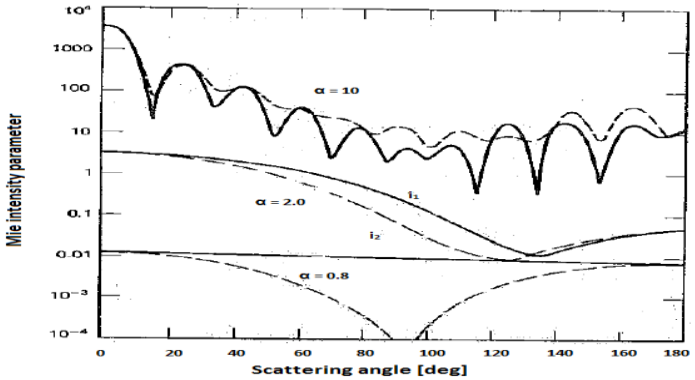

Figure 2.6: Mie intensity parameters versus scattering angle for water droplets (m=1.33) having α=0.8, 2.0 and 10.0. Solid lines are i_1 and dashed lines are i_2 (adapted from Hinds, 1999).

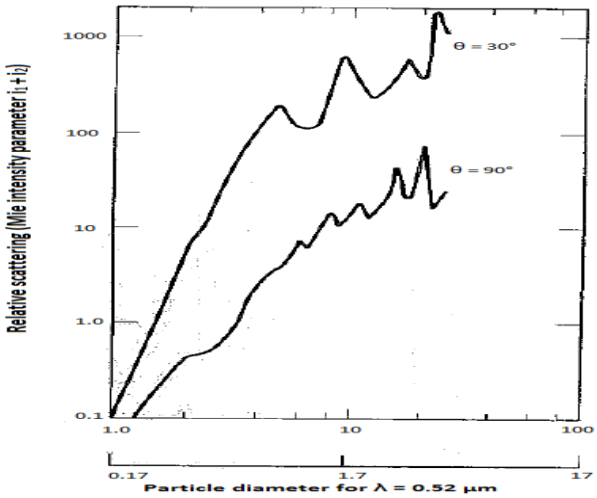

Figure 2.7: Relative scattering (Mie intensity parameter: i_1+i_2) versus size parameter for water droplets (m=1.33) at scattering angles of 30° and 90° (adapted from Hinds, 1999).

2.2.2 Extinction and Beer law

Aerosol particles illuminated by a light beam scatter and absorb the incoming light. This process is called *extinction*. Absorption will only concern particles made of absorbing material, while scattering will concern all particles.

Extinction is responsible for alteration of visibility and sun illumination during daytime in the earth's atmosphere. As an example, black smoke appears black because it absorbs visible light. Pollution particles cause visibility degradation as they scatter back most of the incoming visible light.

The reduction in radiation *intensity* I due to extinction is given by the Beer-Bouguet-Lambert law:

$$\frac{I}{I_0} = \exp(-L\,\sigma_e)$$

Equation 2.32

where L is the path length of the light beam inside the medium (i.e., the aerosol) and σ_e is the extinction coefficient.

For monodisperse particles the following relations are valid:

$$\sigma_s = \sigma_a + \sigma_e$$

Equation 2.33

$$Q_s + Q_a = Q_e$$

Equation 2.34

$$\sigma_e = N\,A_p Q_e = \frac{\pi\,N\,d^2 Q_e}{4}$$

Equation 2.35

where σ_a and σ_s are respectively the absorption and scattering part of extinction coefficient, N is the number of particles per unit volume, while Q_e is the particle extinction efficiency (Q_a is the absorbing part and Q_s is the scattering part), which is defined as the ratio of the radiant power scattered and absorbed by a particle to the radiant power geometrically incident on the particle. The variation of Q_e with respect to the size parameter α at different refractive indices is shown in Figure 2.8. For non-absorbing particles σ_e is exactly equal to σ_s. For polydisperse particles the total σ_e is given by the sum of each of the σ_es for all particle sizes:

$$\sigma_e = \frac{\sum_i \pi\,N_i d_i^2 Q_{e\,i}}{4}$$

Equation 2.36

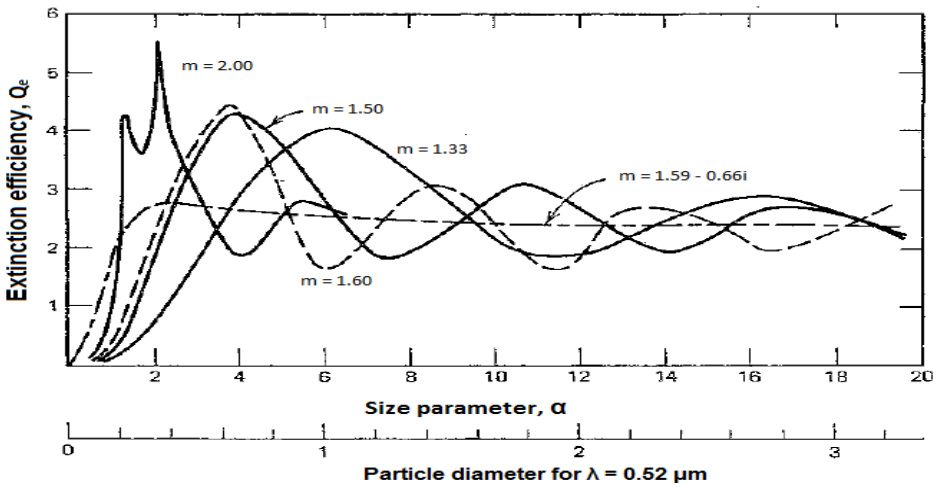

Figure 2.8: Extinction efficiency versus particle size (adapted from Hinds, 1999).

2.3 Aerosol filtration and deposition

The way aerosols interact with other bodies while suspended in the air has led to the development of several instruments and techniques to capture particles for different purposes, including: study of the particle general behaviour, sampling of the particle mass concentration for air monitoring, as well as particle filtration for health purposes.

In the next paragraphs some of the main techniques, effects and equipment relating to aerosol mechanics are reviewed.

2.3.1 Filtration

Filtration is widely deployed in aerosol sampling and air cleaning as it is a simple, versatile and mostly economic tool. In aerosol sampling there exist two important types of filters: fibrous filters and porous membrane filters.

Fibrous filters mostly consist of air (porosity: 70-99%). Fibres range in size from submicrometer up to 100 μm. The most common types are cellulose fibres, glass fibres and plastic fibres. The air velocity through high-efficiency filters is of the order of 0.1 m s^{-1}.

Porous membrane filters have lower porosities than fibrous filters (50-90%). The gas flows through the filter follows an irregular path in the complex pore structure and particles deposit on the elements that form the pores. A widely used membrane filter is

the capillary pore membrane filter (Nuclepore), which has an array of microscopical cylindrical holes of uniform diameter, approximately perpendicular to the filter's surface. For air-cleaning purposes, a filter is usually characterised in terms of its *penetration* P, which is the (mass or number) fraction of entering particles that exit the filter. The velocity of the air at the face of the filter just before it enters is called the *face velocity* U_0 and is defined as (Hinds, 1999):

$$U_0 = \frac{Q}{A}$$

Equation 2.37

where Q is the volumetric flow rate through the filter and A is the cross-sectional area of the filter exposed to the air stream. Inside the filter, the air velocity is increased by the presence of the filter fibres (or membrane or granules), so that the actual velocity U is given by:

$$U = \frac{U_0}{1 - \alpha}$$

Equation 2.38

where α is the filter's volume *packing density* or *solidity* and is linked to the filter's porosity by the following equation:

$$\alpha = \frac{fiber\ volume}{total\ volume} = 1 - porosity$$

Equation 2.39

A fibrous filter may be thought of as many layers, each one having a certain probability of collecting particles of a given size. By considering the fractional capture per unit thickness γ for a differential layer dt, it can be shown that the filter's penetration for monodisperse aerosols is given by:

$$P = e^{-\gamma t}$$

Equation 2.40

The value of γ depends on particle size, face velocity, porosity and fiber size, therefore this equation does not hold for the overall penetration of a polydisperse aerosol. This makes the process of fibrous filtration highly complex. However, an analysis can be carried out by considering the interaction of a single particle with a single fiber and extending the reasoning for the entire filter.

When a filter's fibre is positioned along the path of an aerosol flow, there are basic mechanisms by which particles are captured:

1) Interception
2) Inertial impaction
3) Diffusion
4) Gravitational settling
5) Electrostatic attraction

The difference between interception (Figure 2.9) and impaction (Figure 2.10) is subtle: in the latter a particle is captured by the filter as it encounters an obstacle and cannot avoid it due to its high inertia; in the former, a particle follows the gas streamline but due its size it comes within one radius of the surface of a fibre and is captured.

Brownian diffusion (Figure 2.11) enhances the probability for small particles to hit a fibre while travelling on a non-intercepting streamline. Gravitational settling is only important is particles are big and the flow speed is low. Electrostatic deposition is extremely important, yet it is usually difficult to quantify as the charge distribution of particles and fibres must be known a-priori.

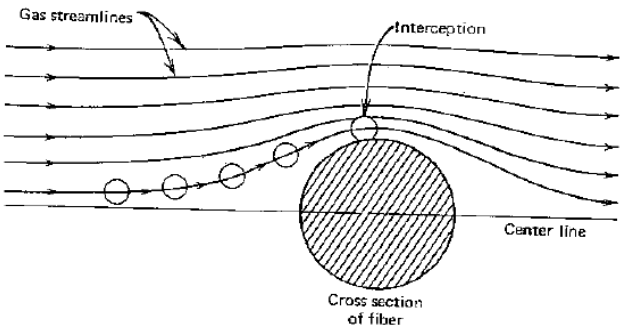

Figure 2.9: Capture by interception (from Hinds, 1999).

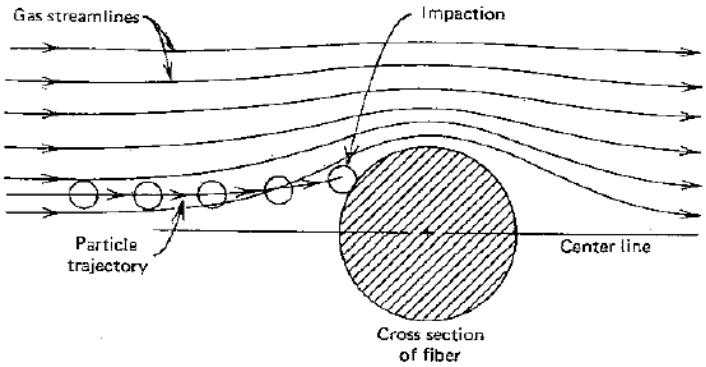

Figure 2.10: Capture by impaction (from Hinds, 1999).

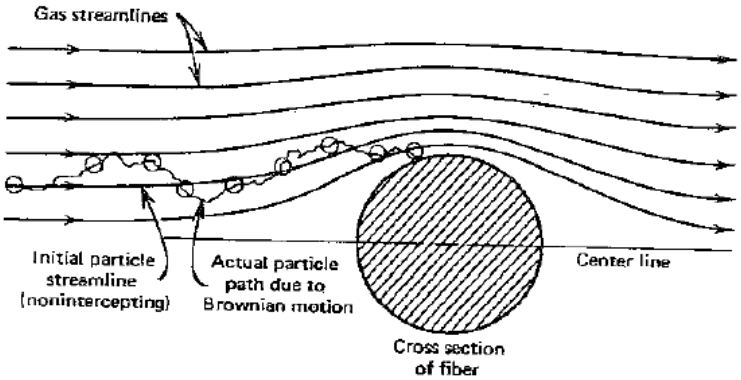

Figure 2.11: Capture by diffusion (from Hinds, 1999).

The single-fibre's efficiency is given by the sum of each single collection mechanism at different particle sizes. As shown by Figure 2.12, at low particle diameters (less than 0.1 μm) diffusion dominates. With increasing particle sizes, impaction and interception gain importance, while diffusion becomes weaker.

It can be therefore noticed that a particle size exists for which the single-fibre filter's efficiency is minimum. This also depends on the filter's face velocity as can be observed in Figure 2.13, but it always lies in the range 0.1-0.5 μm.

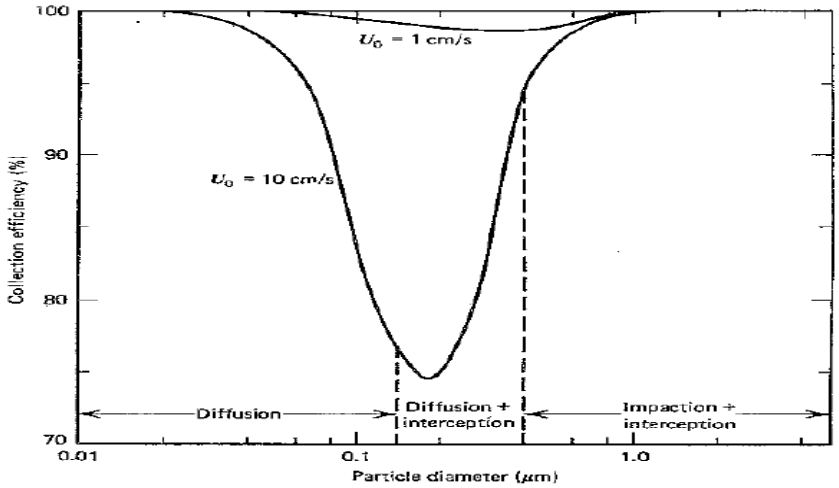

Figure 2.12: Filter efficiency versus particle size for different face velocities, t = 1 mm, α = 0.05 and d = 2 μm (from Hinds, 1999).

2.3.2 Pulmonary deposition

The respiratory system can be divided into three regions: the *head airways*, or *extrathoracic* or nasopharyngeal region, the *lung airways* or *tracheobronchial* region and the *pulmonary* or *alveolar* region (Hinds, 1999).

Inhaled particles may deposit in various region of the respiratory system. The most important deposition mechanisms acting here are impaction, settling and diffusion.

During inhalation, the incoming air will have many direction changes as it flows from the nose or the mouth down to the alveolar region. The net result is that some particles near the airway surfaces deposit by inertial impaction. The harmfulness of a particle depends therefore on its size, chemical composition and on the site at which it deposits within the respiratory system.

In the smaller airways and in the alveolar region the main deposition mechanisms are settling, as the flow velocity is low and the airway dimension is small, and Brownian motion. When considering the region of deposition, it can be inferred that:

a) in the head airways region the main deposition mechanisms are settling and impaction:

this is the way the largest particles are removed on nasal hairs and at bends in the airflow path.

b) In the thoracic airways impaction is the main deposition mechanism for big particles at high flow rates, while for smaller particles and lower flow rates settling becomes more important. Ultrafine particles (less than 0.01 μm) undergo Brownian deposition.

c) Particles not deposited in the head airways and the lung airways regions contribute to the alveolar deposition. Particles larger than 10 μm do not reach this region. In terms of aerosol mass fraction, the great contribution to alveolar deposition is given by particles with size around 2-3 μm

Due to the importance of particle deposition along the respiratory apparatus, several mathematical models have been developed to predict the total and regional deposition. An example is represented in Figure 2.13. These models are based on the combinations of theory with experimental data and apply to typical adults and children. However, as there is a large inter-subject variability for respiratory deposition, individuals may have different deposition patterns.
Particles depositing along the respiratory tract of the human body are usually classified with the following categories:

- *inhalable fraction*, i.e. the aerosols that are actually sampled by the human head;

- *thoracic fraction*, i.e. the part of the inhalable fraction that penetrates and is deposited on the lung airways region;

- *respirable fraction*, i.e. the fraction that further penetrates and is deposited in the alveolar region.

For each of these categories there exist one or more mathematical definitions, according to the criterion used for the sampling.
The sampling criteria for inhalable, thoracic and respirable fractions predicted by the

American conference of governmental industrial hygienists (ACGIH) are exposed in Figure 2.14. Figure 2.15 shows how particle deposition is distributed along the respiratory tract. By looking at the total deposition, it can be observed that, just as in the case of filtration, particles of about 0.5 µm in aerodynamic diameter are not efficiently deposited along the respiratory apparatus because none of the capture mechanisms is particularly strong.

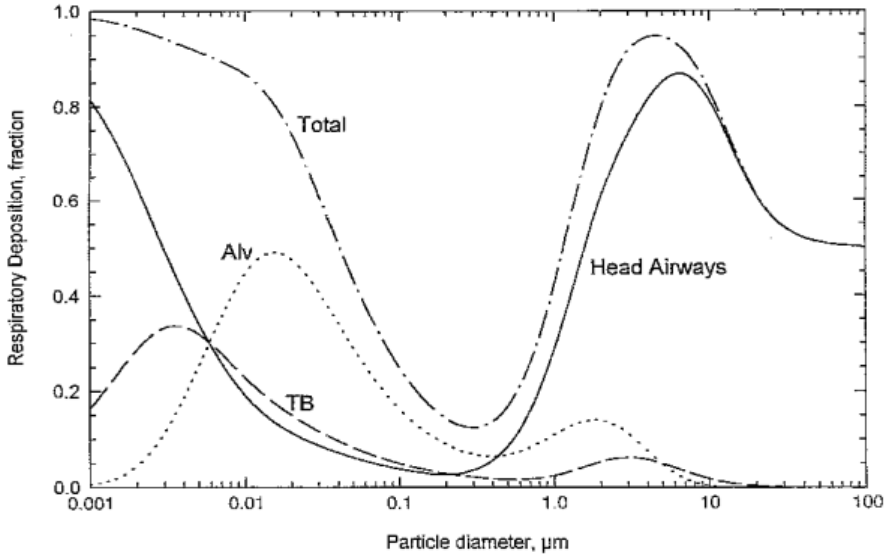

Figure 2.13: Predicted alveolar (Alv), tracheo-bronchial (TB), head airways and total deposition for light exercise (nose breathing) based on a deposition model. Average data for males and females (from Hinds, 1999).

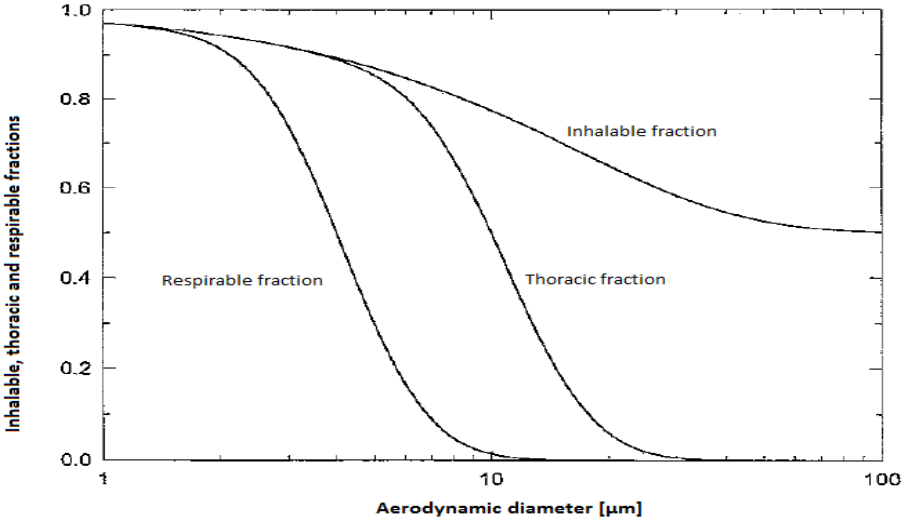

Figure 2.14: American conference of governmental industrial hygienists (ACGIH) sampling criteria for inhalable, thoracic and respirable fractions (adapted from Hinds, 1999).

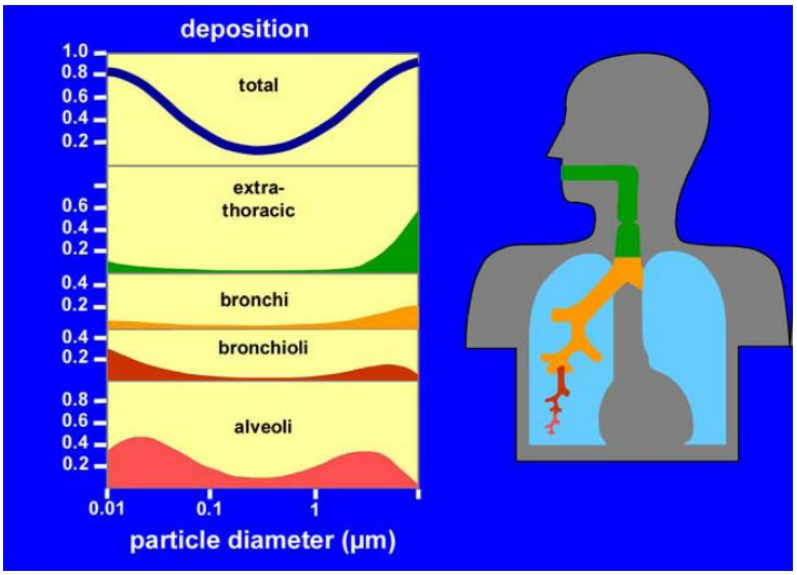

Figure 2.15: Particle deposition along the respiratory apparatus.

As shown by Figure 2.16, for an adult, the aerodynamic diameter value (d_a) of the highest deposition probability for the inhalable, thoracic and respirable fraction is respectively 100 µm, 10 µm and 4 µm. As a result, PM_{10} and PM_4 are nowadays referred to as corresponding to the thoracic and respirable fraction for work places respectively. In order to protect people who are more exposed from atmospheric particles, another curve with a 50% efficiency at d_a = 2.5 µm has been defined and currently used ($PM_{2.5}$)

2.4 Measurement devices for aerosol size: impactors, electrostatic precipitators, mobility analysers

2.4.1 Impactors

An aerosol flow will contain particles with different inertia. If an obstacle is positioned along the path of the flow, particles with small inertia will be able to bend and avoid it, while the ones with great inertia will not follow the streamlines and collide on the obstacle.

This is the working principle of an *inertial impactor*. The aerosol flow is passed through a nozzle and directed towards an obstacle (impaction plate). The parameter governing the collection efficiency is the Stokes's number (Stk). Ideally an impactor should capture all

particles with Stk greater than a certain value. In practice, the relationship between Stk and collection efficiency is not simple and is better explained by cut-off curves (e.g., Figure 2.16), which represent the plot of the impactor's collection efficiency versus the Stokes's number (or its square root) of the incoming particles. In these curves a cut-off point Stk_{50} is usually defined for which the impactor has a collection efficiency of 50%.

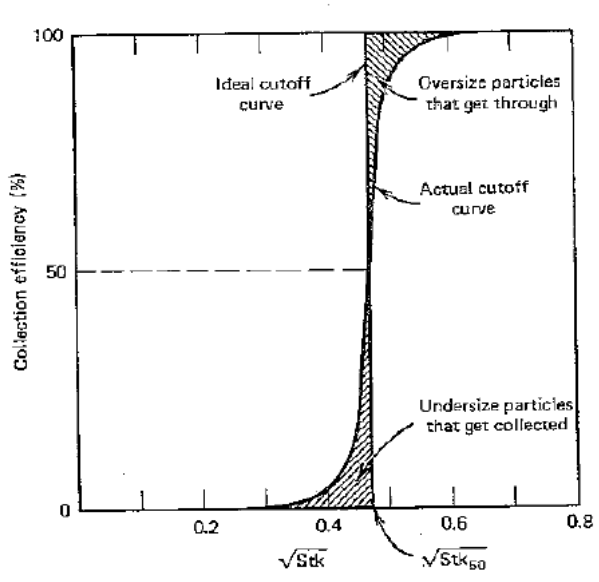

Figure 2.16: Example of an impactor cut-off curve: it represents the plot of the impactor's collection efficiency versus Stk or (like in this case) its square root. As shown in the image, an ideal cutoff curve would have a zero collection efficiency for Stk < Stk_{50} and a 100% collection efficiency for Stk > Stk_{50} (from Hinds, 1999).

If the initial particle concentration is known, by examining the amount of particles deposited onto the impaction plate one can determine the amount of particles exceeding a certain value for Stk. If one wishes to know the aerosol size distribution, several impaction plates can be placed along the aerosol path, each one with decreasing cut-off size, with the largest cut-off sizes coming first. This is a *cascade impactor* (Figure 2.17) and each separate impactor is called an *impactor stage*.

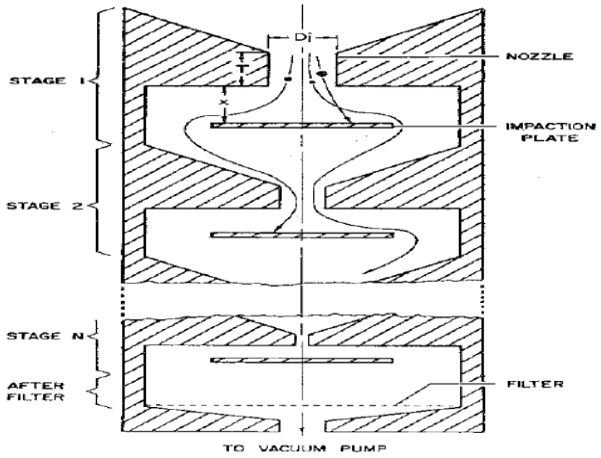

Figure 2.17: Schematic of a cascade impactor (from Hinds, 1999).

Impactors show some problems, e.g. particles may not be collected by the impactor stage, as they are bounced back to the initial flow. This defect can be reduced by coating the impact surface.

A virtual impactor (VI) is a device used to sample, size-separate and concentrate particles with a lower diameter limit denominated as its cut-off. Unlike conventional inertial impactor, a VI does not have solid collection surfaces, but instead, particles are inertially sampled from a large flow to a smaller sub-flow. In a VI, the primary sampled flow is brought through the inlet and is split into major and minor flows (Figure 2.18). Particles with large inertia (i.e. greater than the cut-off size) follow the minor stream, while smaller particles are collected in the major flow. In this way, VIs allow for separating particles smaller than the cut-off size from particles greater than the cut-off size (*dichotomous sampler*).

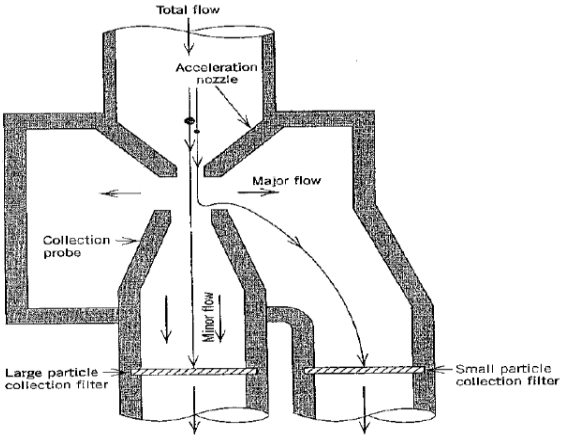

Figure 2.18: Schematic of a virtual impactor (from Hinds, 1999).

Impactors are widely used in PM monitoring systems. They are usually placed before a filter in order to remove particles greater than the PM_x fraction at issue. An example of a PM monitoring station is provided by Figure 2.19: the impactor is the device at the top left, while the pump draws air onto the filter from below.

Figure 2.19: PM sampling station.

2.4.2 Electrostatic precipitators

An electrostatic precipitator is a device that exploits electrostatic forces to collect charged particles for aerosol sampling and air cleaning. The working principle of this device lies in charging particles and subjecting them to an electric field so that the electrostatic migration velocity causes them to deposit on a collection surface.

Particles are usually charged using a corona discharge. The charged aerosol flows then through an electric field oriented perpendicular to the direction of the flow and the collection surface. For a laminar flow precipitator, all particles having velocity $V_{TE} > H*V_x/L$ are collected with 100% efficiency, where H is the distance between the corona discharge wires (or plates), V_x is the flow velocity and L is the dimension along the flow direction. In case of turbolent flow, like in air-cleaning precipitators, efficiency will never be 100%, but it asymptotically approaches this value with increasing V_{TE}.

2.4.3 Mobility analysers

The working principle of a *mobility analyser* relies on introducing aerosol particles along the centreline between two oppositely charged plates. For a given voltage, particles with a mobility greater than a certain amount will migrate towards the plates, while the ones with lower mobility will get through and be collected by a filter positioned downstream. By comparing the mass (or other quantities) sampled when there is no voltage on the plates with the one for different voltages, the distribution of charges and mobilities of the particles can be determined.

A *Differential Mobility Analyser* (DMA), schematised by Figure 2.20, can size particles from 0.005 up to 1 μm at concentrations from 10^{-3} to 10^{5} # L^{-1}. In such a device, an impactor removes particles greater than 10 μm from the input aerosol to avoid problems with the inversion. The aerosol is then neutralised to the Boltzmann equilibrium charge distribution, which represents the charge distribution of an aerosol in charge equilibrium with bipolar ions.

In the electrostatic classifier section, a laminar flow of clean air is surrounded by a thin anular layer of aerosol and the two flows travel axially between a central rod and a coaxial tube. The tube is grounded, while the voltage of the central rod is controlled between 20 and 10000 V. At the bottom of the flow lies a gap, which can only be accessed by particles with a narrow range of mobilities. Particles with greater mobilities migrate to the central rod before reaching the gap, while the ones with lower mobilities pass through the gap and are filtered out.

The serial combination of a Condensation Particle Counter (CPC) and a DMA is called a *Scanning Mobility Particle Sizer* (SMPS), of which Figure 2.21 shows an example, or a *Differential Mobility Particle Sizer* (DMPS). The CPC monitors the exit aerosol stream; in this way the number concentration in a narrow range of mobilities, and therefore particle sizes, can be obtained and the submicrometer particle size distribution is found by stepping (in the case of a DMPS) or continuously scanning (in the case of a SMPS) through the voltage range.

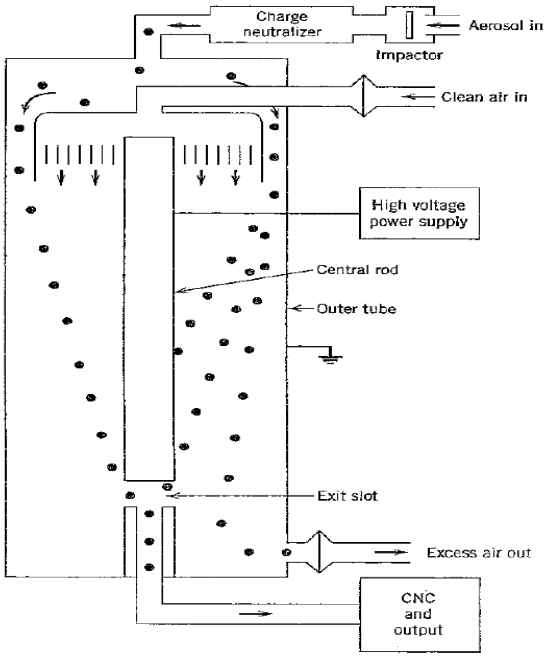

Figure 2.20: Schematic of a Differential Mobility Analyser (from Hinds, 1999).

Figure 2.21: Scanning Mobility Particle Sizer.

2.5 Light scattering instruments

Light scattering paves the way for sensitive devices that return nearly immediate measurements of aerosol particle sizes. Light scattering techniques have the advantage of providing instantaneous information and they cause minimal disturbance to the particles being measured. A disadvantage of light scattering techniques is that scattering may be highly sensitive to small variations of the refractive index, the scattering angle, the

particle shape, which may all lead to erroneous measurements of the particle size.

2.5.1 Photometers

A *transmissometer*, or *light-attenuating photometer*, is an instrument that measures the light extinction through a path length ranging from a few cm up to a few km. Stack transmissometers are used to measure the extinction by the smoke in the stack and they have a focused light source directed across the stack towards a detector.

Care must be taken at several elements. As these instruments measure the light extinction by the smoke in a stack, the light beam should be highly collimated, otherwise the instrument will also detect significant amounts of forward-scattered light. Due to this, at high number concentrations the intensity of the transmitted light may vary in an unpredictable way with concentration. Therefore, a gravimetric calibration can be used if the particle refractive index and size are constant. To eliminate forward scattering, appropriate adjustments must be applied to the pinhole before the detector.

A *photometer* measures the relative particle concentration from combined light scattered by many particles at once. The aerosol flows through the instrument at a certain sample rate and the illumination and collection optics are arranged so that the light scattered at fixed angles reaches the detector. Forward-scattering photometers, i.e. working with angles smaller than 30°, are less sensitive to refractive index.

Photometers may be used in the field of occupational hygiene to measure particle mass concentrations. However, in this case a previous calibration with side-by-side filter samples is essential if the particles present in the environment at issue are different from the manufacturer's calibration aerosol.

2.5.2 Optical Particle Counters (OPCs)

2.5.2.1 Measurement principle

An *optical particle counter* (OPC) is a device that relies on the measurement of scattered light in order to detect and classify a particle (Hinds, 1999). As shown by Figure 2.22, particles are drawn into a sample inlet and flow through a laser beam. In the view volume Mie scattering occurs as particles are passed *one at a time* (with few exceptions) into the laser beam. The laser beam is thin and surrounded by sheath air, so that only one particle at once is illuminated. The laser beam may be further polarised by mean of a condenser

lens. Scattered light from different angles is then collected by a collector lens and forwarded to a photomultiplier tube.

By analysing the height of the electronic pulse it produces, the particle is then classified and a count is added in the proper channel.

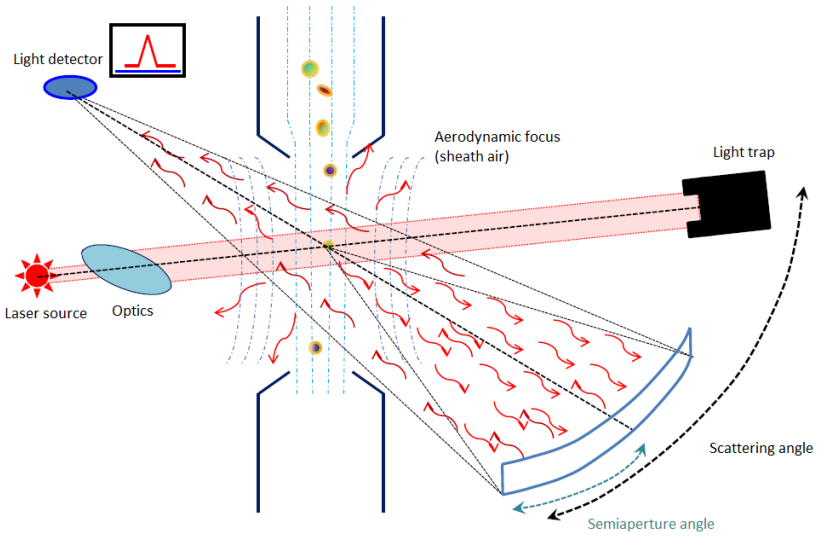

Figure 2.22: Schematic of an OPC. Adapted from Colombi et al. (2012).

This analysis relies on the assumption that scattered light intensity is a monotonic function of particle size, which is not always the case (see Figure 2.7).

Forward scattering is usually the most exploited as it provides the strongest signal, but requires special care to reduce background noise, which is the least at 90°. For this reason the most of the OPCs rely upon 90° scattering. However, forward scattering has a great advantage in that it is primarily diffracted light, which is therefore less sensitive to the refractive index and to whether the particle is absorbing.

2.5.2.2 Critical aspects

The response of an OPC largely depends on the size of the illumination angle, the particle size, the particle shape, the particle refractive index and the pressure inside the view volume. As OPCs are designed to detect small particles, the view volume should have a very small illumination angle, which is the case of laser light.

A non-spherical particle will yield a signal that is fairly different from the one caused by a spherical one. Moreover, if the particle is not well aligned with the laser beam in the view volume, the amount of scattered light will be different from the one that would be observed if the particle were perfectly aligned. Due to this problem, the particle size the

OPC returns may be different from the actual one. For non-spherical particles the amount of scattered light largely depends on the side being illuminated by the laser beam.

As previously mentioned, as the OPC output relies upon Mie scattering, at particle diameters larger than 1 μm more than one particle size will correspond to a given scattering intensity due to the typical intensity undulations of Mie scattering (see Figure 2.7).

The sizing accuracy strongly depends on the refractive index of the test material (Heim et al., 2008). If this is known, the particle size distribution may be easily achieved after a suitable calibration. Usually, the calibration curve (i.e., the relationship between light scattering, signal intensity and particle size) supplied by the manufacturer is based on monodisperse spheres of polystyrene latex (PSL), which have a (real) refractive index of 1.59.

Besides PSL, oil mixtures are also widely deployed for calibration purposes since they are easy to generate and their droplets are usually spherical in shape. An oil usually presents a refractive index whose real part is lower and the imaginary part is greater than their corresponding ones of PSL. This yields a strong reduction in detected light intensity due to a reduced light scattering (because of the lower real part of the refractive index) and an increased light absorption (because of the greater imaginary part).

OPCs are often required to measure number concentrations of particles that are different from the test material and might have, therefore, very different refractive indices. When measuring a particle suspension of different origin and material, it is sometimes assumed that particles have the same refractive number as the medium in which they are suspended (e.g., 1.00 for air, 1.33 for water). On the contrary, as shown in Figure 2.23, when the refractive index is not known a-priori, errors in size estimation may be as big as 140%.

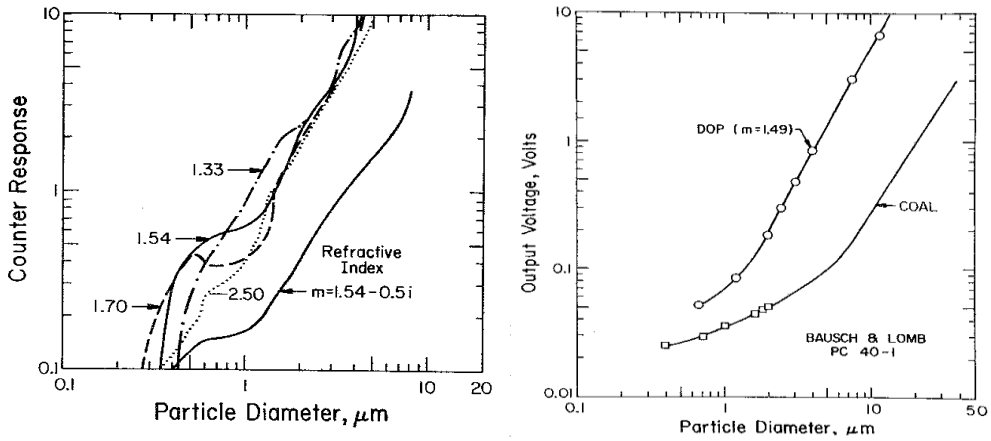

Figure 2.23: Theoretical response (left) and experimental calibration curve (right) of the Bausch and Lomb 40-1A particle counter; the output voltage of the OPC is plotted against the particle diameter at different particle refractive indices (from Liu, 1976).

As OPCs are designed so that particles are passed in the view volume one at a time, coincidence errors occur when more particles flow through the laser beam simultaneously. The resulting spurious signal will yield an underestimation of the particle number concentration and an overestimation of the particle size.

These errors decrease if the flow rate and the beam size are reduced. The latter, however, requires a small aerosol stream diameter, so that nearly all particles will pass through the beam.

In general, OPCs are seriously affected by coincidence errors at low number concentrations (less than 10^7 # L^{-1}) and cannot therefore be deployed for air sampling during severe pollution events, unless the air to be sampled is diluted.

2.5.2.3 Applications

An OPC is a suitable device for air sampling of indoor environment, where the presence of dusts, smokes or any kind of pollutant relating to PM can affect the air quality and therefore impair the health of the people living or working in such environment.

OPCs can therefore be deployed in work environments such as factories, workshops, office rooms or conference halls, especially if these environments are close to sources of pollutions heavily trafficked roads.

In these kinds of environments, the ambient air should be kept under control in order not to affect the health of the people living or working there.

OPCs may also be used for outdoor air samplings as long as the aerosol particle concentration is lower than 10^6-10^7 # L^{-1}. However, in some circumstances they may be used for PM sampling although they do not rely upon the reference (standard gravimetric) method for ambient monitoring (Guide to the Demonstration of Equivalence of Ambient Air Monitoring Methods, 2010).

Indeed, standard gravimetric measurements for the determination of PM_{10} and $PM_{2.5}$ mass concentrations are carried out by sampling the particulate matter on filters and weighing them by means of a balance. Filters should operate at a nominal flow rate of 2300 L hr^{-1} over a sampling period of 24 hr as prescribed by EN 12314 (European Standard, 2014).

New generation OPCs are now equipped with software systems and perform calculations of PM mass concentration automatically. However, this requires assumptions on the particle mass density as OPCs are not designed to directly measure the mass of the sampled particulate matter. Colombi et al. (2013) show how an OPC (Grimm 1.107) can provide useful insight into the PM mass concentration when used in cooperation with gravimetric filter samples. In particular, PM trends returned by the OPC are similar to those extrapolated from filter measurements, yet the mass concentrations evaluated by the OPC significantly underestimate the ones measured through the gravimetric method. This is because the particle density (or density function) used by the OPC software system to extrapolate the mass concentration is based upon the particle amounts and chemical composition of the place where the OPC calibration takes place.

2.5.3 Microscopy

As optical microscopes have a total magnification seldom greater than 500, they are most suitable for counting, observing and sizing solid particles larger than 1 μm.

To examine particles smaller than the limit of resolution of an optical microscope, an electron microscope should instead be used. There exist two types of electron microscopes: *transmission electron microscopes* (TEMs) and *scanning electron microscopes* (SEMs).

The structure of a TEM is similar to that of an optical microscope. Instead of a light source, the TEM uses electrons generated by thermo-ionic effect that are then focussed by magnetic lenses. The interior of the TEM is kept under high vacuum conditions to prevent the scattering of the electron beam by air molecules.

Particles in the electron beam absorb and scatter electrons and finally produce a magnified two-dimensional image, which can be viewed by projecting it onto a fluorescent screen or photographic plate. The limit of resolution of a TEM is usually of the order of some tenths of nm.

Just like the TEM, a SEM utilises electron beams, magnetic lenses and high vacuum but it finally creates a three-dimensional image.

The electronic beam is focussed to a spot of about 0.01 μm in diameter and passed across the sample. This causes secondary electrons to be emitted from the sample's surface. These electrons are then attracted to a detector maintained at a constant positive voltage with respect to the sample. The detector is usually a photomultiplier tube where the electron signal is amplified and converted into an electric signal.

The brightness of the image is therefore made proportional to the number of secondary electrons that reach the detector at a given instant. By tilting the sample with respect to the electron beam, shadows are produced giving a remarkable three-dimensional effect to the image.

The resolution of a SEM is equal to the diameter of the focussed electronic beam, i.e. about 0.01 μm: this is lower than the resolution of a TEM but still fairly higher than the one of an optical microscope. Like the TEM, the SEM is limited to solid, non-volatile particles. To prevent electronic charging on the sample surface, which would affect the electronic beam and therefore distort the image, a thin coating of gold or carbon usually applied before the sample observation at the SEM.

Chapter 3: Materials and Methods

3.1 Aerosol generation

There are several devices devoted to generating aerosol particles. While working, an aerosol generator with high performances should produce aerosol with constant characteristics (diameter, concentration, etc.). Monodisperse aerosols are obtained by means of *vibrating orifices*, *condensation generators* or *spinning-disk generators*. Another way of producing monodisperse aerosols is through the nebulisation of suspensions of spherical polystyrene particles. Such suspensions are available in a wide size range (from 0.038 up to 20 μm) from several commercial sources (Griffiths et al., 1998).

A *nebuliser* produces droplets with small particle size by removing larger droplets by impaction inside the device. In a nebuliser compressed air exits from a small tube at high velocity. The low pressure caused by the Bernoulli effect in the exit region causes the liquid to be drawn into the air stream through a second tube. The liquid exits the tube as a thin filament that is further stretched out as it is accelerated in the air stream, until it breaks into droplets. The spray stream is then directed onto an impaction surface, where larger droplets are deposited and drain back to the liquid reservoir. An example of nebuliser (DeVilbiss, mod. 40) is provided by Figure 3.1.

All of the aforementioned devices require the use of compressed gas (air, nitrogen). A different type of atomiser is the *ultrasonic nebuliser*. This device relies on the ultrasonic waves generated by a piezoelectric crystal that is located near the surface of a small volume of liquid and activated by a direct current supply. The energy causes agitation, thus forming a fountain above the surface of the liquid. Compression waves in the liquid cause capillary waves to form in the fountain, which shatter to form dense aerosol.

Several problems may arise when using polystyrene latex (PSL) aerosols for calibration purposes (Fuchs, 1973). First off the actual size of the particles may be different from the one indicated by the producer. This implies that before an accurate calibration a check-up of the size of the particles should be required.

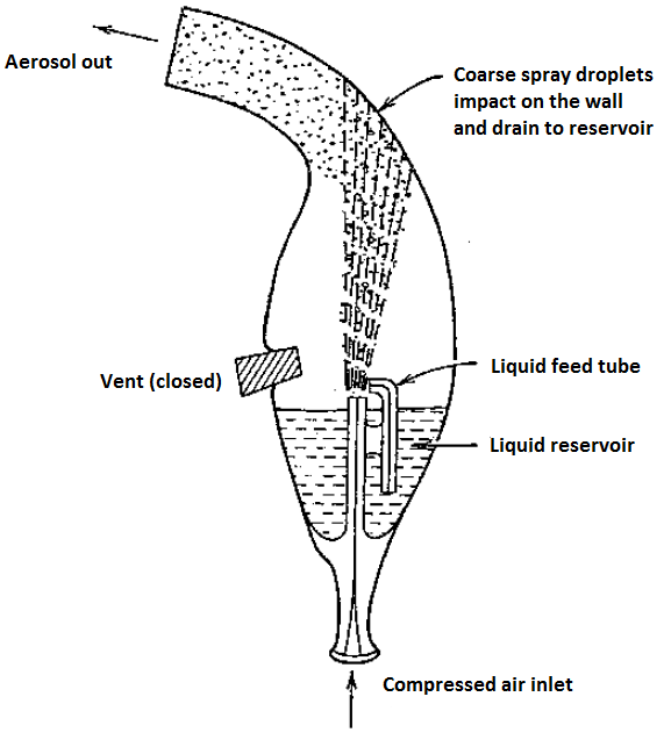

Figure 3.1: Diagram of the DeVilbiss mod. 40 nebuliser. Adapted from Hinds (1999).

In addition to PSL aerosols, additional particles smaller than 100 nm can be generated from impurity of the water, even if Milli-Q water grades are used (Park et al., 2012).

Another critical aspect is the presence of non-volatile stabiliser in the suspension. This is necessary for the stability of the PS particles, which would otherwise quickly coagulate. Therefore, after drying, the resulting particles may either be latex particles covered by a shell of dried stabiliser, or consist of stabiliser only ("empties").

To avoid possible aggregation of PS particles due to the presence of more particles in each droplet, suspensions should have low concentrations (i.e., the dilution should be high) and the droplet diameter should be small. Raabe (1968) found an empirical formula (Equation 3.1) for the dilution factor Y necessary to give a desired singlet ratio R, which is the number of droplet containing single particles relative to the total number of droplets containing particles.

$$Y = \frac{f\ D_{3g}^3 \exp[4.5\ (\ln^2 \sigma_g)\ ]\ [1 - \exp(\ln^2 \sigma_g)]}{(1-R)D_i^3}$$

Equation 3.1

Here f is the volume fraction of individual particles of diameter D_i in the original suspension and D_{3g} is the volume median diameter of the droplet distribution.
In any case, as aggregates are at least twice greater than a single particle, the output signal should be distinguishable from that of single particles.
Another critical aspect is the presence of non-volatile stabiliser in the suspension. This is necessary for the stability of the PS particles, which would otherwise quickly coagulate. Therefore, after drying, the resulting particles may either be latex particles covered by a shell of dried stabiliser, or consist of stabiliser only ("empties").
The tests performed in this work were carried out by using PSL spheres of 0.5, 0.95 and 1.03 μm in diameter produced by Agar Scientific.

3.2 Aerosol generators used for this study

In this study two different aerosol generators were used. Tests were initially conducted through a home-made aerosol generation apparatus, including an ultra-sonic nebuliser (Projet, Artsana), a silica gel column to evaporate water droplets and an air dilution system. Afterwards, a commercial aerosol generator (AGK 2000, Palas GmbH) was made available and used for further tests. In the following the main features of these two aerosol generation systems are described.

a) The Projet generator is an ultrasonic nebuliser for aerosol therapy produced by Artsana S.p.a (see Figure 3.2). It can produce monodisperse and polydisperse aerosols at a nearly constant rate for about 15 min in a row, which corresponds to the maximum time of ongoing use. Fresh water is used to fill the water reservoir, in which the piezoelectric crystal is located. An amount of PSL suspension is diluted according to Equation 3.1 in Milli-Q water and poured into a plastic support (capacity: approximately 10 mL) positioned inside the reservoir. The casing is covered by a removable buckler lid.
The device is activated by connecting it to direct current and pressing the proper start button. It is provided with a flow regulator, by which the nebulisation rate may be varied (3 mL every 4-7 minutes depending on the supply). The nebulised suspension is conveyed outward by means of an exit nozzle.

Figure 3.2: Projet aerosol generator, Artsana S.p.a.

b) The AGK 2000 commercial aerosol generator is a liquid nebuliser for suspensions produced by Palas GmbH. It consists of a removable liquid reservoir containing the suspension to nebulise, a binary pressure nozzle, a cyclone and a pressure minimiser. One branch of the binary pressure nozzle conveys compressed air towards the liquid reservoir to draw the suspension towards the cyclone, while the other conveys the compressed air towards the cyclone for drying purposes. Figure 3.3 shows a picture of the generator, while Figure 3.4 is a schematic of the working principle.

The suspension is nebulised at a rate depending on the pressure of the compressed air (17 mL hr^{-1} at a working pressure of 2 bar). In this work, all tests were performed with pressures between 1.5 and 3.0 bar, corresponding to a total air inflow between 14.4 and 24.0 L min^{-1}.

Figure 3.3: AGK 2000 aerosol generator, Palas GmbH.

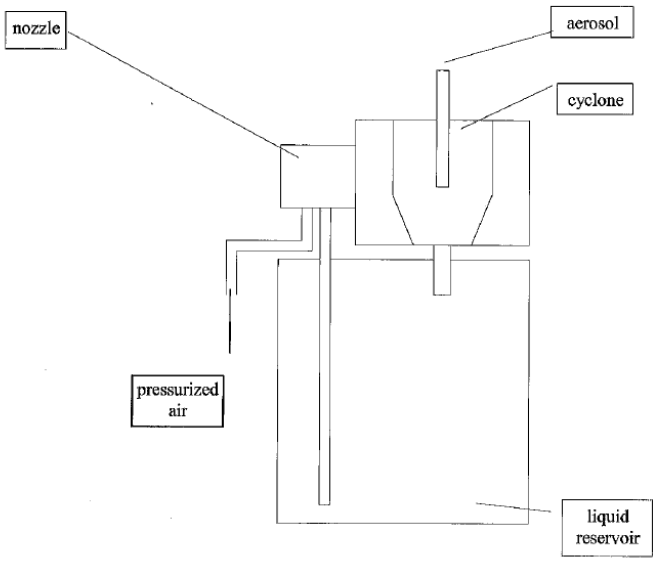

Figure 3.4: Schematic of AGK 2000, Palas GmbH.

3.3 Optical Particle Counters used for this study

Three different OPCs were used to sample the aerosol particles produced by the aforementioned aerosol generators.

The first one is an optical particle counter widely used in air quality monitoring (Portable Laser Aerosolspectrometer Dust Monitor Model 1.108, GRIMM AEROSOL Technik GmbH & Co.).

The second one is an OPC of new design that might be used in participating monitoring programs (CompactOPC N1, Alphasense). Over the last years, citizen science approaches have transformed scientific data collection and analysis in some areas, mostly due to

technological advances and the increased willingness of the general public to be involved in the scientific practice. Technology now enables the development of low-cost, miniaturised and portable detectors also for particulate matter measurements, like this OPC. This allows the setup of compact monitoring stations for smart cities applications.
Finally, the last instrument is an optical particle counter usually deployed in clean air monitoring (Laser Particle Sensor, Kanomax).
In the following the main features of these detectors are described.

a) The Portable Laser Aerosolspectrometer Dust Monitor Model 1.108 (hereafter GRM) is an optical particle counter produced by GRIMM AEROSOL Technik GmbH & Co. KG and widely used in air quality researches. It is provided with a pump sucking air at a rate of (1.2± 0.06) L min^{-1}. The pump draws particles into a viewing volume where a laser source (λ = 780 nm) is located. The scattered light due to particles passing in the view volume is directed (Heim et al., 2008) onto two mirrors (a parabolic and an additional one) and then reflected back to a detector diode. The scattering angle between the laser direction and the plane where the mirror and the detector diode lie is 90°. The parabolic mirror is wide (120°), while the second mirror is thinner (18°). This increases the total amount of light detected by the detector diode, improves the signal-to-noise ratio and smooths out Mie scattering undulations caused by the monochromatic illumination. Figure 3.5 is a picture of this OPC and Table 3.1 reports its specifics.
The GRM is designed so that more than one particle at a time can enter the view volume; it directly measures, therefore, the particle number concentrations. However, the design of the view volume (the mirror system) increases the coincidence error and decreases the upper concentration limit ($2*10^6$ # L^{-1}).
The signal created by the detector diode after a light pulse is then amplified and classified into 15 different size channels (see Table 3.2). Data output can be averaged in intervals from 6 seconds up to 60 minutes. Data may be displayed as number concentrations (# L^{-1}) and mass concentrations (µg m^{-3}). A Windows software is provided to visualise measurement's results in real time and save data in text format; this software also calculates dust mass fraction in terms of occupational health.
Particulate mass fractions (PM_{10}, $PM_{2.5}$ and PM_1) are also calculated but are not in compliance with EU Standards for Particulate Matter (see Table 1.1) or US EPA. The

pump also provides the viewing chamber with rinsing air, which protects the laser optics from pollution and is used as particle-free reference air during the instrument's self-tests.

Inlet flow rate [L min^{-1}]	1.2 +/- 0.06
Weight [kg]	Approx. 3
Size [cm]	23.5x13.5x6
Measured size range [µm]	0.3-20

Table 3.1: Specifics of the Portable Laser Aerospectrometer Dust Monitor (GRM).

Figure 3.5: Portable Laser Aerospectrometer Dust Monitor (GRM).

channel	size range [µm]
1	0.30-0.40
2	0.40-0.50
3	0.50-0.65
4	0.65-0.80
5	0.80-1.0
6	1.0-1.6
7	1.6-2.0
8	2.0-3.0
9	3.0-4.0
10	4.0-5.0
11	5.0-7.5
12	7.5-10.0
13	10.0-15.0
14	15.0-20.0
15	>20.0

Table 3.2: Channel division of the Portable Laser Aerospectrometer Dust Monitor (GRM).

b) The CompactOPC N1 (hereafter COPC) is an OPC produced by Alphasense. It is a small, light and low-cost instrument and is provided with a USB cable requiring a PC USB socket. From this cable, the instrument withdraws the working electrical current. A picture of this OPC is represented by Figure 3.6, while other specifics are reported by Table 3.3. A software allows the user to visualise and save data, which are only displayed as counts/s and classified into 16 channel sizes or bins (see Table 3.4). Additionally, the software also reports temperature and pressure data and performs automatic calculations of PM concentrations.

This instrument is provided with a small view chamber and small fan sucking air at a rate of 0.15 L min^{-1} according to the producer. The user manual does not provide the uncertainty relating to this parameter. If number concentrations instead of counts are requested, the counts as read out from the instrument should be divided by the sample

flow rate. Because a correct knowledge of the sample flow rate of an OPC is mandatory in any measurement, a measure of the sample flow rate of the COPC was carried out.
For this OPC this measurement could not be directly carried out by means of a calibrated soap bubble flowmeter as it has a very low sample flow. An electronic flowmeter (Hastings) was calibrated by connecting it at a pump drawing air at a flow rate as read out from a rotameter (Asa Srl) with a full scale of 4 L hr^{-1} and the distance between two notches corresponding to 2 L hr^{-1}. The COPC's sample flow rate was measured by the electronic flowmeter; the final result yielded (12 $\pm$ 2) L hr^{-1}, i.e. (0.20 $\pm$ 0.03) L min^{-1}. The uncertainty on the measurement was assumed to be equal to the distance between two notches in the rotameter. Hereafter, this value will be used to convert all counts recorded by the COPC into number concentrations and the uncertainty will be deployed to calculate the errors relating to this conversion.

Inlet flow rate [L min^{-1}]	0.2 $\pm$ 0.03
Weight [kg]	0.106
Size [cm]	6x8x8
Measured size range [µm]	0.38-17.23

Table 3.3: Specifics of the CompactOPC N1 (COPC), Alphasense.

Figure 3.6: CompactOPC N1 (COPC), Alphasense.

Bin	**Size range [µm]**
0	0.38-0.52
1	0.52-0.75
2	0.75-1
3	1-1.25
4	1.25-1.49
5	1.49-2
6	2-2.99
7	2.99-4
8	4-5
9	5-6.5
10	6.5-8
11	8-10
12	10-12
13	12-14
14	14-16
15	16-17.23

Table 3.4: Channel division of the CompactOPC N1 (COPC), Alphasense.

c) The Laser Particle Sensor (hereafter LPS; see Figure 3.7) is an OPC produced by Kanomax and distributed in Italy by Pollution Clean Air Systems S.p.A. It classifies particles into two channels only and the maximum number concentration that can be correctly sampled is 35300 # L^{-1}. This instrument is generally used for indoor air and

clean room monitoring. In normal working conditions it requires a pump to suck air at a flow rate of (2.83 ± 0.14) L min^{-1}, as this instrument is not provided with an internal pump. Therefore in all tests relating to this work this instrument was always connected to a pump (BRAVO, Tecora) drawing air at a rate of 2.83 L min^{-1}.

The instrument is provided with a software that allows the user to visualise and save data. Four models for this instrument exist: mod. 3714-00, 3714-01, 3715-00 and 3715-01. The difference between the four models is in the sampled size range and the option of monitoring the flow speed (Laser Particle Sensor – Modello 3714-00/-01 3715-00/-01 - Manuale di Istruzioni). Table 3.5 reports the specifics of mod. 3714-00 and 3715-00; the latter was used for this work.

Figure 3.7: Laser Particle Sensor (LPS) mod. 3715-00, Kanomax.

Model	3714-00	3715-00
Weight [kg]	Approx. 0.5	Approx. 0.5
Sample flow [L min^{-1}]	2.83 ± 0.14	2.83 ± 0.14
Size [cm]	7x12x4	7x12x4
Channel 1 size range [µm]	0.3-0.5	0.5-5
Channel 2 size range [µm]	> 0.5	> 5

Table 3.5: Specifics of the Laser Particle Sensor, mod. 3714-00 and 3715-00.

3.4 Reference Method

3.4.1 Description

To state whether the output of an OPC is correct, one should know the actual particle concentration. This can be done by collecting the particles onto an absolute filter during the OPC measurement and after the sampling counter them at a SEM.

To accomplish this task, during all tests with PSL particles, a parallel sampling with an absolute filter (Nuclepore; porosity: 0.22 µm) was carried out by means of a membrane pump (Reciprotor Edwards). Before counting the particles at the SEM, each filter's piece was stuck onto a stub; all stubs were then inserted into a sputter coater in order to cover

the specimens with a thin layer of gold. This was done to prevent specimen's charging with an electron beam in conventional SEM mode (high vacuum, high voltage).

By counting the particles deposited onto the specimens, the total number of particles deposited onto the filter can be evaluated; by dividing this results by the sampled volume, a number concentration is obtained, which may act as a reference number concentration for the OPC.

3.4.2 Particle concentrations obtained through SEM observations

Once the particles were identified at the SEM, a certain number of fields **M** (usually some tenths) was observed. Each field consisted of a rectangle of sides **a** (18.8 cm) and **b** (14.2 cm). By dividing the magnification of the SEM (3000 or 6000 depending on the case) by the area of this rectangle, a conversion factor **z** could be calculated.

The total observed area $\mathbf{A_S}$ was obtained by summing the areas of each of the **M** observed fields. By dividing the sum of all particles **n** viewed in all fields (at the SEM) by $\mathbf{A_S}$ and multiplying this value by the actual filter's area $\mathbf{A_F}$, the total number of particles deposited onto the filter during the measurement could be evaluated after making the assumption of homogeneous deposition. By dividing this value by the sampling rate **Q** (6.5 L min^{-1}) and the timespan of the measurement **t** (usually about 20 min) a number concentration $\mathbf{C_f}$ was obtained.

As the filter sampling area was a circle of diameter **d**, this yields:

$$C_f = \frac{n}{Q\ t}\frac{A_F}{A_S} = \frac{\pi}{M}\frac{n}{Q\ t}\ \frac{d^2}{4}\ \frac{z^2}{a\ b}$$

Equation 3.2

The uncertainty on $\mathbf{C_f}$ was calculated through error propagation, which yielded:

$$\sigma_{Cf} = \sqrt{\sum_i \left(\frac{\partial C_f}{\partial x_i}\right)^2 \sigma_i^2}$$

Equation 3.3

where $\mathbf{x_i}$ indicates each of the variables on which $\mathbf{C_f}$ depends, i.e. **n**, **Q**, **t**, **d**, **z**, **a** and **b**, while $\boldsymbol{\sigma_i}$ refers to the error associated with each of the aforementioned dependencies.

As **a** and **b** were measured by means of a ruler, the corresponding errors were considered to be equal to the distance between two ruler notches, i.e. 0.1 cm. Similarly, the diameter of the filter **d** was measured by a Vernier scale and the error associated with this measurement was assumed to be equal to the smaller distance this instrument could size; this yielded **d** = (3.5 $\pm$ 0.5) cm.

To find **z**, the SEM's software reported a segment of length **h** representing the actual distance observed at a given magnification. For instance, at a magnification of about 6000 (as reported by the SEM's software), the segment was 6.2 cm long and reported an actual length of 10 μm, thus yielding **z** = 6200. As the length of this segment was measured by means of a ruler, once again the error of this measurement was assumed to be equal to the distance between two ruler notches, i.e. for **h** = 6.2 cm the error was 0.1 cm and consequently **z** = 6200 $\pm$ 100. Instead, when using a magnification of 3000, the same calculations yielded **z** = 3030 $\pm$ 100.

As **n** was found by directly counting the particles deposited onto the filter, it was assumed to be a rare event and thus follow Poisson statistics; the error associated to **n** was therefore assumed to be equal to the square root of **n**. Great uncertainties were often associated to the pump's flow rate **Q**, as this was never constant but turned out to oscillate around a mean value. The error associated with this parameter was assumed to be equal to one third of the largest oscillations, i.e. with a flow rate of 6.5 L min^{-1} the oscillations could be as big as 1 L min^{-1}, thus yielding a final value of **Q** = (6.5 $\pm$ 0.3) L min^{-1}.

The error associated with **t** was given by the chronometer and assumed to be equal to 1 s. Finally, no error was associated with **M**, as it represents the exact number of viewed fields.

3.4.3 Reading out the number concentration from the OPCs

As for the OPC, by assuming the production of PSL to be nearly constant in time, a mean number concentration **C** was achieved by dividing the mean value of the counts (**n**) over the sampled volume **V**.

$$C = \frac{n}{V}$$

Equation 3.4

The error on **C** ($\boldsymbol{\sigma_c}$) was calculated once again through error propagation.

$$\sigma_C = \sqrt{\left(\frac{\partial C}{\partial n}\right)\sigma_n^2 + \left(\frac{\partial C}{\partial V}\right)\sigma_V^2}$$

Equation 3.5

Here $\boldsymbol{\sigma_V}$ is the error on the instrument's sample flow as reported in the tables of chapter 3.3, while $\boldsymbol{\sigma_n}$ is the error associated with **n**. As the instrument's readout should only be dependent on the aerosol generation by the source and the latter was classified as a rare event, $\boldsymbol{\sigma_n}$ was set equal to the square root of **n**.
Specifically, the error on the counts $\boldsymbol{\sigma_n}$ was not considered for the GRM's output, as this OPC directly returns a particle number concentration averaged over a certain period.

3.5 Data Handling

3.5.1 The lognormal distribution

Most of the aerosol atmospheric distribution size can be described by using a lognormal distribution, i.e. a Gaussian distribution based on a logarithmic scale (Junge, 1955). The lognormal distribution is completely described by the geometric mean d_g and the geometric standard deviation σ_g, which are defined as follows (Hinds, 1999):

$$d_g = \left(\prod_{i=1}^{N} d_i\right)^{\frac{1}{N}}$$

Equation 3.6

$$\ln \sigma_g = \left(\frac{\sum_i \left(\ln d_i - \ln d_g \right)^2}{N} \right)^{\frac{1}{2}}$$

Equation 3.7

where d_i is the size of a single particle and N is the number of particles belonging to the distribution.

In count distributions the geometric mean is replaced by the count median diameter CMD, which corresponds to the fiftieth percentile of the count distribution, i.e. the size for which the cumulative fraction of the distribution equals 0.5. For this reason, the CMD is also denoted by $d_{50\%}$.

However, if the count distribution is assumed to be lognormal, then CMD = d_g and the geometric standard deviation is found as

$$\ln(\sigma_g) = \ln(d_{84\%}) - \ln(d_{50\%})$$

Equation 3.8

where $d_{84\%}$ indicates the size for which the cumulative fraction of the distribution equals 0.84.

For most purposes, a monodisperse aerosol is defined as an aerosol that has σ_g less than 1.2; geometric standard deviations greater than 1.2 indicate a polydisperse aerosol (Hinds, 1999).

3.5.2 Normalised Histograms

To compare the output of two OPCs is not always straightforward, as their channel divisions may be different. Moreover, if one wishes to obtain the particle distribution by simply looking at the output of an OPC, the result will be dependent on the width of each channel (size resolution). As observed in Chapter 3.2, at small particle sizes (less than 1 μm) the channel width is usually small, while at large particle sizes (greater than 1 μm) the channel width becomes larger and larger. This is because most of the size intervals follow a logarithmic trend.

To overcome these problems, one may resort to normalised histograms, i.e. divide the instrument's readout in a given channel by the channel width, thus obtaining a histogram reporting a frequency (or number concentration) per unit width. A variant to this proceeding consists of dividing the channel readout by the logarithm (usually to base 10) of the channel width, usually denoted by $\Delta N/\Delta \log(d)$ or in similar ways.

The latter is often deployed when dealing with size distributions resembling a lognormal distribution and was therefore used in this work to compare the output of different OPCs. Instead, as for the comparison of OPC outputs with the particle concentration obtained from the filter samplings, the direct reading from a single channel or the sum of several channels was considered.

Chapter 4: Experimental results

In this chapter experimental results relating to the inter-comparison tests carried out with each OPC are presented. Initially, tests with indoor aerosol were conducted. Afterwards tests with monodisperse aerosol of 0.5, 0.95 and 1.03 μm in diameter were carried out with two different aerosol generation systems.

4.1 Indoor measurements

4.1.1 Background concentration

Before starting the comparison among the OPCs, a preliminary test with clean air was carried out. The experimental scheme is shown in Fig 4.1.

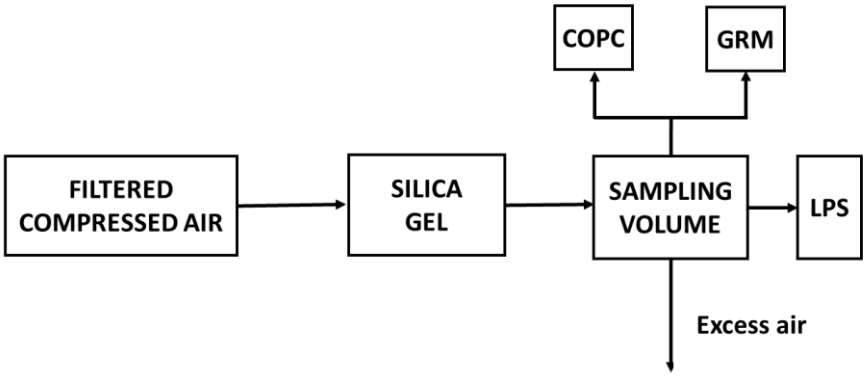

Figure 4.1: Experimental setup for measuring the background concentration in clean air conditions.

Clean air was conveyed towards a silica gel column and then into the sampling volume. Mean values and errors on the particle number concentrations were calculated according to Equation 3.4 and Equation 3.5 (Chapter 3.4.3). In these conditions all OPCs measured very low particle number concentrations (see Table 4.1).

OPC	**Particle number concentration [# L^{-1}]**
COPC	0.06 ± 0.27
GRM	32 ± 2
LPS	42 ± 209

Table 4.1: Particle number concentration measured by each OPC in clean air conditions.

4.1.2 Samplings in indoor environment

Samplings of indoor air under different conditions were carried out with the OPCs running in parallel to test the counting efficiency of each OPC. During these samplings the particle number concentrations as read out from the GRM were used as reference ones. The setup of each experimental configuration is reported in Table 4.2.

Test Number	Setup
1	All OPCs drawing laboratory air from the sampling volume according to Figure 4.2
2	All OPCs positioned in the environment
3	Same as Test 2
4	COPC in a sealed box with a pump drawing air at 1 L min^{-1}; LPS and GRM drawing air from a sampling volume
5	COPC in a sealed box with a pump drawing air at 3 L min^{-1}; LPS and GRM drawing air from a sampling volume
6	Same as Test 5

Table 4.2: Configuration setup of each indoor sampling.

To evaluate the relative performances and in order to compare the OPC output, the mean particle number concentrations in the size range 0.5-5 μm were considered. Ratios between the different OPC particle number concentration outputs were also considered; namely, the ratio of the results achieved from the COPC to the ones obtained from the GRM was termed COPC/GRM and similarly LPS/GRM (COPC/LPS) refers to the ratio of the results as read out from the LPS (COPC) to the ones obtained from the GRM (LPS). As for COPC/GRM, the 0.4-0.5 μm size range was also considered. As the channels of the two instruments are not perfectly coincident, the particle number concentrations relating to those channels were normalised by the logarithm width of each size bin.

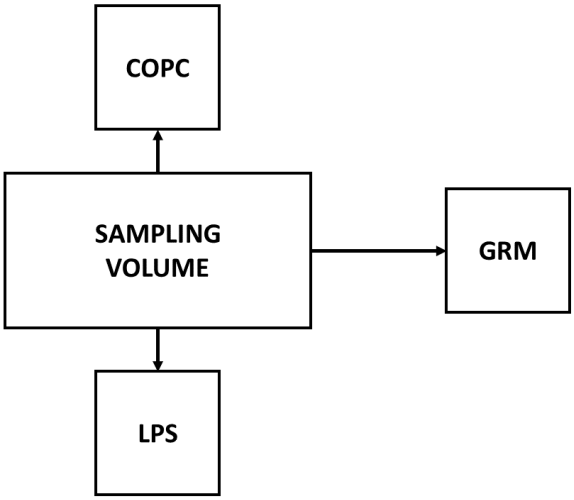

Figure 4.2: Schematic of Test 1.

In *Test 2* and *3* the OPCs were left free to sample the indoor air from the laboratory. The configuration of these two tests can be taken as a standard sampling condition and can be used to evaluate the performance of the COPC. An example of the size distribution of *Test 2* as read out from the COPC and the GRM is reported in Figure 4.3 and 4.4 respectively; it is clearly observed that most of the particles are in the first size bins below 0.5 µm. The error bars in the figures (and in the ones hereafter) refer to the errors on each measurement as calculated from Equation 3.5.

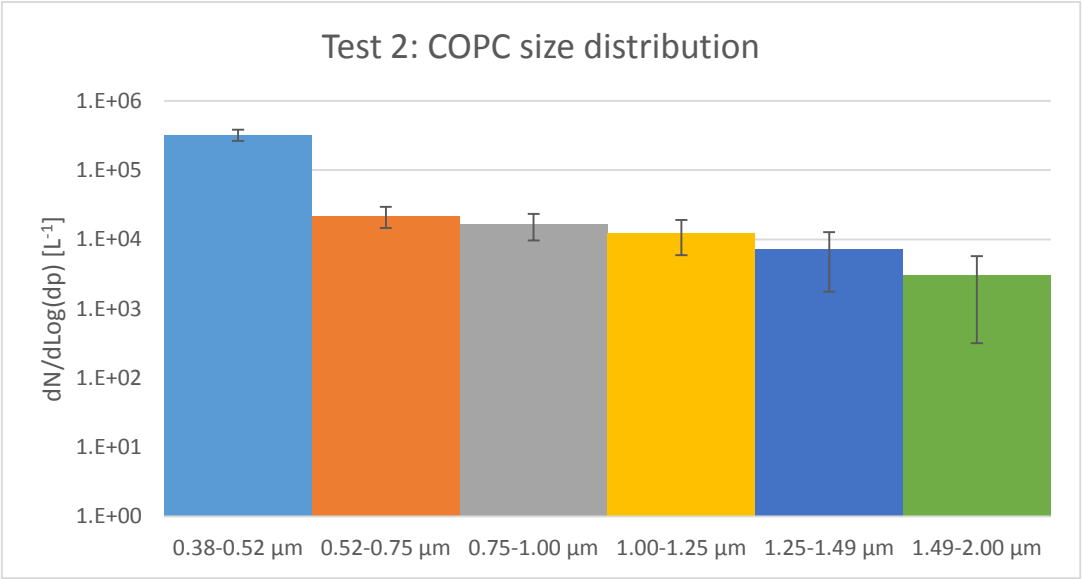

Figure 4.3: Particle size distribution as read out from the COPC during Test 2.

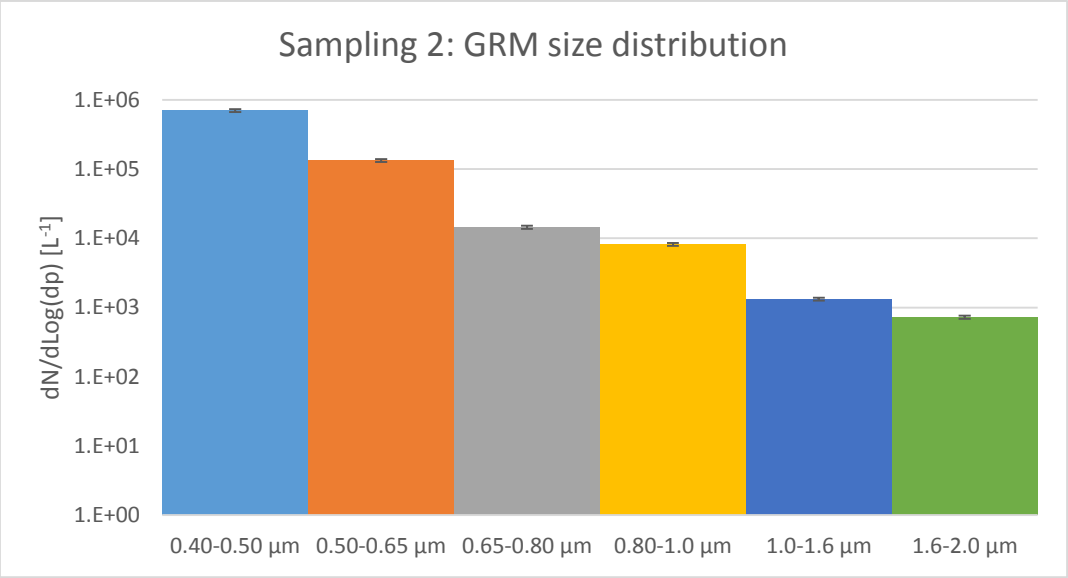

Figure 4.4: Particle size distribution as read out from the GRM during Test 2.

In *Test 4* the LPS and the GRM were in the same configuration as *Test 1*, while the COPC was positioned in a sealed box with a pump drawing air at a rate of 1 L min^{-1}. This configuration was set up to verify if the COPC's fan can draw air from the tube connected to the sampling volume (as *Test 1*) and keep a constant flow rate. *Test 5* and *6* share the same configuration as *Test 4*, but the pump's flow rate was set equal to 3 L min^{-1}. The experimental setup of *Test 4*, *5* and *6* is shown in Figure 4.5. Mean values and errors as calculated from Equation 3.4 and Equation 3.5 are summarised in Table 4.3.

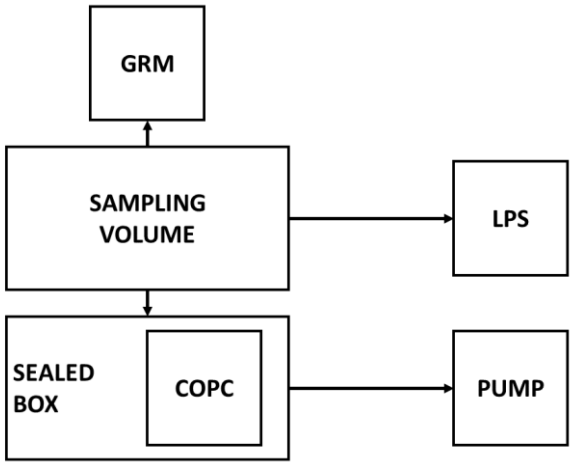

Figure 4.5: Experimental setup of Test 4, 5 and 6. In Test 4 the pump's drawing rate is set to 1 L min^{-1}, while in Test 5 and 6 it is set to 3 L min^{-1}.

OPC	Particle number concentration [# L^{-1}]				
	COPC		GRM		LPS
Test number	**Size range: 0.4-0.5 µm**	**Size range: 0.5-5 µm**	**Size range: 0.4-0.5 µm**	**Size range: 0.5-5 µm**	**Size range: 0.5-5 µm**
1	$(5.8 \pm 1.8)10^3$	$(0.9 \pm 0.6)10^3$	$(11.2 \pm 0.6)10^3$	$(4.2 \pm 0.2)10^3$	$(6.2 \pm 0.4)10^3$
2	$(44.0 \pm 10.7)10^3$	$(8.0 \pm 2.3)10^3$	$(67.7 \pm 3.4)10^3$	$(18.9 \pm 0.9)10^3$	$(30.9 \pm 3.9)10^3$
3	$(22.5 \pm 4.7)10^3$	$(4.1 \pm 1.3)10^3$	$(29.9 \pm 1.5)10^3$	$(10.0 \pm 0.5)10^3$	$(15.7 \pm 1.1)10^3$
4	$(1.2 \pm 0.6)10^3$	$(0.3 \pm 0.3)10^3$	$(2.1 \pm 0.1)10^3$	$(1.3 \pm 0.1)10^3$	$(1.7 \pm 0.2)10^3$
5	$(1.7 \pm 0.8)10^3$	$(0.6 \pm 0.5)10^3$	$(2.4 \pm 0.1)10^3$	$(1.5 \pm 0.1)10^3$	$(2.1 \pm 0.3)10^3$
6	$(6.9 \pm 1.9)10^3$	$(1.5 \pm 0.7)10^3$	$(9.3 \pm 0.5)10^3$	$(3.7 \pm 0.2)10^3$	$(5.6 \pm 0.5)10^3$

Table 4.3: Particle number concentrations as read out from each instrument in the two considered size ranges (0.4-0.5 µm and 0.5-5 µm) in each sampling.

In each of the indoor tests the LPS/GRM ratio (0.5-5 µm) does not change significantly, its average value being 1.49. This indicates that the particle number concentrations reported by the LPS is higher than the GRM ones (see Figure 4.6).

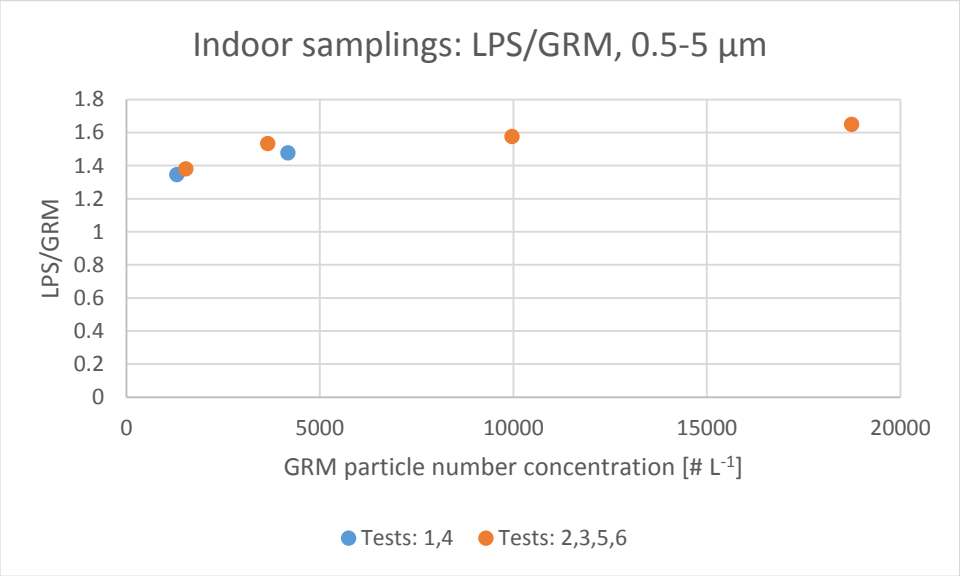

Figure 4.6: Trend of the LPS/GRM ratio in the 0.5-5 µm size range versus the particle number concentration recorded by the GRM during different tests.

On the contrary, the COPC/GRM ratio was always fairly smaller than one. Figure 4.7 shows the COPC/GRM ratio for the 0.5-5 µm size range; it can be observed that in this interval the COPC always underestimated the particle number concentration reported by the GRM. However, while in *Test 2*, *3*, *5* and *6* this ratio assumed similar values (around 0.4), in *Test 1* and *4* it dropped down to about 0.22.

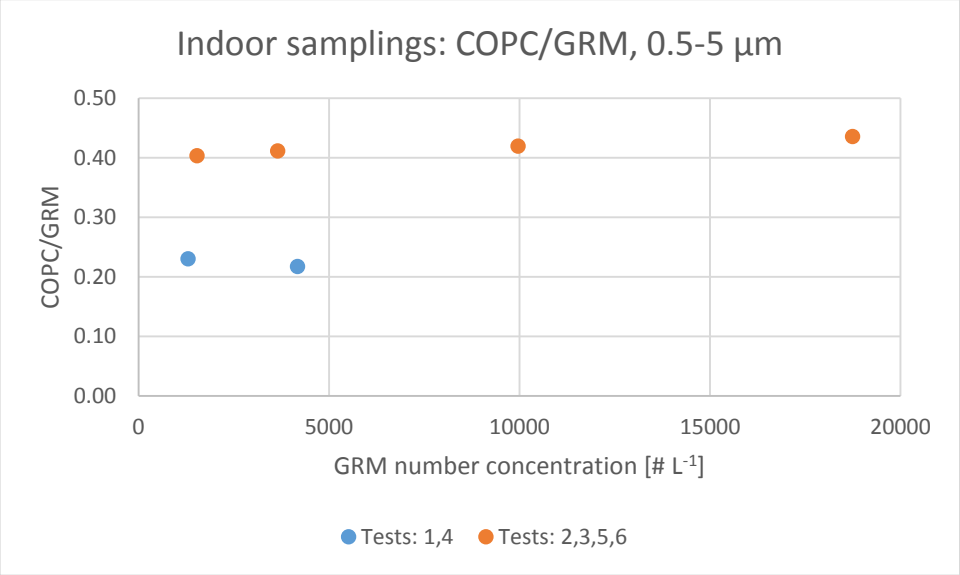

Figure 4.7: Trend of the COPC/GRM ratio in the 0.5-5 µm size range versus the particle number concentration recorded by the GRM during different tests.

Figure 4.8 shows the COPC/GRM ratio in the 0.4-0.5 µm size range. The behaviour is similar to the one observed for the ratio in the 0.5-5 µm size range and the conclusions are similar.

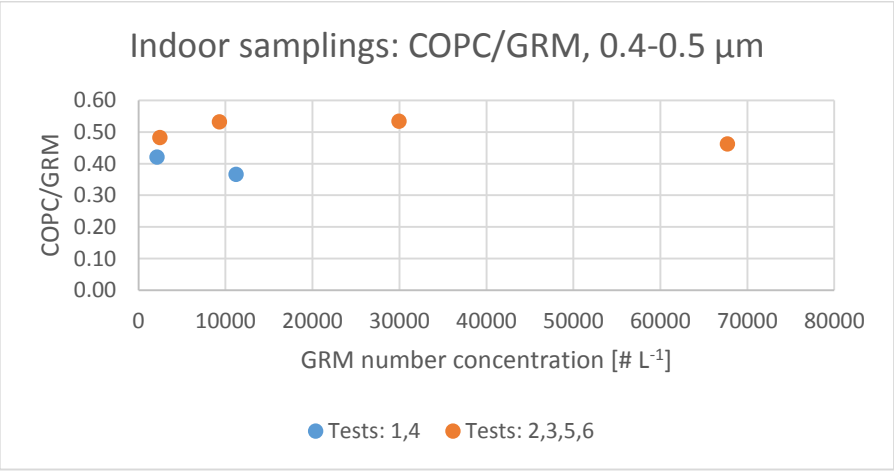

Figure 4.8: Trend of the COPC/GRM ratio in the 0.4-0.5 µm size range versus the particle number concentration recorded by the GRM during different tests.

Finally, the trend shown by the COPC/LPS ratio in the 0.5-5 µm size range (Figure 4.9) is similar to the one reported by the COPC/GRM ratio, i.e. the results of *Test 2*, *3*, *5* and *6* are similar, while the results of *Test 1* are comparable with the ones of *Test 4*.

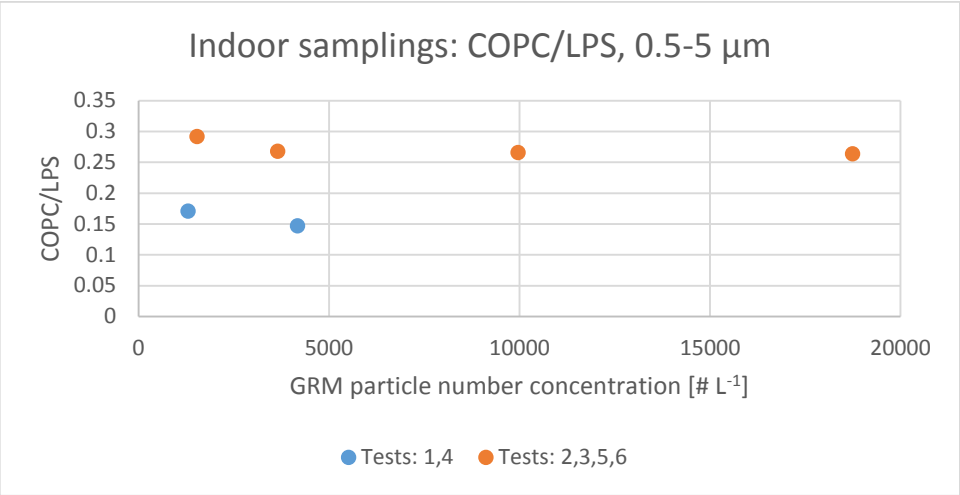

Figure 4.9: Trend of the COPC/LPS ratio in the 0.5-5 µm size range versus the particle number concentration recorded by the GRM during different tests.

As pointed out before, the reason for this variability could be the COPC's fan, which could not keep a well defined and constant flow rate, specifically in case of sampling from a line. Therefore in *Test 4* the COPC was inserted into a sealed box with a pump drawing air at a rate of 1 L min^{-1}. However, the results did not show differences in behaviour compared to *Test 1*; it was therefore decided to raise the pump's flow rate to 3 L min^{-1} (*Test 5* and *Test 6*): in these conditions the COPC/GRM and COPC/LPS ratios appeared to be comparable with those found in *Tests 2* and *3*.

In conclusion, by taking the GRM as the reference device, the COPC always underestimated the particle number concentration, while the LPS always overestimated it. In addition, the ratios of the particle number concentrations reported by each instrument suggested that the output of the GRM and the LPS does not depend on the experimental configuration, while the output of the COPC does. This implies that an accurate choice for the experimental setup is probably essential to carry out correct measurements with the COPC. These results point out that in order to use the COPC with monodisperse aerosol, which requires taking aerosol from a sampling line, it is necessary to assist the instrument's aspiration with a pump to avoid a high underestimation of the particle number concentration.

4.2 Response time

Before starting samplings with monodisperse aerosol it is necessary to evaluate the response time of each instrument. The experimental setup is the same as *Tests 5* and *6* (Figure 4.5). After an initial startup, during which all OPCs were observed to measure a nearly constant particle number concentration, a candle was put close to the inlet of the sampling volume and then immediately removed. The candle smoke introduced a very short peak of particle concentration that was detected by all OPCs.

The OPCs were then let sample the air of the sampling volume until the number concentrations became similar to those measured before the smoke signal. The signal A can be thought of as pulse governed by the following power law.

$$A(t) = A_0 e^{t/\tau}$$

Equation 4.1

Here τ is the time constant (i.e., the response time) and A_0 is A(t = 0). As t = 0 can be chosen with no particular limitations (the point should only lie within the rising part of the signal), by looking at the rising signal, one can consider A_{10} and A_{90} , the values corresponding to 10% and 90% of the total rise, and the times t_{10} and t_{90} at which these values were registered.

The rise time τ_{rise} was then calculated through the following formula.

$$\tau_{rise} = \frac{t_{90} - t_{10}}{\ln(\frac{A_{90}}{A_{10}})}$$

Equation 4.2

As this discussion holds for the falling signal as well, Equation 4.2 was also used to calculate the fall time τ_{fall}, with A_{10}, A_{90}, t_{10} and t_{90} now referring to the falling part of the signal.

Hereafter the procedure for the experimental calculation of τ_{rise} and τ_{fall} is reported. In the rise and fall curves, the background number concentration, which was assumed to be equal to the last measured value before the rise, was subtracted from each measured value. Then the exact values for A_{90} and A_{10} for both rise and fall were calculated.

In practice, as it is almost impossible that an instrument samples the number concentration in the exact moment when the rise (or the fall) curve is at the 90% or 10% of its total

development, it was decided to select the values measured by each instrument that approached A_{90} and A_{10} the most. As for t_{90} and t_{10}, they were chosen as the time values corresponding to the selected values for A_{90} and A_{10}. Results are summarised in Table 4.4.

OPC	size range [µm]	τ_{rise} [s]	τ_{fall} [s]
COPC	0.38-0.52	1.8	76.7
	0.52-0.75	10.9	45.6
	0.5-5	1.8	32.4
GRM	0.3-0.4	21.9	19.0
	0.4-0.5	19.6	16.5
	0.5-0.65	21.9	17.8
	0.5-5	21.8	17.2
LPS	0.5-5	17.0	49.8

Table 4.4: Response times of each OPC in different size ranges.

Results show that the response time of each OPC is in the order of some tenths of seconds, which is fairly smaller than the average duration of a test with PSL spheres (about 20 min).

4.3 Measurements with PSL particles

Experiments with monodisperse particles were carried out with the particle counters to measure their response under controlled exposure conditions. Specifically, particles of 0.5 µm, 0.95 µm and 1.03 µm in size were used. In parallel, also samplings with an absolute filter were carried out to allow the observation and counting of the particles under SEM investigations. In this way, an absolute particle number concentration can be inferred.

To compare the output of the OPCs with one another, as already done with indoor aerosol, normalised concentration values were achieved by dividing the concentrations values reported by each instrument by the logarithm of the size interval; afterwards, the COPC/GRM ratio was defined as the normalised concentration value reported by the COPC to the one reported by the GRM. In a similar way the LPS/GRM and COPC/LPS ratios were defined.

4.3.1 Experimental setup

For the following tests the experimental setup shown by Fig 4.10 was used. The PSL suspension was atomised by the nebuliser (Projet) and mixed with clean air (air flow: 20 L min^{-1}) in a mixing volume and dried in a silica gel column. At the exit of this box, particles were conveyed to the sampling volume and hence to the three OPCs and the filter. The COPC was located in a sealed box and equipped with a pump with a drawing rate of 3 L min^{-1} as previously described (Chapter 4.1.2). Results will be given for each particle class.

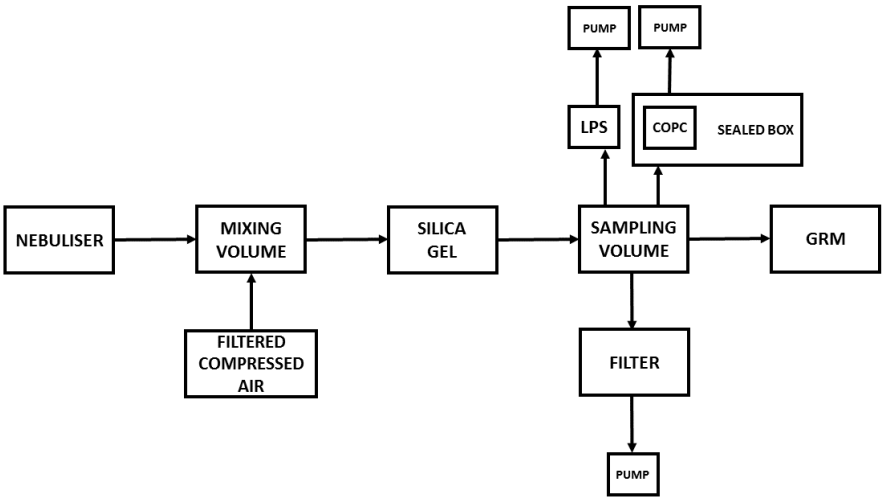

Figure 4.10: Diagram of the experimental apparatus.

4.3.2 Tests with 0.5 μm calibrated particles

A preliminary test was conducted with the GRM only and, in parallel, with a filter to observe and count the generated aerosol particles. Measurements of particle number concentrations with the GRM were recorded every 6 seconds and the nebuliser was let aerosolise the suspension for 13 minutes. During this period the production of aerosol particles was observed to be approximately constant. A picture of the experimental setup is shown by Figure 4.11.

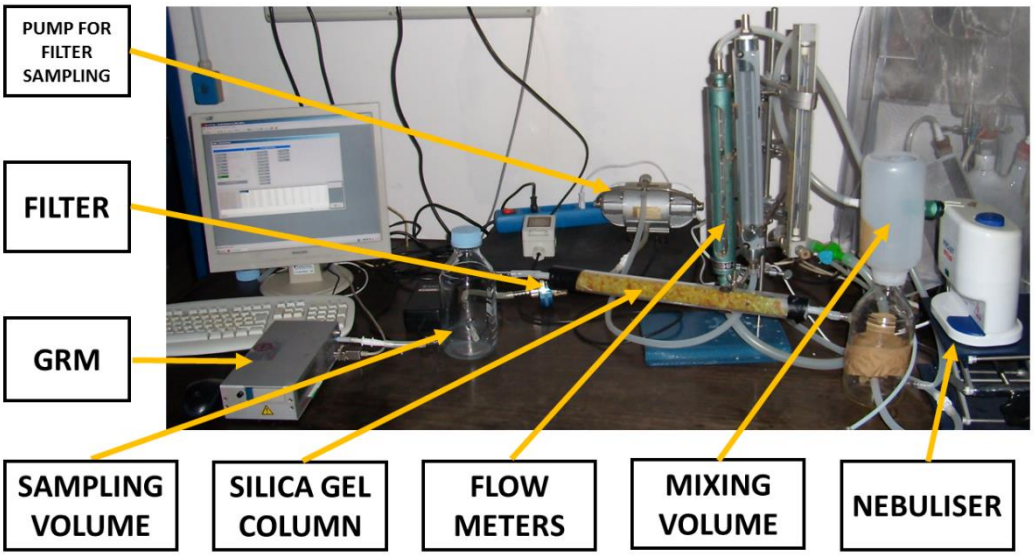

Figure 4.11: Experimental setup.

At the end of the aerosol generation process, the filter (Nuclepore, porosity of 0.22 μm) was removed from its holder and with a cutting tool three small disks were obtained. The three pieces of the filter, previously coated with gold as described in Chapter 3.4.1, were analysed by means of the SEM. By using a magnification of 6000, the PSL particles could be clearly distinguished. Fig 4.12 shows an example of PSL particles deposited onto the filter. Considering Equation 3.2, twenty fields per piece were observed, which yields total number of observed fields (**M**) of 60, and particles were counted. Table 4.5 shows the particle counted in all of the analysed fields of the three stubs observed at the SEM.

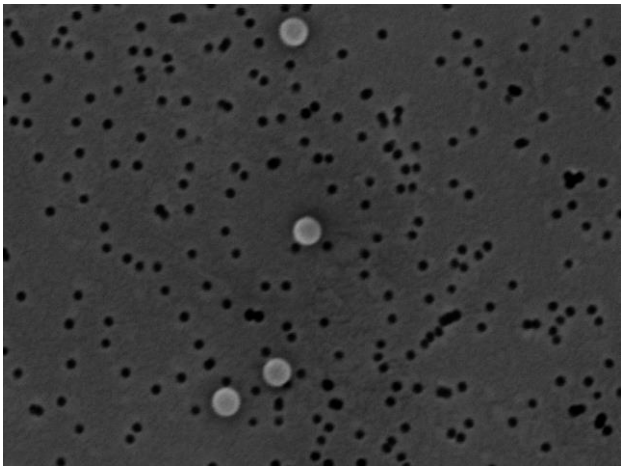

Figure 4.12: Image of a filter sample. White circles are PSL spheres, while the black dots are the filter's pores as viewed at the SEM

Field	Stub 1	Stub 2	Stub 3
	Particle amount	Particle amount	Particle amount
1	7	7	4
2	7	5	7
3	11	4	8
4	2	3	3
5	2	3	4
6	4	1	5
7	4	6	3
8	4	11	7
9	2	1	3
10	8	0	7
11	4	3	8
12	5	8	3
13	7	9	5
14	5	2	7
15	8	5	7
16	6	7	4
17	5	7	9
18	7	3	3
19	2	6	9
20	7	3	6
Total	107	94	112

Table 4.5: Particle counts in each observed field of the three filter's samples.

The total number of particles counted on all fields (**n**) was 313. By considering a total sampling time **t** of 13 min and an inlet sample flow **Q** of 6.5 L min^{-1}, from Equation 3.2 an average particle number concentration ($\mathbf{C_f}$) of $9.0*10^4$ # L^{-1} was obtained.

Figure 4.13 shows the size distribution in four different channels as recorded by the GRM during the test. For the second channel of the GRM (0.4-0.5 μm size range) a particle number concentration below $12*10^4$ # L^{-1} was found, comparable with the concentration obtained from SEM observation.

It is thought that to estimate the number of particles deposited onto the filter the particle deposition should be assumed to be uniform all over the filter. In addition, the comparison was carried out between two results achieved through completely different measurement techniques.

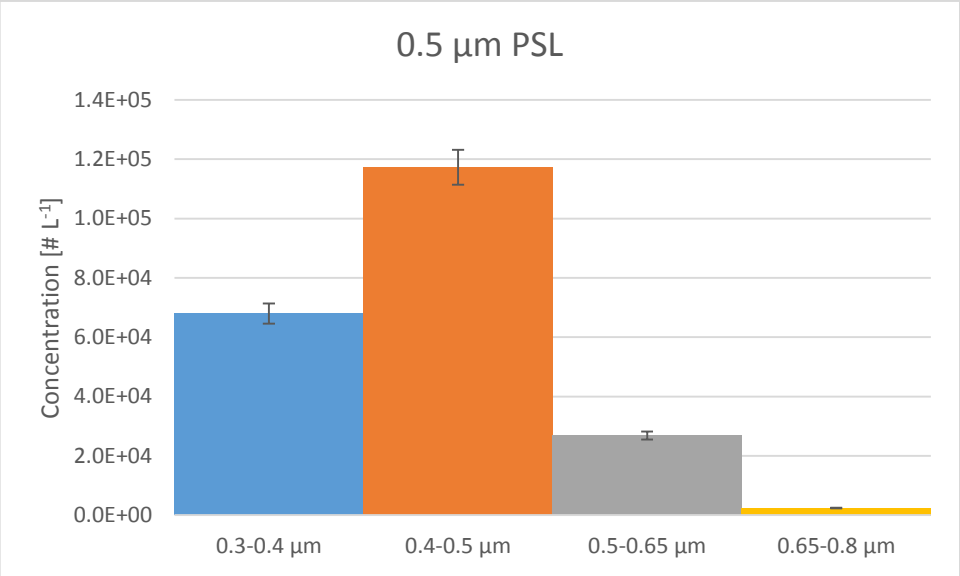

Figure 4.13: PSL particle size distribution as read out from the GRM in different channels.

After this preliminary test, all OPCs and the filter were connected to the sampling volume and a new experiment of PSL generation was carried out. The aerosol was nebulised by means of the Projet nebuliser and the sampling by the OPCs and the particle counting at the SEM were performed in the same way as previously done with the GRM only.

In this case, in order to increase the counting statistics, six pieces of the filter were taken and 12 fields of each sample were analysed by means of the SEM. Aggregates observed on the filter due to water droplets containing more than one PSL particles were not considered in the particle counts (see Figure 4.14). This is because due to the atomisation process some water droplets may contain more than one PSL particle. To calculate the mean particle number concentration and the uncertainty from the number of particles deposited onto the viewed fields Equation 3.2 and Equation 3.3 were used by considering a number of observed fields (**M**) of 72, a total amount of counted particles (**n**) of 474 and a conversion factor **z** of 6200. The number concentration obtained with the filter ($\mathbf{C_f}$) was $1.0*10^5$ # L^{-1}.

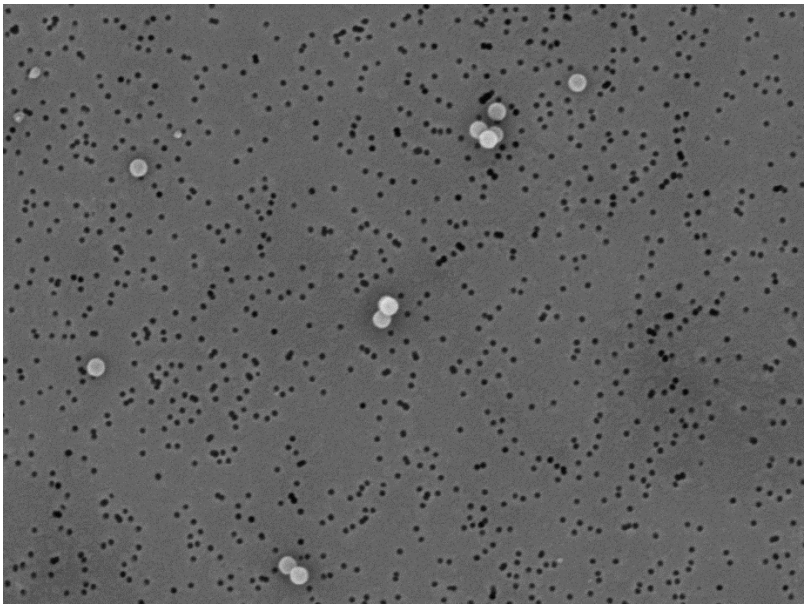

Figure 4.14: Image of a filter sample. The small black dots are the pores of the filter, while the white circles are the PSL spheres as viewed at the SEM. The presence of particle aggregates can be clearly observed.

The particle size distribution relating to this test for the GRM and COPC are shown in Figure 4.15 and 4.16 respectively. Most of the particles are counted in the 0.4-0.5 µm size bin. The particle number concentrations recorded by the COPC ($\mathbf{C_{COPC}}$) and the GRM ($\mathbf{C_{GRM}}$) were then compared with the one obtained from the filter data (see Table 4.6). The uncertainties on each mean particle number concentration were evaluated by considering both the square root of the counts and the error on the sampling flow rate, as already described in Chapter 3.4.3.

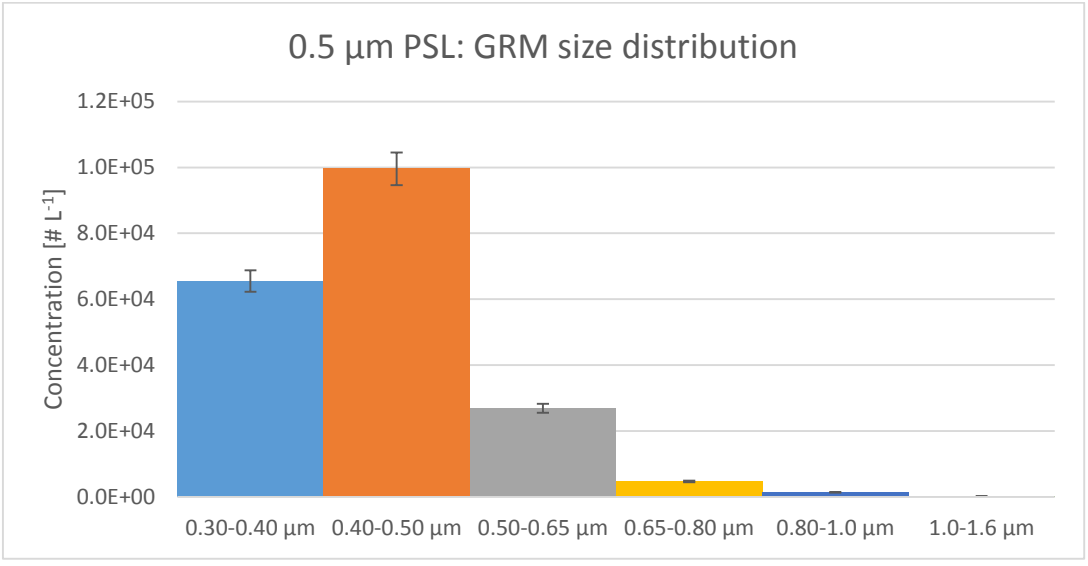

Figure 4.15: Averaged particle size distribution reported by the GRM during the generation of 0.5 µm PSL spheres. The peak observed in the 0.4-0.5 µm size bin was considered for the comparison with monodisperse aerosol.

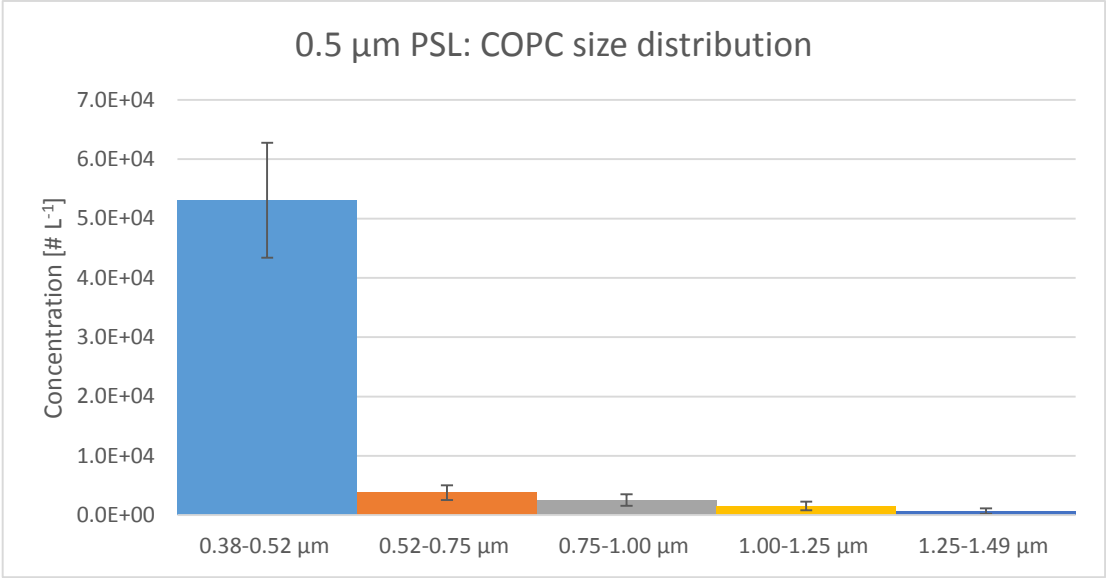

Figure 4.16: Averaged particle size distribution reported by the COPC during the generation of 0.5 µm PSL spheres.

	Size range [µm]	**Number concentration [# L^{-1}]**
C_{COPC}	0.38-0.52	$(5.3 \pm 1.0)*10^4$
	0.52-5	$(0.9 \pm 0.2)*10^4$
C_{GRM}	0.4-0.5	$(10.0 \pm 0.5)*10^4$
	0.5-5	$(3.4 \pm 0.2)*10^4$
C_{LPS}	0.5-5	$(3.7 \pm 0.2)*10^4$
C_f		$(10.2 \pm 1.0)*10^4$

Table 4.6: Particle number concentrations measured by each OPC and obtained by counting the particles deposited onto the filter.

The particle number concentrations reported by each instrument in different size ranges and the one obtained from the filter's sampling are summarised in Table 4.6, while ratios of the PSL number concentrations obtained from each instrument are shown in Table 4.7.

Ratio	**Size range: 0.4-0.5 µm**	**Size range: 0.5-5 µm**
COPC/GRM	0.46	0.34
LPS/GRM		1.11
COPC/LPS		0.30

Table 4.7: COPC/GRM, LPS/GRM and COPC/LPS ratios for the 0.4-0.5 µm and 0.5-5 µm size ranges during the nebulisation of PSL spheres of 0.5 µm in diameter.

In the 0.4-0.5 µm size range the PSL number concentration reported by the GRM is well compared with the one obtained by counting particles at the SEM (**C_f**). In the 0.5-5 µm size range, in which aggregates of two or more PSL particles may be found, the particle number concentration reported by the LPS is greater than the one reported by the GRM, but the LPS/GRM ratio is smaller than previously found. This is because the aerosol concentration is fairly greater than the concentration limit the LPS can sample (35300 #

L^{-1}), which boils down to coincidence errors. Moreover, the GRM counts most of the PSL concentration in the 0.4-0.5 µm size range, which the LPS does not sample.

In the first channel (0.38-0.52 µm) the COPC counted $5.3*10^4$ # L^{-1}; the COPC/GRM ratio in the 0.4-0.5 µm size range is found to be 0.48, while in the 0.5-5 µm size range this ratio drops down to 0.34. In both cases the values are comparable with the ones found during indoor samplings (*Tests 2,3,5* and *6* in Figure 4.8).

Two more tests with 0.5 µm PSL spheres were carried out, during which the COPC was not equipped with the pump. Figure 4.17 shows the COPC/GRM ratio for the 0.4-0.5 µm size range as a function of the concentrations read out from the GRM in the same size range. It may be observed that without the pump the COPC is unable to sample from a pipe.

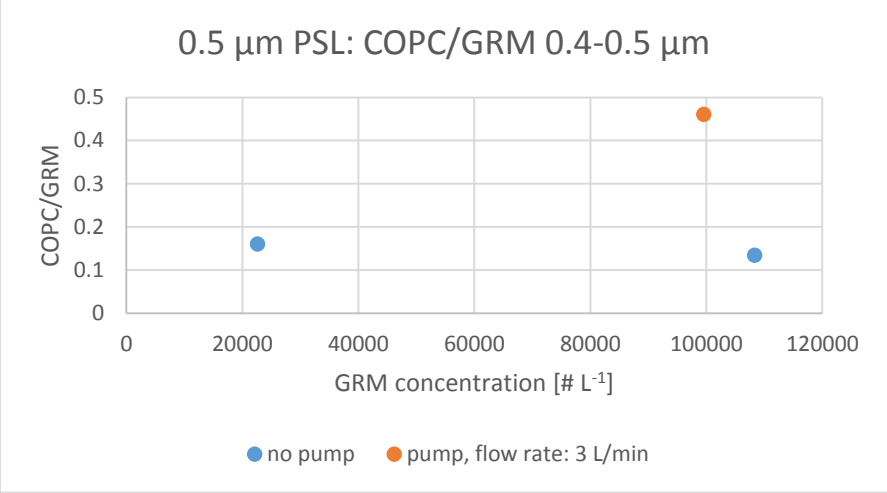

Figure 4.17: Plot of the COPC/GRM ratio in the 0.4-0.5 um size range as a function of the PSL number concentration measured by the GRM in the same range during tests with 0.5 µm PSL. The red dot ("pump, flow rate: 3 L/min") refers to the test carried out in parallel with the filter's sampling. Blue dots ("no pump") refer to tests performed with the COPC not equipped with the pump.

4.3.3 Test with 0.95 µm PSL

A suspension of PSL of size d = 0.95 µm was prepared. The OPCs and the filter were connected to the sampling volume. After the Projet nebuliser was turned on, the OPCs were let sample, while particles were sampled by a pump and deposited onto the filter. A sample of these particle is provided by Figure 4.18.

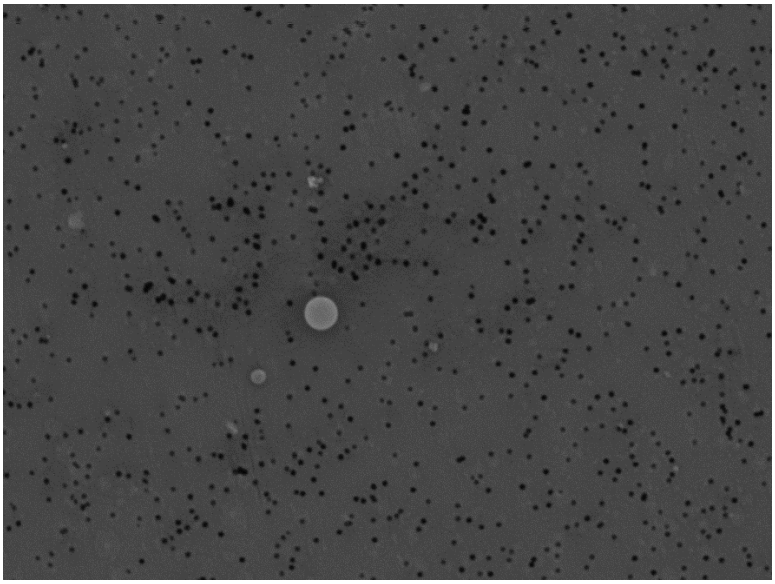

Figure 4.18: Sample of a stub: a PSL particle of 0.95 µm in size; the small white objects around the particle are residuals and debris from surfactant present in the PSL suspension.

Considering Equation 3.2 and Equation 3.3, by using a magnification of 3000, i.e. a conversion factor (**z**) of 3030, with a total amount of counted particles (**n**) of 636, a number of observed fields (**M**) of 186, a number concentration ($\mathbf{C}_f$) of $8.3*10^3$ # L^{-1} was found.

With this PSL size, a critical aspect in monodisperse particle atomisation may be observed. The nebulisation of PSL particles also results in many water droplets containing no PSL spheres, but only residuals of small size and debris from the surfactant used to avoid PSL particle agglomeration in the suspension; these small impurities are clearly visible in Figure 4.18. As an example, the aerosol size distribution from the GRM is shown in Figure 4.19: the highest concentrations appear to be in the lowest channels (0.3-0.65 µm), while concentrations in channels in which the signal from the PSL particles is expected are significantly lower. In performing these tests, only the correct channel bins should be considered, which is also the procedure used for OPC calibration (ISO 21501-4, 2007).

Particle number concentration obtained from each instrument and the filter are reported in Table 4.8.

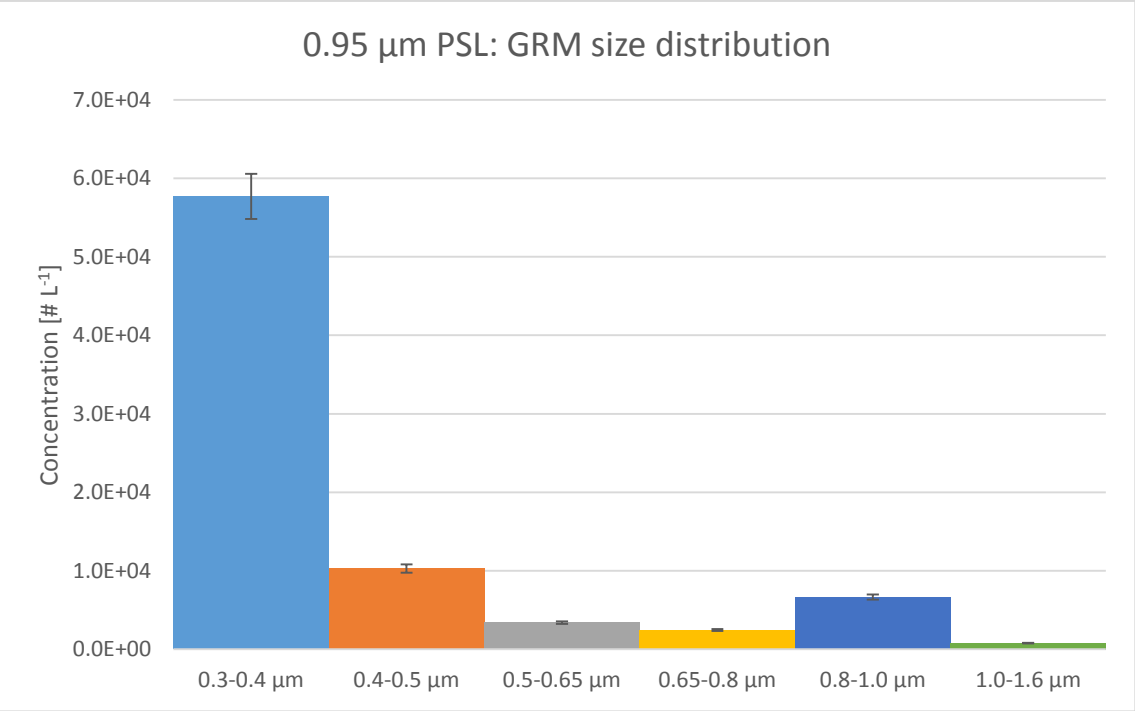

Figure 4.19: 0.95 µm PSL size distribution as read out from the GRM. Numerous counts are observed in the first channels and are due to the non-complete evaporation of droplets containing water or surfactant only.

	Size range [µm]	**Number concentration [# L^{-1}]**
C_{COPC}	0.75-1	$(4.0 \pm 1.3)*10^3$
	0.52-5	$(10.1 \pm 2.4)*10^3$
C_{GRM}	0.8-1	$(6.7 \pm 0.3)*10^3$
	0.5-5	$(13.7 \pm 0.7)*10^3$
C_{LPS}	0.5-5	$(28.1 \pm 1.6)*10^3$
C_f		$(8.4 \pm 0.9)*10^3$

Table 4.8: Comparing the PSL number concentration evaluated from filter data (C_f) with the ones read out from each OPC.

By looking at the size bins where the generated aerosol particles are expected, both the COPC and the GRM show the maximum particle number concentration in the correct channel (0.75-1 µm for the COPC, 0.8-1 µm for the GRM), as pointed out by Figure 4.20 and 4.21.

In the 0.8-1 µm size range the GRM reports a PSL number concentration comparable with the one obtained from the filter: $6.7*10^3$ # L^{-1}. In the same size interval (0.75-1 µm) the COPC reports a PSL concentration of $4.0*10^3$ # L^{-1}, which is still smaller than the one read out from the GRM, but the normalised COPC/GRM ratio in this size range is 0.46,

which is greater than the one found with PSL particles of smaller sizes; this implies that the COPC's counting efficiency probably increases with increasing particle size. In the 0.5-5 µm size range, the LPS reports a particle number concentration almost twice the one read out from the GRM in the same interval; this confirms that this OPC overestimates the particle number concentration.

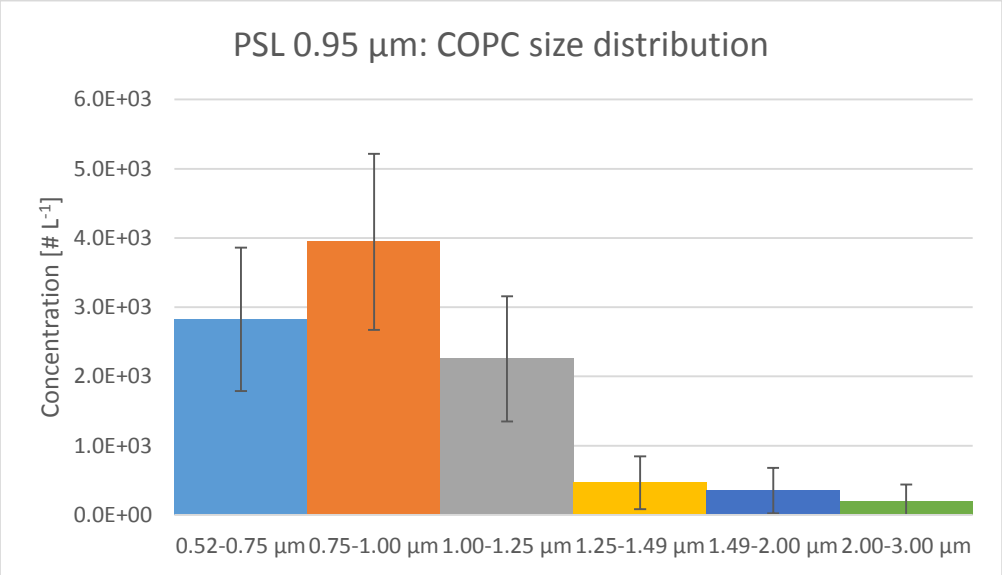

Figure 4.20: Averaged particle size distribution reported by the COPC during the generation of 0.95 µm PSL spheres. The peak is observed in the 0.75-1.00 µm size bin.

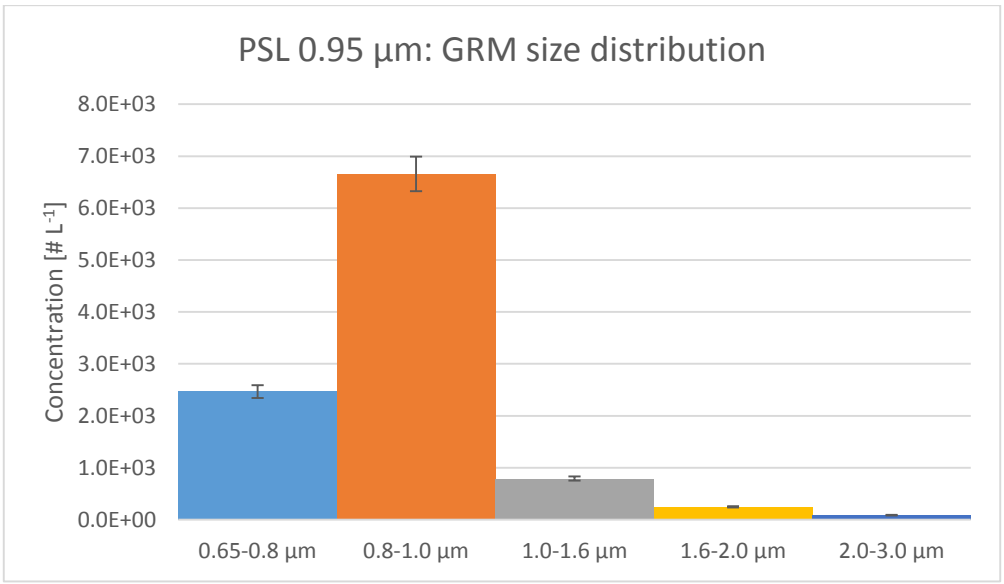

Figure 4.21: Averaged particle size distribution reported by the GRM during the generation of 0.95 µm PSL spheres. The peak is observed in the 0.8-1.0 µm size bin.

Figures 4.22 and 4.23 report the normalised particle number concentrations in the channels from 0.4 to 2 µm as functions of the particle size for the COPC and the GRM for these two tests. In both cases at sizes smaller than 1 µm the COPC underestimates the GRM counts, while at greater sizes the opposite is true. Furthermore, it may also be observed that the GRM has a better resolution than the COPC for particles of 1 µm in size.

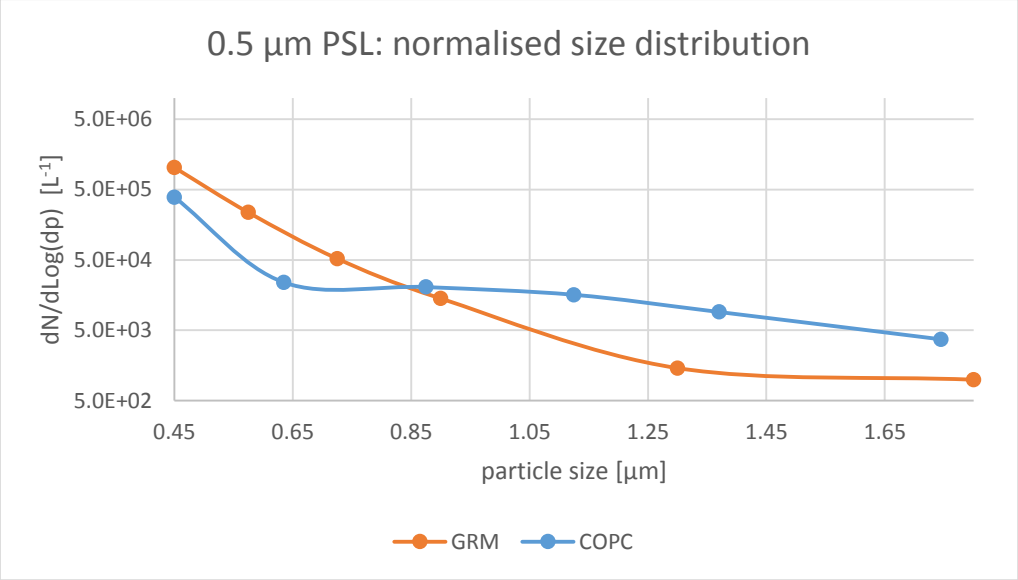

Figure 4.22: Plot of the normalised particle number concentrations reported by the COPC and the GRM as read out from each channel against the corresponding particle size during the test with 0.5 µm PSL spheres conducted with the Projet nebuliser.

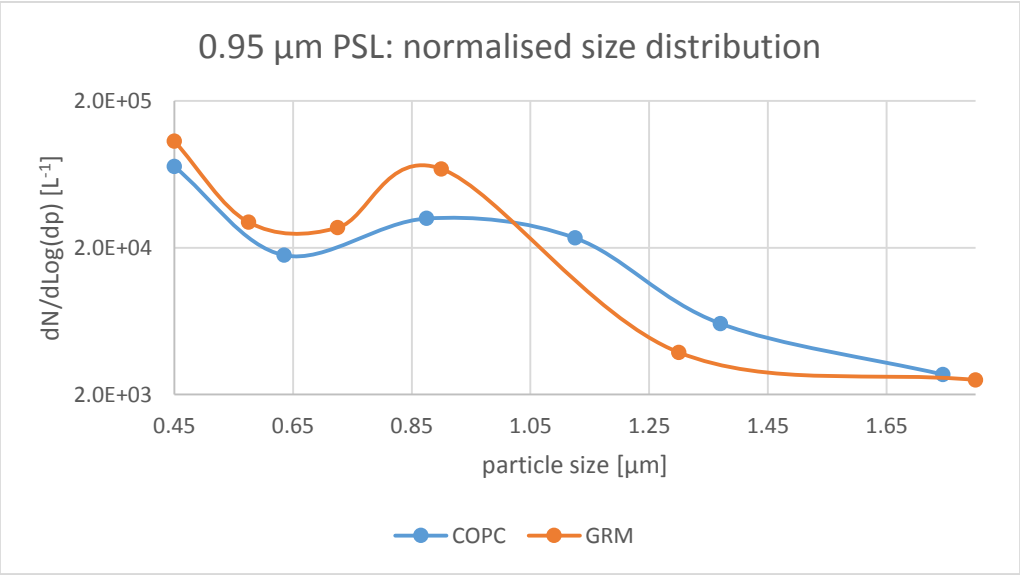

Figure 4.23: Plot of the particle normalised number concentrations reported by the COPC and the GRM as read out from each channel against the corresponding particle size during the test with 0.95 µm PSL spheres conducted with the Projet nebuliser.

4.3.4 Generating PSL with the AGK 2000 aerosol generator

To make the generation of the aerosol particles more controlled, the commercial generator AGK 2000 was purchased and used in the following runs. This generator was used to calibrate the LPS as shown in the next chapter. To improve the entrance flow rate of the COPC, this OPC was no longer located in the sealed box; instead, it was directly connected to a pump with a flow rate at the fan's outlet equal to the manufactured one (0.2 L min^{-1}). Moreover, as this instrument is not perfectly sealed, to avoid contamination by indoor particles, it was covered and sealed by a plastic bag, as shown by Figure 4.24. The pump's flow rate was checked, before each test, by means of a flow meter positioned at the entrance of the sampler.

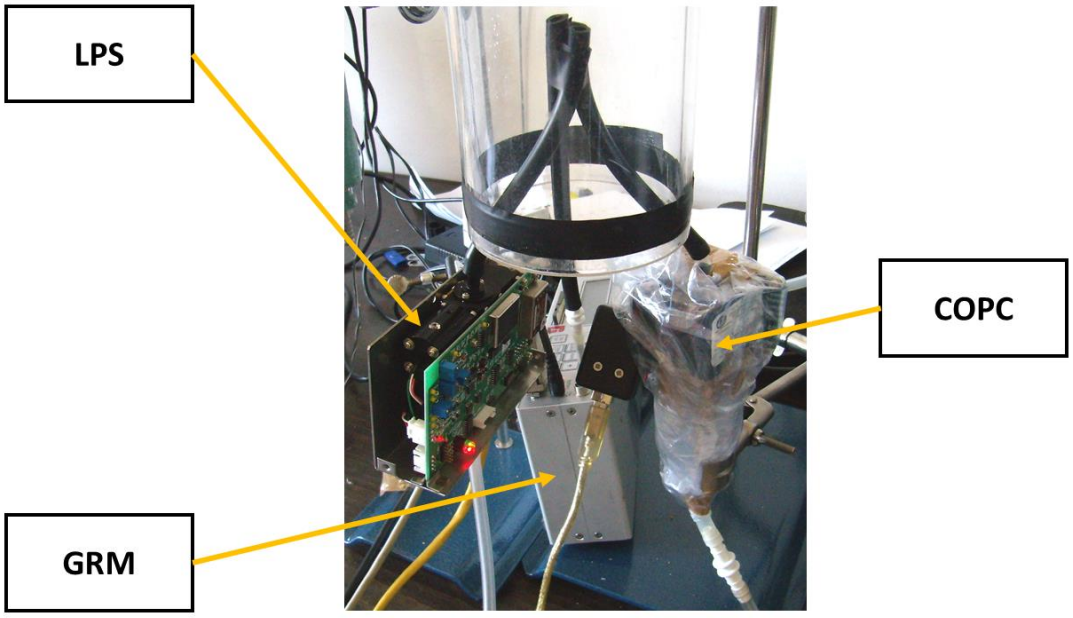

Figure 4.24: LPS, COPC and GRM during the sampling; as it may be observed, the COPC was sealed in a plastic bag.

Tests with 0.5 μm PSL spheres were carried out with the AGK 2000 aerosol generator. In all cases the size distribution appeared to be monodisperse and once again, by looking at the GRM's output, a clear peak was found in the range 0.4-0.5 μm. Figures 4.25 and 4.26 show the particle size distribution obtained with the new generator at a working pressure of 2.0 bar.

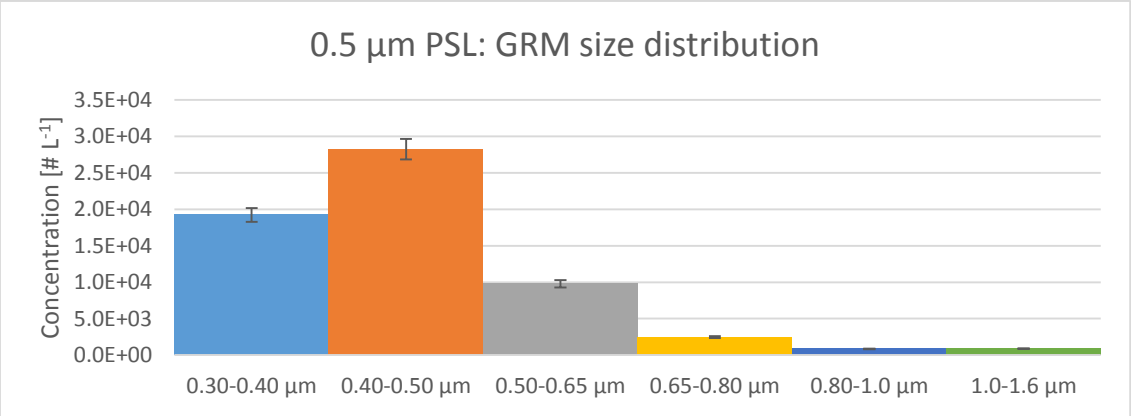

Figure 4.25: 0.5 µm PSL particle size distribution as reported by the GRM; generator working pressure: 2.0 bar.

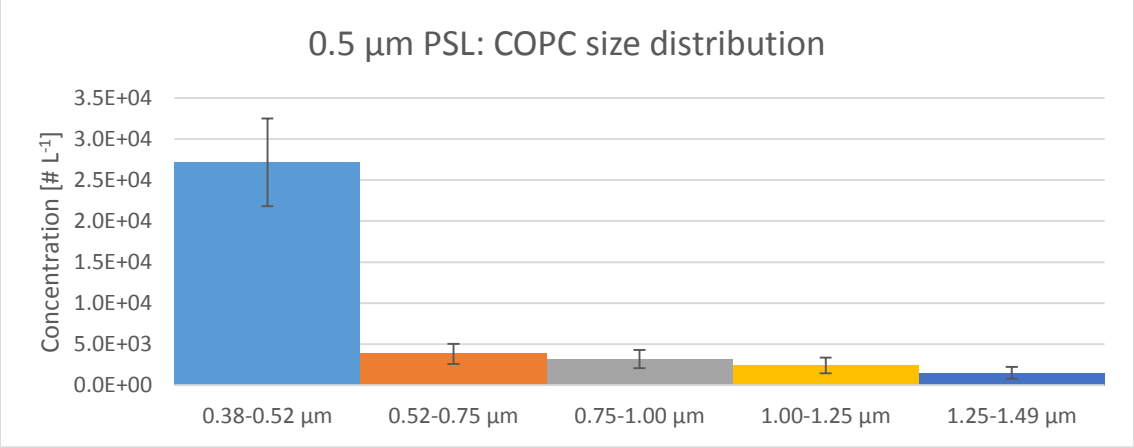

Figure 4.26: 0.5 µm PSL particle size distribution as reported by the COPC; generator working pressure: 2.0 bar.

Results show that in tests with particle number concentrations smaller than the LPS's concentration limit value, the LPS/GRM ratio is roughly 1.30, which once again indicates an overestimate in the counts. On the other hands, the COPC/GRM ratio in the 0.4-0.5 µm size range with 0.5 µm PSL particles is between 0.67 and 0.69 depending on the nebuliser's working pressure. This value is greater than the one previously found; this could be due to a lesser amount of non-evaporated droplets with the new generation system or a better sampling flow rate for the COPC. The improvement of the COPC's performance compared with previous tests is given by Figure 4.27, which shows a plot of the COPC/GRM ratio in the 0.4-0.5 µm size range as a function of the GRM output in the same size interval in all tests conducted with PSL spheres of 0.5 µm in diameter. Here, the red dots ("New configuration") refer to the tests carried out with the new generator and the COPC connected to the pump; the blue dots ("Old configuration") refer to the tests carried out with the previous generator (Projet) with the COPC equipped with the

pump drawing air at a flow rate of 3 L min^{-1} and the one where the COPC was not supported by the pump.

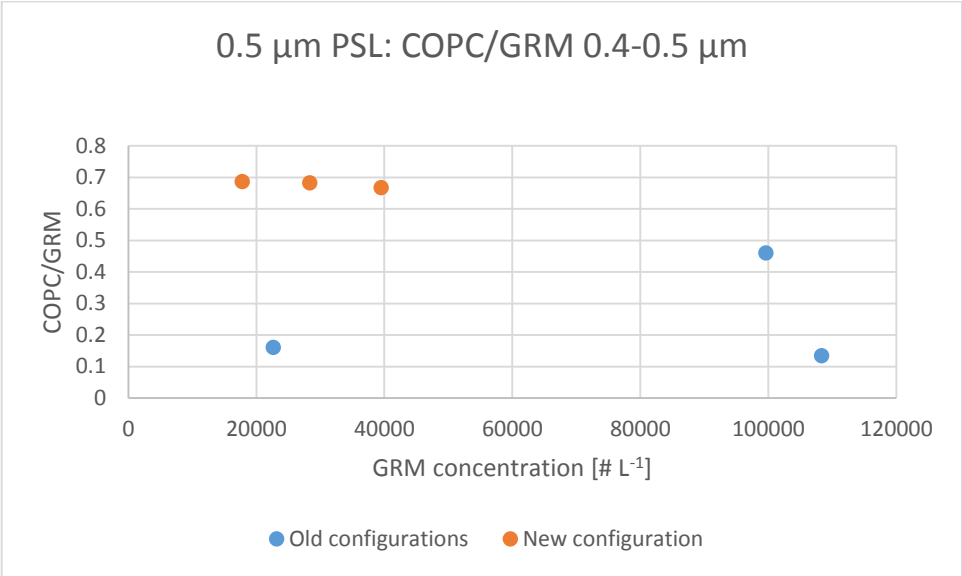

Figure 4.27: Plot of the COPC/GRM ratio in the 0.4-0.5 µm size range as a function of the PSL number concentration measured by the GRM in the same range during tests with 0.5 µm PSL. Blue dots ("Old configurations") represent the test with the COPC equipped with the pump drawing air (flow rate: 3 L min^{-1}) and the ones where it was not supported by the pump. Red dots ("New configuration") represent the tests with 0.5 µm PSL with the new setup.

The AGK 2000 generator was also used in tests with 1.03 µm PSL spheres (working pressure: 2.8 bar). Also in this case the distribution was found to be monodisperse, as shown by Figure 4.28 and 4.29, which represent the PSL size distribution reported by the COPC and the GRM respectively. It should be noticed that in these tests PSL of 1.03 µm in size was used, unlike in previous tests, where PSL of 0.95 µm in size was used.

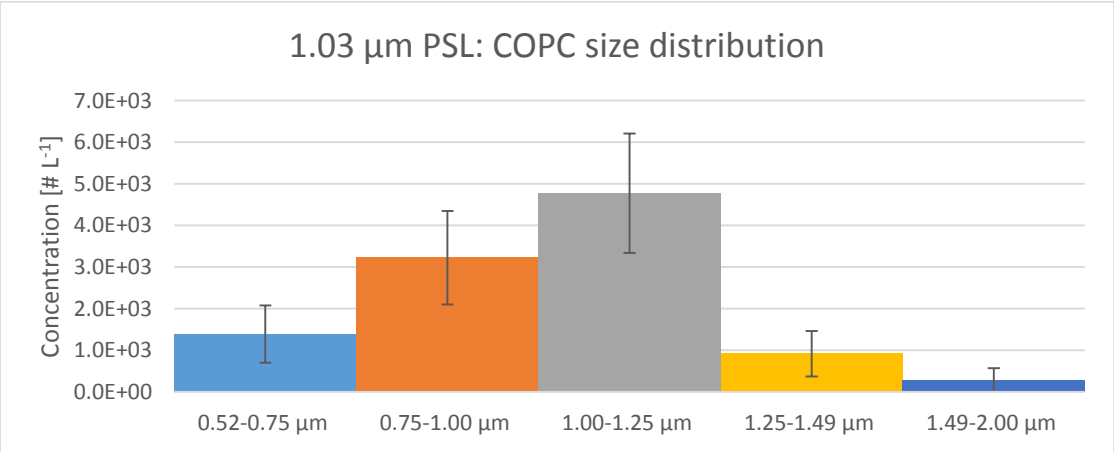

Figure 4.28: 1.03 µm PSL particle size distribution as reported by the COPC; generator working pressure: 2.8 bar.

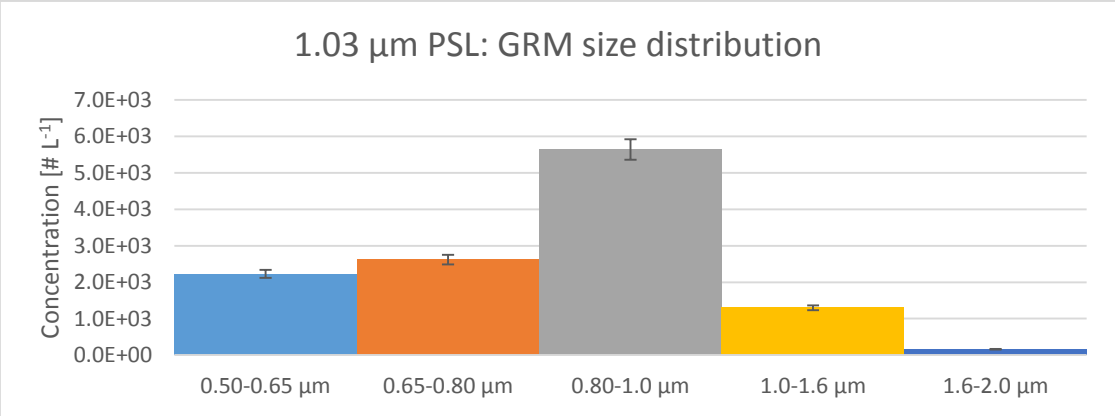

Figure 4.29: 1.03 µm PSL particle size distribution as reported by the GRM; generator working pressure: 2.8 bar.

The COPC reports a clear peak in the channel where the PSL signal is expected (1-1.25 µm): in this bin a particle number concentration of $4.8*10^3$ # L^{-1} is observed. Instead, the GRM shows a peak in the 0.8-1 µm bin and reporting a value of $5.6*10^3$ # L^{-1}, while in the channel where most of the particles are expected (1-1.6 µm) a particle concentration of $1.3*10^3$ # L^{-1} is observed. Once again, the COPC appears to underestimate the concentrations read out from the GRM for sizes smaller than 1 µm, while it overestimates the GRM concentrations for sizes greater than 1 µm. Results are reported in Table 4.9; for the sake of completeness, the total number concentrations read out from the COPC and the GRM in the 0.5-5 µm size range are also reported, as well as the concentrations read out from the LPS. In particular, once again the latter appears to overestimate the GRM concentrations in the 0.5-5 µm size range.

Instrument	**Size range [µm]**	**Number concentration [# L^{-1}]**
COPC	0.75-1	$(3.2 \pm 1.1)*10^3$
	1-1.25	$(4.8 \pm 1.4) *10^3$
	0.52-5	$(13.7 \pm 3.1) *10^3$
GRM	0.8-1	$(5.6 \pm 0.3) *10^3$
	1-1.6	$(1.3 \pm 0.1) *10^3$
	0.5-5	$(12.0 \pm 0.6) *10^3$
LPS	0.5-5	$(13.8 \pm 0.9) *10^3$

Table 4.9: Particle number concentrations reported by each instrument in several size ranges during the test with 1.03 µm PSL spheres conducted with the AGK 2000 generator.

Figure 4.30 and 4.31 show the normalised size distributions as read out from the COPC and the GRM for the tests with 0.5 µm (working pressure: 2.0 bar) and 1.03 µm PSL

conducted with the AGK 2000 generator. These figures confirm the previous findings, i.e. the COPC underestimates the GRM particle number concentrations at sizes smaller than 1 µm, while it overestimates them at sizes greater than 1 µm. It is also noticed that the GRM classifies particles of 1.03 µm in sizes in the 0.8-1 µm channel and the peak relating to these particles is fairly less sharp than with 0.95 µm particles.

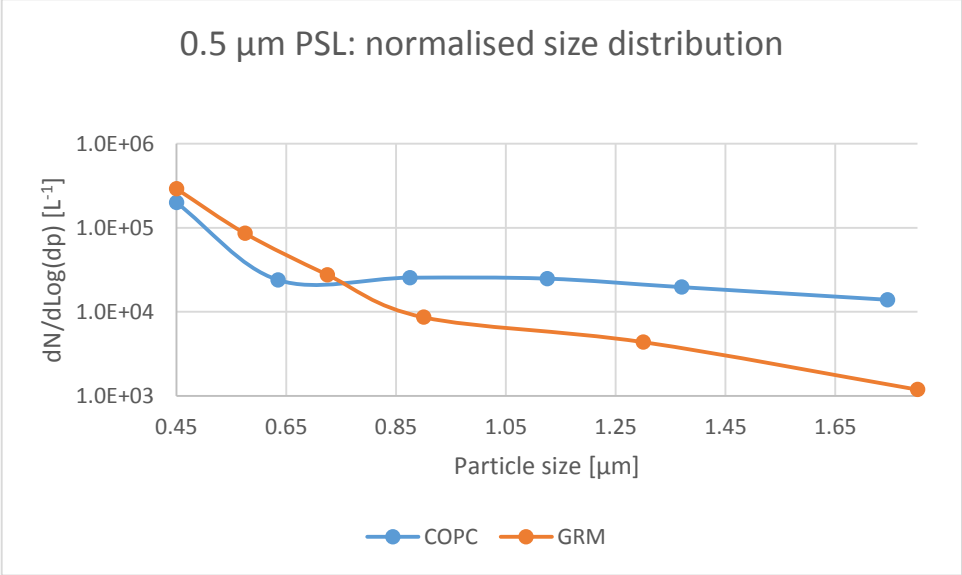

Figure 4.30: Plot of the normalised particle number concentrations reported by the COPC and the GRM as read out from each channel against the corresponding particle size during the test with 0.5 µm PSL spheres conducted with the AGK 2000 nebuliser.

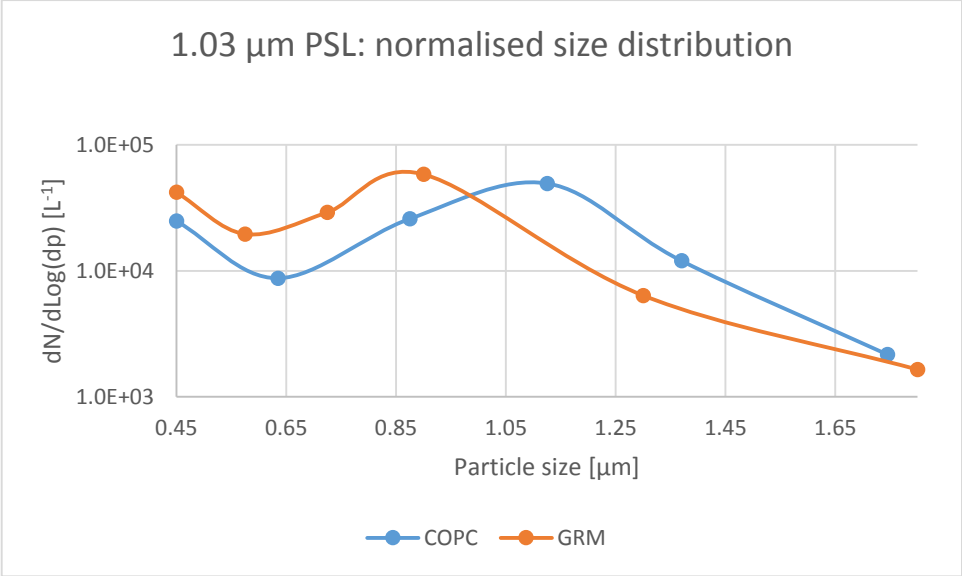

Figure 4.31: Plot of the normalised particle number concentrations reported by the COPC and the GRM as read out from each channel against the corresponding particle size during the test with 1.03 µm PSL spheres conducted with the AGK 2000 nebuliser.

4.4 Simulation of an indoor campaign

To verify the main conclusions obtained with the previous tests, two indoor campaigns, i.e. samplings of indoor particle concentration, were undertaken. In these campaigns (Test A and Test B), the COPC and the GRM were let sample laboratory indoor air for about 20 hr with the inlets facing upwards.

During the Test A the COPC was let free to sample with no further support, while in Test B the COPC was inserted and sealed in a polyethylene envelope and equipped with a pump drawing air at a rate of 0.2 L min^{-1} as already done with the AGK 2000 generator. In this way it was made sure that the COPC should be sampling at its correct entrance flow rate in every instant.

Data were recorded every minute and the results obtained by each OPC were compared with each others. From the time-series achieved by each OPC a linear cross-correlation was carried out and the corresponding Pearson product-moment correlation coefficient (R^2) was evaluated. This operation was performed for both the 0.4-5 μm and the 1-5 μm size interval and the ratio COPC/GRM was calculated for each single measurement for both size ranges.

As for Test A, particle number concentrations returned by the GRM until midnight were generally low, as shown by Figure 4.32. This was likely due to the limited use and the scarce presence of personnel in the laboratory during this period. However, two peaks appear around midnight and at 4 a.m. and a third greater one is observed around 9 a.m. The former is likely due to the deposition of particles suspended during the day before, the 4 a.m. peak might be due to the air conditioning system, while the 9 a.m. peak was caused by an outdoor air outbreak due to the opening of a window.

The COPC presents the same trend as the GRM, although the recorded particle number concentrations are lower. This is consistent with the results previously obtained. Also the peak relating to the window's opening is much less evident.

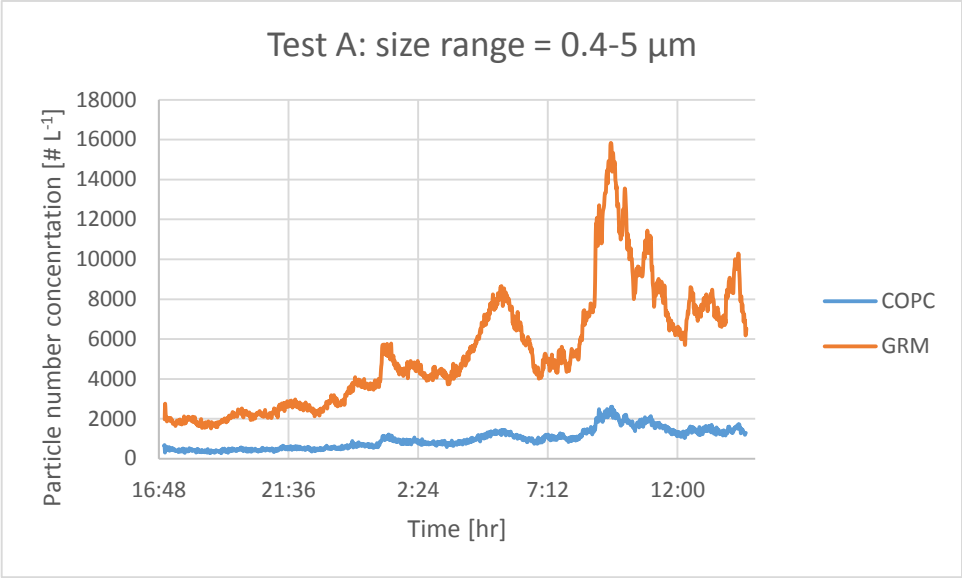

Figure 4.32: Time-series of the particle number concentrations in the 0.4-5 um size range during Test A.

Figure 4.33 reports the cross-correlation between the concentrations read out from the GRM and the ones read out from the COPC in the 0.4-5 µm size range. Data recorded by the two devices appear to be linearly correlated (R^2 = 0.93). The same figure also shows the average normalised ratio of the concentrations reported by the COPC to the ones reported by the GRM (**y**), which is 0.18. Also it may be observed that data are more concentrated when concentrations are low, while at high concentrations (more than 10000 # L^{-1} as recorded by the GRM) data are more scattered.

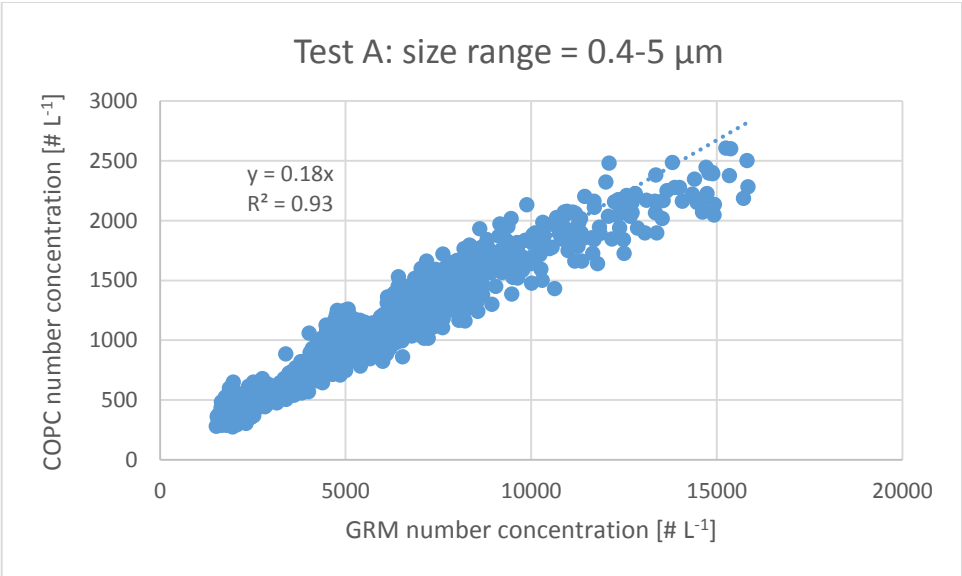

Figure 4.33: Scatterplot of the GRM output against the COPC output for the 0.4-5 µm size range during Test A.

As for Test B, the indoor particle number concentrations appear to be even lower (Figure 4.34): a peak comes out around 9 PM and thereafter the concentrations decrease up to the morning of the day after, where a slight increase is observed and a peak is observed in correspondence of a window's opening around 10:30 AM. From this figure, it may be observed that the COPC's performances clearly improve if this OPC is equipped with a pump. Figure 4.35 reports the average normalised ratio of the concentrations recorded by the COPC to the ones recorded by the GRM (**y**) in the 0.4-5 µm size range, which in this case is 0.66, comparable with the ratios obtained during tests with PSL particles (see Figure 4.27). The same figure also shows that data from the two OPCs are well linearly correlated (R^2 = 0.97: even higher with respect to the previous R^2 value obtained with the COPC not equipped with the pump) and, once again, at high concentrations (more than 6000 # L^{-1} as read out from the GRM) data are more scattered.

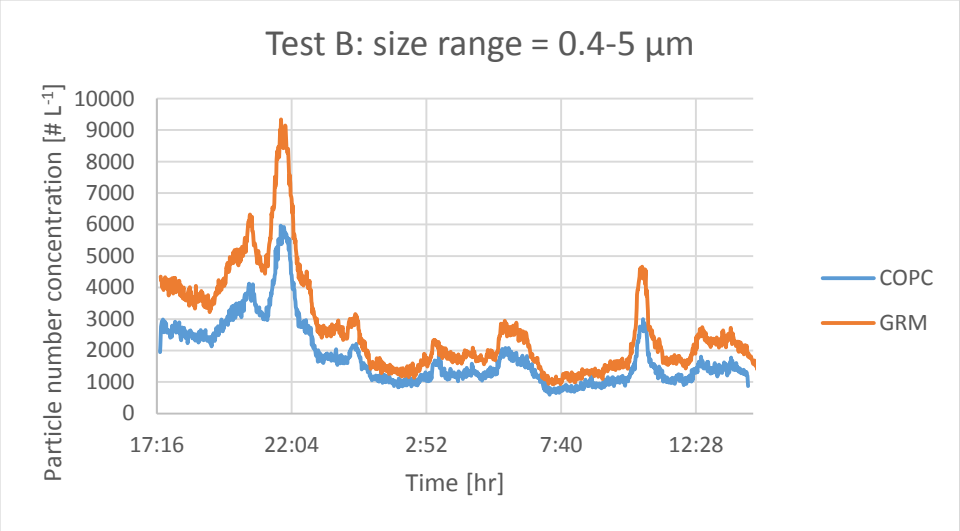

Figure 4.34: Time-series of the particle number concentrations in the 0.4-5 um size range during Test B.

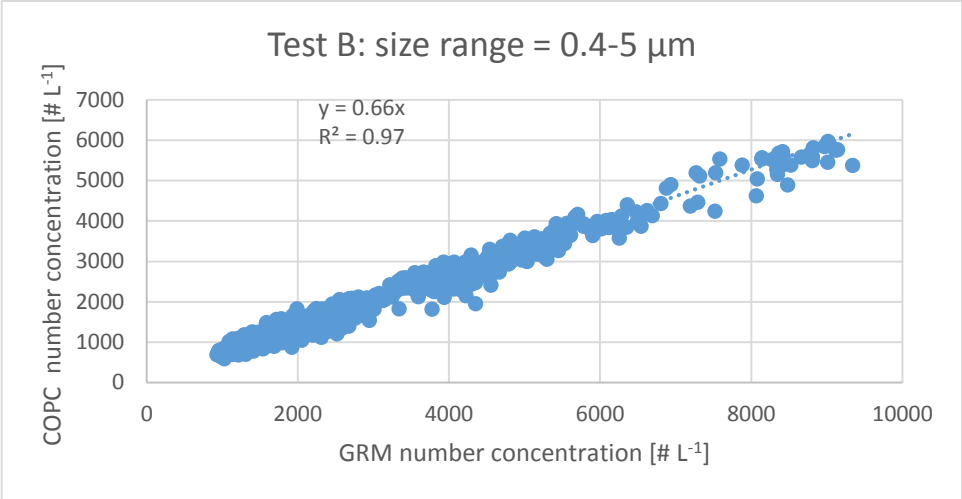

Figure 4.35: Scatterplot of the GRM output against the COPC output for the 0.4-5 um size range during Test B.

These findings show that the concentrations measured by the COPC are linearly correlated with the ones returned by a calibrated instrument such as the GRM and confirm the hypothesis that the COPC requires the support of a pump to sample at its nominal flow rate (0.2 L min^{-1}). In future, this may allow for measurements of indoor air carried out by the COPC after the application of an appropriate linear correction factor.

As for the 1-5 µm size range, it may be noticed that the COPC/GRM ratio is fairly greater than in the 0.4-5 µm size range; however, while in Test A (Figure 4.36) the GRM still measures more than the COPC (COPC/GRM = 0.79), in Test B (Figure 4.37) the COPC measured concentrations greater than the GRM (COPC/GRM = 2.11). It was initially thought that the drawing rate of the COPC was too small and at big particle sizes overestimation problems might occur if the OPC was sampling with the inlet facing upwards, thus introducing a systematic error due to the different sampling velocities of the two instruments. However, the Agarwall-Liu criterion (Hinds, 1999), which provides the conditions for correct samplings in clean air, was found to be satisfied; indeed, the calculated sampling velocity of this instrument (9 cm s^{-1}) is fairly greater than the settling velocity of such particles (V_{TS} = 3.48*10^{-3} cm s^{-1} for d = 1 µm; V_{TS} = 7.76*10^{-2} cm s^{-1} for d = 5 µm; Hinds, 1999); therefore the oversampling of the COPC in this size range is not the consequence of the inlet orientation (upward or lateral). In any case, in both tests the total contribution of particles in the 1-5 µm size range was always almost negligible (never more than 700 # L^{-1}, to be compared with average total concentrations of 4000 # L^{-1}), however this confirms that at sizes greater than 1 µm the COPC tends to return higher particle number concentrations than the GRM (see Figures 4.22, 4.23, 4.30 and 4.31).

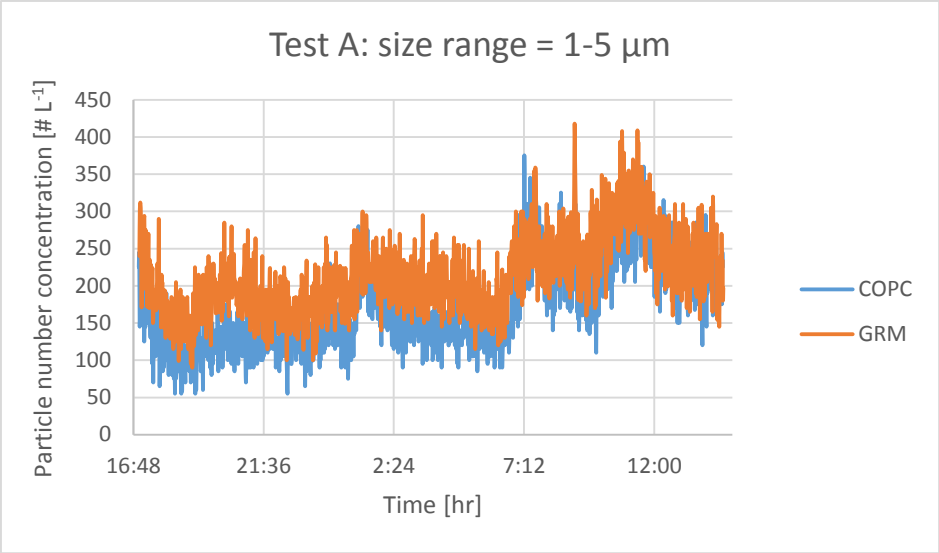

Figure 4.36: Time-series of the particle number concentrations in the 1-5 um size range during Test A.

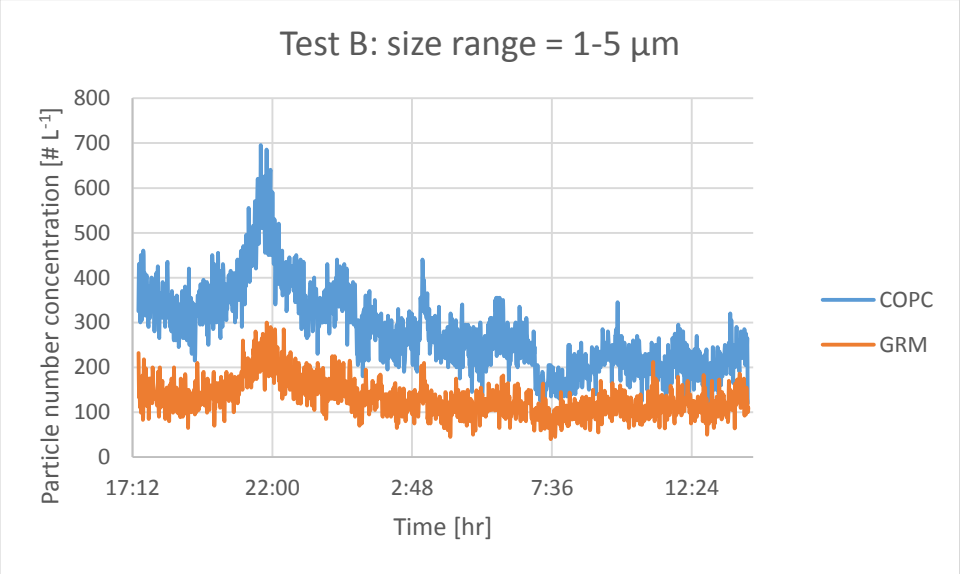

Figure 4.37: Time-series of the particle number concentrations in the 1-5 um size range during Test B.

By looking at the trend of the COPC/GRM ratio against the total particle number concentration (Figure 4.38 and 4.39), it may be observed that at low number concentrations data are more scattered. One possible explanation might be that the COPC measures data every 1 second, while the GRM can return averaged concentrations after at least 6 seconds. For instance, a number concentration of 10000 # L^{-1} may result from the average of three measurements (e.g., 10000, 9200 and 10800 # L^{-1}). At smaller number concentrations the same result implies greater variability in terms of magnitude order inside the single measurements (e.g., 1000 # L^{-1} may result from averaging the

following measurements: 500 # L^{-1}, 1200 # L^{-1}, 1300 # L^{-1}). To this purpose, specific tests should be undertaken.

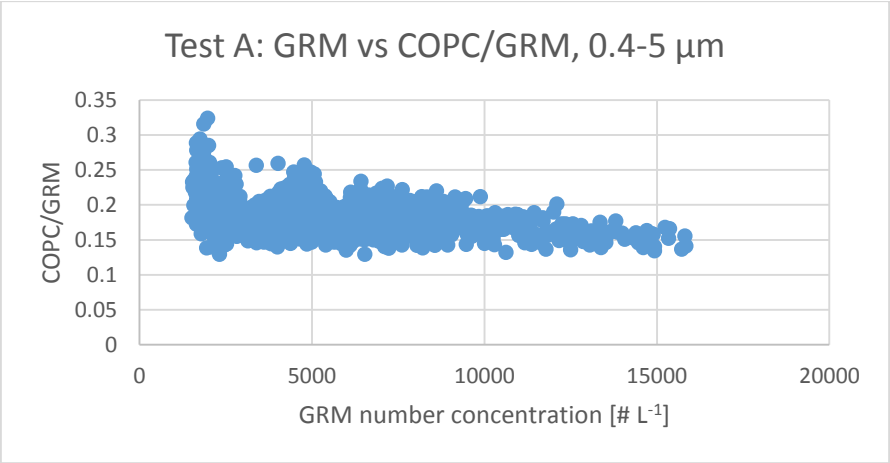

Figure 4.38: Scatterplot of COPC/GRM as a function of the GRM particle number concentration during Test A for the 0.4-5 µm size range.

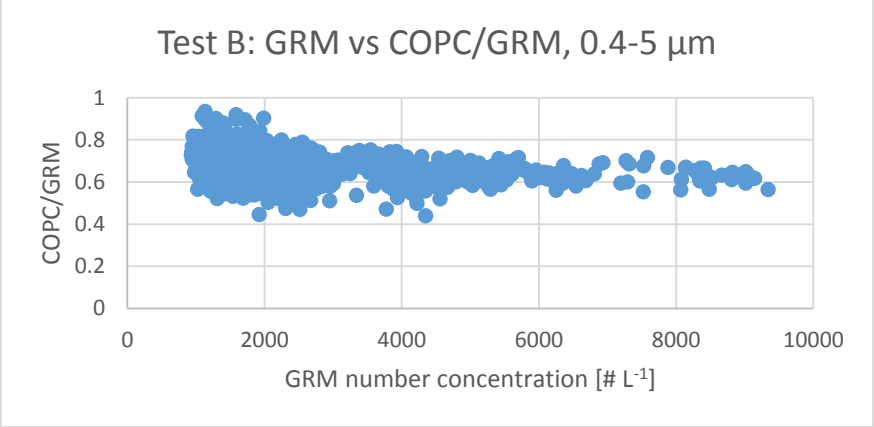

Figure 4.39: Scatterplot of COPC/GRM as a function of the GRM particle number concentration during Test B for the 0.4-5 µm size range.

In conclusion, the COPC appears to underestimate the concentration of particles smaller than 0.5 µm; by equipping the COPC with a pump, at particle number concentrations greater than 3000 # L^{-1} the correct total particle number concentration may be achieved by dividing by 0.66 the normalised values obtained from the COPC (see Figure 4.35). For particle number concentrations smaller than 3000 # L^{-1} this conversion still applies, although with less accuracy. By using the COPC as it comes out from the factory (without the pump), this ratio would drop down to 0.18, making the measurement almost physically meaningless.

4.4 Conclusion

In this chapter the performances and behaviour of the COPC were characterised. This new generation device allows for continuous personal sampling in both indoor and outdoor environment due to its small size, reduced weight and low noise.

Several tests in indoor conditions and with PSL calibrated spheres of different diameters were performed and reported in this chapter. The GRM was taken as the reference device and the results obtained from the COPC and the LPS were compared with the GRM output. In some of the tests with calibrated PSL spheres a parallel filter sampling was carried out. Results show a good agreement between the GRM data and the ones obtained by counting at the SEM particles deposited onto the filter. Indoor tests suggested that in the range 0.5-5 μm the LPS overestimated the total particle number concentrations, while the COPC always underestimated it.

It was concluded that to achieve reliable data from the COPC it is however necessary to equip this OPC with a pump, in order to keep the inlet flow rate constant. Under this configuration experimental results yield a normalised conversion factor of 0.66 for the 0.4-5 μm size range with respect to OPCs of commercial use such as the GRM.

Experimental results also indicate that the COPC can quite well classify particle sizes; this OPC appears to have a greater counting efficiency for particles greater than 1 μm, yet the amount of such particles in indoor environments is negligible.

Chapter 5: Building up a test bench for calibrating the LPS counter

5.1 Standard practice for OPC calibration: procedure

When referred to an OPC, the term calibration indicates the procedure by which one corrects the output of the OPC under calibration (i.e., particle number concentration and particle size distribution) by using a reference device in parallel. Important parameters are typically the inlet sample flow rate, the particle sizing accuracy, the counting efficiency (the ratio of the output of the device to be calibrated to the one of the reference device), the particle sizing resolution and the zero count rate.

A reference device may be another OPC that has already been calibrated; the reference OPC is usually calibrated against an absolute standard or primary standard. The primary standard is obtained by counting at SEM particle number concentrations of monodisperse spherical particles.

The calibration procedure is carried out by changing or adjusting certain parameters of the OPC's internal circuit (generally voltage values). Typical instrumentation required for an OPC calibration includes: flowmeters, a flow calibrator, an aerosol generator, a filter, an oscilloscope and pulse height analyser or a digital multimeter. In the following a typical calibration procedure is reported step by step (see for example: ASTM F 328-98, 2003 and ISO 21501-4, 2007).

a) Almost all OPCs are equipped with a critical orifice at the inlet, which ensures a fixed sample flow rate, provided the correct pressure drop is guaranteed. The sample flow is usually regulated by a potentiometer governing the voltage output of the OPC pressure transductor. By acting on this potentiometer, the voltage output will change and so will the correct value of the sample flow considered in the particle number concentration calculations.

b) For the determination of the particle sizing accuracy, monodisperse spheres should be generated by the nebuliser with the experimental setup already described in Chapter 4. The voltage pulses caused by the particle signal should then be observed by means of an

oscilloscope, recorded and averaged by means of a pulse height analyser so that a mean voltage value for the given particle size can be achieved. The operation should be repeated for monodisperse spheres of several sizes, so that a calibration curve (voltage output against particle size) is achieved; adjustments to the voltage output should be applied in accordance with the output of the reference device. Results should be compared with the data from the most recent calibration: if differences between old and new data are significant, remedial measures should be taken.

c) The zero count rate of an OPC is determined by connecting an absolute filter to the OPC's inlet. Data have to be collected cumulatively for a certain period and then compared with the zero count rate reported by the manufacturer or by data from the most recent calibration. Remedial measures should be taken in case differences are significant.

d) The counting efficiency is found by generating monodisperse spheres of size equal to the border of a bin and the output is compared with the one of a reference device. The operation should be repeated for all borders of all bins; remedial measures should be taken if differences between the device to be calibrated and the reference one are significant.

In this study, the procedures for the calibration of the LPS were developed and used. The calibration of the inlet sample flow was fully performed and the counting efficiency was adjusted. The determination of the particle sizing accuracy is only meaningful if the instrument to be calibrated can distinguish several size intervals over a wide size range (see for example the size bins of the GRM or the COPC in Table 3.2 and 3.4 respectively). As the LPS has two channels only, step b) was not performed. Results are shown in the following.

5.2 Experimental part

In order to proceed with the calibration procedure of the LPS, the cover of the OPC had to be removed. In this way the LPS's internal circuit could be observed. In the following, details on the calibration of the inlet sample flow and the counting efficiency are exposed.

5.2.1 Flow calibration

The flow calibration procedure consists of two steps: a) adjustment of the appropriate potentiometer voltage and b) measurement of the sample flow.

a) Adjustment of the potentiometer voltage.

This operation was performed in accordance with the Laser Particle Sensor Calibration Manual. The metal shell covering the optic and the electronic components of the LPS was removed, while the instrument was let sample the ambient air. By connecting the test leads of a digital multimeter (Wavetek, mod. 23XT) to the test points identified as TP GND, TP3 and TP4, the voltage between TP GND and TP3 (hereafter V_3) and the one between TP GND and TP4 (hereafter V_4) were measured. Figure 5.1 shows the location of the test points used in this occasion and the potentiometers used in the steps afterwards.

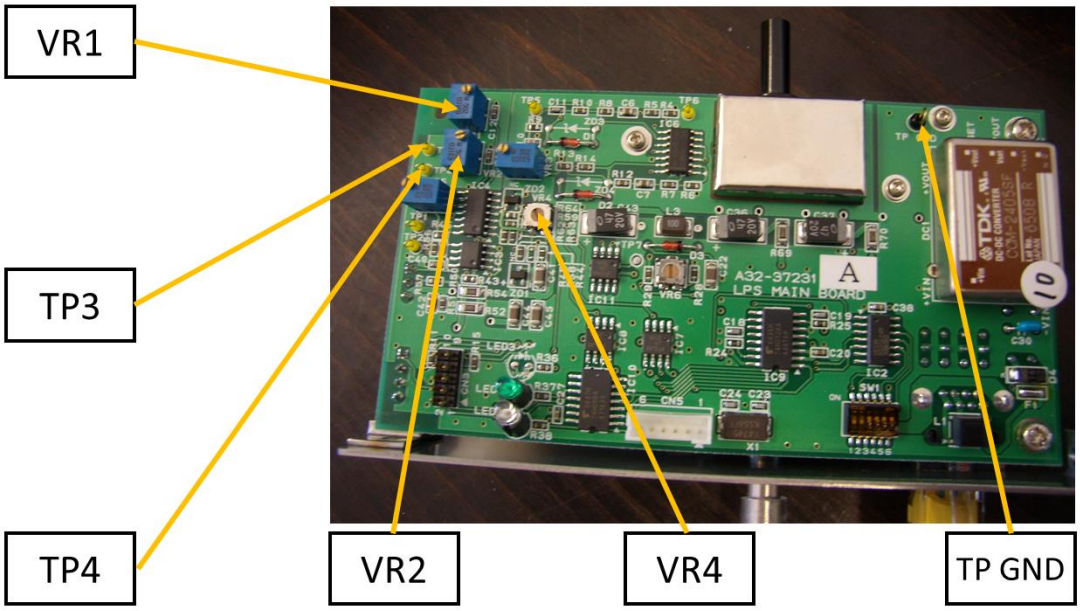

Figure 5.1: Electronic components of the Laser Particle Sensor mod. 3715-00; the test points (TP3, TP4 and TP GND) and the potentiometers (VR1, VR2 and VR4) utilised during the calibration of this OPC are indicated by the arrows.

Before delving into the voltage outputs, the sample flow rate of the LPS was previously measured by means of a flow meter and the recorded value was found to be slightly smaller than 2.83 L min^{-1}, i.e. the value reported by the manufacturer. Afterwards V_3 and V_4 were measured and observed to be 1.14 V and 1.32 V respectively. As prescribed by the instrument's calibration manual, the relationship between V_3 and V_4 should be:

$$V_3 = \frac{V_4}{0.85}$$

Equation 5.1

To satisfy this relationship, the correct value for V_4 should be 1.34 V. The appropriate potentiometer (VR4 in Figure 5.1) was then screwed in order to achieve V_4 = 1.34 V.

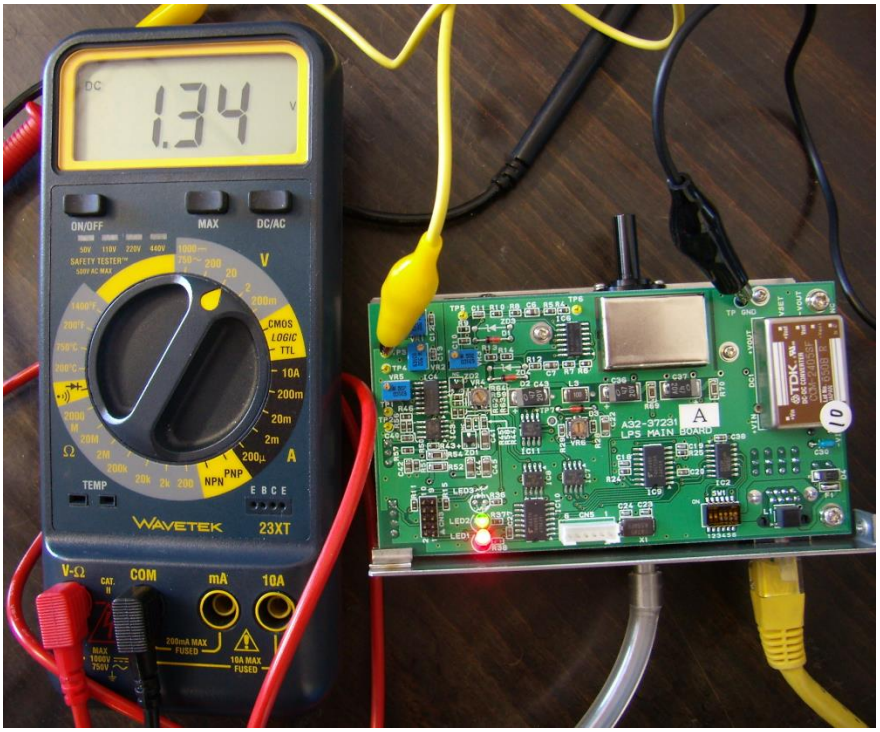

Figure 5.2: Measuring the voltage between TP3 and TP GND (V_3), here indicating V_3 = 1.34 V.

b) Measurement of the sample flow

After screwing the VR4 potentiometer, the flow of the LPS was measured by means of a bubble flow calibrator (mini-BUCK mod. M-5, A. P. Buck Inc.). The LPS was switched on and let measure ambient particulate concentration, while the flow calibrator was connected at the OPC's sample inlet. Twelve measurements of the sample flow were performed (as an example, see Figure 5.3); the value of each measurement was recorded, the mean value was found and the error σ_{sf} was calculated through the following formula:

$$\sigma_{sf} = \frac{\sigma_{dev}}{\sqrt{N}}$$

Equation 5.2

where σ_{dev} is the standard deviation of the distribution achieved with the measurements and N is the total number of measurements (in this case N = 12). Table 5.1 reports details on measurements of the LPS's sample flow after the calibration. The average flow was found to be (2836 $\pm$ 2) cc min^{-1}, in good accordance with the value reported by the producer, i.e. (2.83 $\pm$ 0.14) L min^{-1}. The latter value was therefore retained as correct and no corrections on the previous measurements of particle number concentrations were made.

Figure 5.3: Laser Particle Sensor mod. 3715-00 connected to mini-BUCK calibrator mod. M-5, here indicating a sample flow rate of 2823 cc min^{-1}.

Measure number	Flow rate [cc min^{-1}]
1	2823
2	2833
3	2833
4	2836
5	2835
6	2831
7	2844
8	2841
9	2840
10	2849
11	2833
12	2833
Total	2836 $\pm$ 2

Table 5.1: LPS's sample flow rate after the calibration: details on the single measurements.

5.2.2 Counting efficiency

The LPS mod. 3715-00 has two channels: one for particles of sizes between 0.5 and 5 µm and another for particles greater than 5 µm. The internal circuit analyses the shape and the amplitude of each pulse caused by a particle's passage. A particular pin transforms each pulse into a square wave and based on the height of each square wave a particle is classified and counted in the first or the second channel.

As prescribed by the instrument's calibration manual, the voltage response to a particle passage should be found in the pins reported in Figure 5.4; a number was assigned to each pin, which is reported in the same figure.

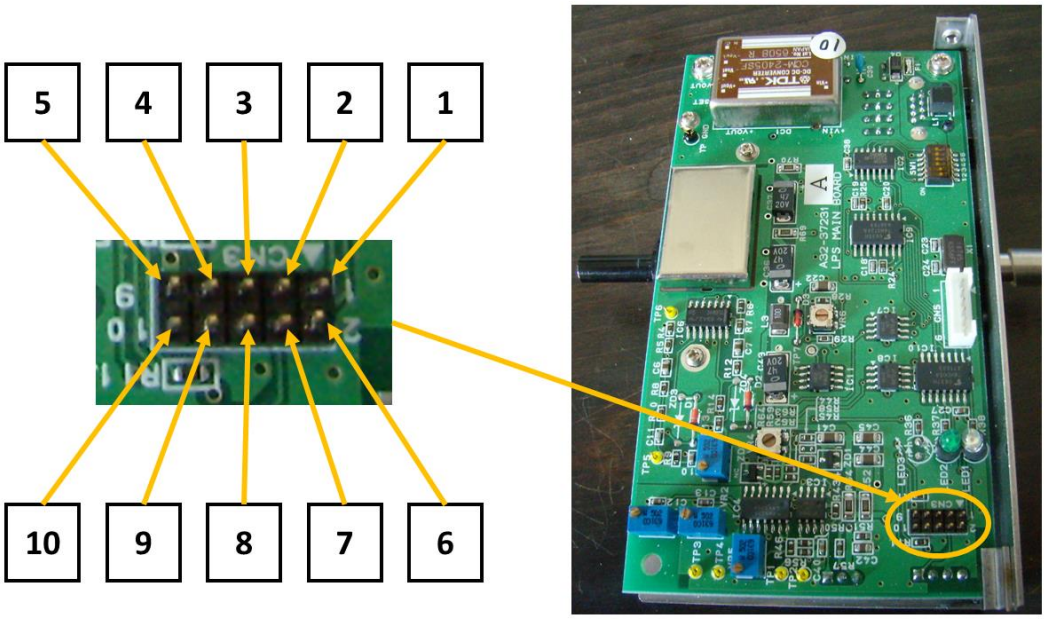

Figure 5.4: Particular of the LPS's internal circuit: pins.

The task of each pin was then identified after connecting them to TP GND and observing the output voltage by means of an oscilloscope; the functions of each pin are summarised Table 5.2. Particle passages are recorded by Pin 9, while Pin 1 reports square waves with equal amplitude, each of which likely indicates one count. Pin 3, Pin 4, Pin 5, Pin 6, Pin 7 and Pin 10 do not report significant output.

The voltage outputs of Pin 2 and Pin 8 are governed by acting on the VR1 and VR2 potentiometers (see Figure 5.1) respectively. Pin 2 regulates the voltage threshold governing the counts of particles in the 0.5-5 µm size range ("small threshold"), while

Pin 8 regulates the voltage threshold governing the counts of particles greater than 5 μm ("large threshold").

Pin	Voltage output	Notes
1	Max. 0.05 V	Square waves
2	Max. 3 V	Depending on VR1("small threshold)
3	0 V	
4	0 V	
5	0 V	
6	0 V	
7	4.54 V	
8	Max. 3 V	Depending on VR2 ("large threshold")
9	Max. 0.42 V	Pulses of different shapes
10	0 V	

Table 5.2: Voltage output and notes of each pin. Pin 9 reports the voltage output due to a particle's passage. After the signal is analysed a count is added and reported by a square wave in Pin 1. Pin 2 and Pin 8 are regulated by the VR1 and VR2 potentiometers respectively and govern the thresholds relating to the counting of particles in the 0.5-5 μm size range and particles greater than 5 μm respectively.

Before generating the test aerosol, the zero count rate of the LPS was checked: the sample inlet of the OPC was connected to an absolute filter and the output was recorded for about 10 minutes. During this period, one particle in 5 minutes was observed, which is in accordance to the ISO 21501-4 (2007) regulation.

The calibration of the counting efficiency of the LPS was carried out for the 0.5-5 μm channel: monodisperse PSL spheres of 0.5 μm were generated by means of the AGK 2000 generator with the experimental setup described in Figure 4.10. As reference device, another LPS already calibrated provided by Pollution Clean Air Systems S.p.A. was used. While producing the test aerosol, the particle number concentration reported by the device to be calibrated was varied by acting on the VR1 potentiometer and the voltage output relating to Pin 2 (V_{PIN2}) was recorded by means of a digital multimeter (Fluke, mod. 187), which can measure the millivolt (mV) scale. For each value of V_{PIN2} data from the reference device and the device to be calibrated were recorded for about 1 min and finally averaged. A picture of the experimental setup is shown in Figure 5.5.

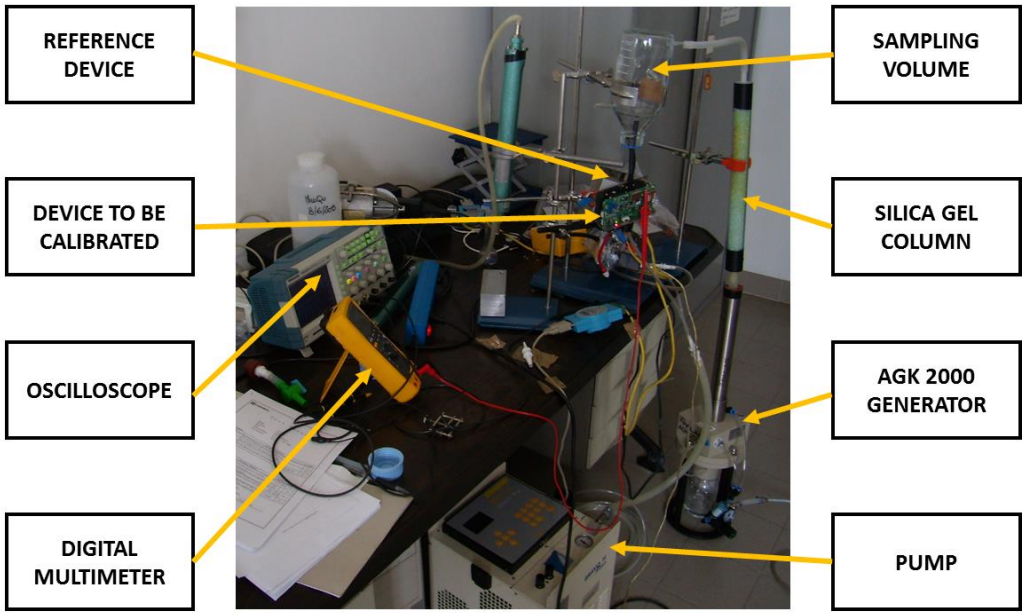

Figure 5.5: Experimental setup for the calibration of the LPS's counting efficiency. The test aerosol (PSL spheres of 0.5 µm in diameter) was produced by the AGK 2000 generator and conveyed towards the sampling volume, where the reference device and the one under calibration measured the particle number concentrations. The digital multimeter measured the V_{PIN2} voltage, which is governed by the VR1 potentiometer (see Figure 5.1).

Initially, V_{PIN2} was found to be 1.996 V and the counting efficiency was observed to be about 150%. By increasing V_{PIN2}, the instrument to be calibrated was observed to measure smaller particle number concentrations, i.e. the counting efficiency was observed to decrease; by varying V_{PIN2} a plot of V_{PIN2} as a function of the counting efficiency could be achieved. This plot is reported in Figure 5.6 and clearly shows that a linear relationship exists between V_{PIN2} and the counting efficiency, as confirmed by the value of the Pearson product-moment correlation coefficient (R^2 = 0.98). By indicating V_{PIN2} with **y** and the counting efficiency with **x**, this experimental relationship is given by:

$$y = a + b * x$$

Equation 5.3

with a = 6887.3 mV and b = -34.3 mV*(counting efficiency)$^{-1}$. To have the same particle counts from both instruments, in Equation 5.3 **x** = 100% should be entered, which yields V_{PIN2} = 3.460 V.

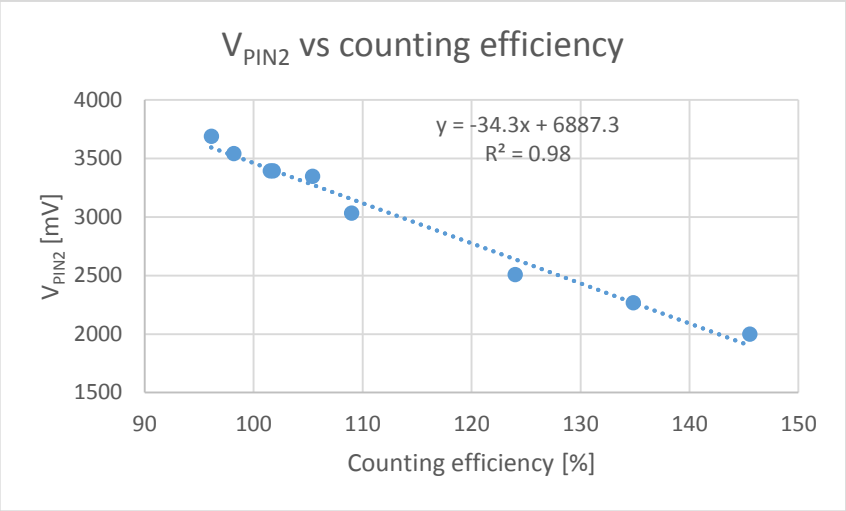

Figure 5.6: Plot of the counting efficiency against V_{PIN2} for the 0.5-5 µm size range while generating 0.5µm PSL spheres. The counting efficiency increases with decreasing VPIN2; by setting counting efficiency = 100%, V_{PIN2} = 3.46 V is found.

5.3 Conclusions

In this chapter results relating to the calibration procedure of the LPS were reported. Namely, this procedure involved the adjustment of the inlet sample flow rate and the calibration of the counting efficiency. Initially, it was observed that the sample flow rate was fairly similar to the manufacture's value; however, after a little voltage adjustment the correct value prescribed by the instrument's user manual (2.83 L min^{-1}) was found. The counting efficiency was found to be different from the one reported by the reference OPC. By increasing the appropriate potentiometer voltage (V_{PIN2}), the LPS device to be calibrated was observed to measure smaller particle number concentrations, yielding that the counting efficiency would decrease with increasing V_{PIN2}. Measurements of particle number concentrations of monodisperse PSL spheres of 0.5 µm in diameter and output values from both the reference device and the OPC to be calibrated were taken and averaged over 1 min. A plot of V_{PIN2} as a function of the counting efficiency was achieved and a linear relationship between the two was observed to exist. From this relationship, a value of 100% for the counting efficiency was found for V_{PIN2} = 3.460 V.

After this procedure, the calibration of the LPS was completed.

Conclusions

Aerosols play an important role in most of the atmospheric processes, thus affecting the Earth's climate and human health with decreases in life expectancy. Therefore, it is of primary importance to be able to monitor aerosol concentrations and size distributions on a real-time basis.

Optical particle counters (OPC) are widely used to measure real time concentrations and size distributions of particulate matter. They are deployed for monitoring outdoor and indoor ambient air, identifying pollution sources and predicting urban air quality. Progresses in technique have very recently allowed the commercialisation of smaller, cheaper and portable OPCs, which are therefore well suited for personal exposure assessment to airborne particles or for distributed sensor network (e.g. participatory environmental monitoring programs).

In this work, an experimental setup was built up to characterise the performances of a new, compact and cheap OPC (CompactOPC N1, produced by Alphasense; hereafter COPC) in terms of sizing accuracy and counting efficiency. This setup involved a traditional OPC used in clean air monitoring activities (Portable Laser Aerosolspectrometer Dust Monitor Model 1.108, produced by GRIMM AEROSOL Technik GmbH & Co.; hereafter GRM), another OPC used in clean room monitoring (Laser Particle Sensor, produced by Kanomax; hereafter LPS) and the generation of monodisperse aerosol. In addition, the experimental circuit allowed the aerosol sampling on absolute filters (Nuclepore) for offline SEM observations, which gave a reference particle number concentration value.

Tests with both indoor and calibrated monodisperse spherical polystyrene (PSL) particles were carried out. PSL particles were produced by means of an ultrasonic nebuliser used for health purposes (Projet, Artsana) and a commercial pressure atomiser (AGK 2000, Palas). A good agreement was found between the concentrations measured by the GRM and the ones obtained from particle counting analysis at SEM, ensuring a good reliability of the experimental setup and the GRM performances.

Results showed that the LPS always overestimated the GRM's output in the 0.5-5 μm size range: the normalised ratio of the concentration read out from the LPS to the one read out from the GRM was on average 1.49.

The reverse was true for the COPC, which always underestimated the particle number concentration with respect to the GRM. Most important, the performances of the COPC depended on its sampling configuration. By considering the normalised ratio of the COPC's output to the GRM one (hereafter COPC/GRM ratio), when both the COPC and the GRM drew air from a closed sampling volume, this value was found to be around 0.2; when directly sampling the indoor air, the COPC/GRM ratio oscillated between 0.2 and 0.4.

A critical aspect of the COPC was therefore the inlet sample flow rate, which was obtained with a fan instead of a sampling pump. Better sampling efficiency values were obtained by sealing the COPC into a plastic bag and connecting it to a pump with a flow rate equals to the COPC's manufactured one (0.2 L min^{-1}). This configuration appeared to return the best performances, as the COPC/GRM ratio was found to be 0.66.

The sizing accuracy of the COPC was found to be very good, as confirmed by the high linear correlation between the COPC's and the GRM's output (R^2 = 0.93 and 0.97). In addition, the particle concentration peaks were always found in the expected channel size bins according to the PSL particle diameters. Finally, it was noticed that the COPC overestimated the particle number concentrations, with respect to the GRM outputs, for particle sizes greater than 1 μm.

In conclusion, the correlation between the COPC and the GRM and the sizing accuracy of the COPC might allow for deploying this OPC as low-cost personal monitoring equipment for measurements of PM concentrations, as long as the COPC is connected to a pump with a stable flow rate of 0.2 L min^{-1}. According to this study, for correct PM estimates, results should be divided by a normalised conversion factor of 0.66.

The same experimental set up was also deployed for the calibration of the LPS according to the ISO 21501-4 (2007) regulation. To this purpose, the flow rate was measured by means of a bubble flow calibrator and adjusted by acting on the appropriate potentiometer in the LPS's internal circuit as prescribed by the instrument manual.

The counting efficiency of the LPS was calibrated against the output of another LPS device already calibrated (golden instrument). When both devices were exposed to 0.5 μm PSL monodisperse particles, the counts in the 0.5-5 μm channel of the LPS were adjusted by acting on the appropriate potentiometer in order to achieve a counting efficiency of 100%.

List of acronyms

ACGIH: American conference of governmental industrial hygienists

CAFE: Clean Air For Europe

CPC: condensation particle counter

CMD: count median diameter

COPC: CompactOPC N1

DMA: differential mobility analyser

DMPS: differential mobility particle sizer

DMS: dimethylsulphyde

GRM: Portable Laser Aerosolspectrometer Dust Monitor Model 1.108

GmbH: Gesellschaft mit beschränkter Haftung, i.e. limited liability company

Inc.: Incorporated

IPCC: Intergovernmental Panel for Climate Change

LPS: Laser Particle Sensor Model 3715-00

LW: long wave

MSA: methanesulphonic acid

NAAQS: National Ambient Air Quality Standards

OPC: optical particle counter

PBAP: primary biological aerosol particles

PM: particulate matter

PSL: polystyrene latex

SEM: scanning electron microscope

SMPS: scanning mobility particle sizer

S.p.a: società per azioni, i.e. joint-stock company

Srl: Società a responsabilità limitata, i.e. same as GmbH

SW: short wave

TEM: transmission electron microscope

TOA: top of the atmosphere

US EPA: United States Environmental Protection Agency

VOC: volatile organic compound

Bibliography

Abdullahi K. L., Delgado-Saborit J. M. and Harrison R. M. (2013): Emissions and indoor concentrations of particulate matter and its specific chemical components from cooking: A review. *Atm. Envir.*, **71**, 260-294.

Air Quality Standards. Available at http://ec.europa.eu/environment/air/quality/standards.htm

Andreae M. O. and Rosenfeld D. (2008): Aerosol–cloud precipitation interactions. Part 1. The nature and sources of cloud active aerosols. *Earth Science Revision*, **89**, 13–41.

Aphekom. Improving Knowledge and Communication for Decision Making on Air Pollution and Health in Europe. Summary report of the Aphekom project 2008-2011 (2011). Available at: http://aphekom.org/c/document_library/get_file?uuid=5532fafa-921f-4ab1-9ed9-c0148f7da36a&groupId=10347

ASTM F 328-98 (2003) "Standard Practice for Calibration of an Airborne Particle Counter Using Monodisperse Spherical Particles".

Belosi F., Santachiara G. and Prodi F. (2011): Eyjafjallajökull Volcanic Eruption: Ice Nuclei and Particle Characterization. *Atmos. Clim. Sci*., **1**, 48-54.

CAFE: Clean Air For Europe - Working Group on Particulate Matter (2005): Second Position Paper on Particulate Matter. Available at: http://ec.europa.eu/environment/archives/cafe/pdf

Chen B., Kitagawa H., Hu K., Jie D., Yang J. and Li J. (2008): Element and mineral characterization of dust emission from the saline land at Songnen Plain, Northeastern China. *J. Environ. Sci. (China)*, **21**(10), 1363-70.

Colombi C., Gianelle V., Lazzarini M. and Angius S. (2012): Optical Particle Counters: dalla teoria alle applicazioni. Quinto convegno nazionale sul particolato atmosferico. Italian Aerosol Society.

Colombi C., Angius S., Gianelle V. and Lazzarini M. (2013): Particulate matter concentrations, physical characteristiscs and elemental composition in the Milan underground transport system. *Atm. Envir.*, **70**, 166-178.

Daisey J. M. and Gundel L. A. (1991): Tracing the Sources of Indoor Aerosol Using Evolved Gas Analysis. *Aerosol Sci. Technol.*, **14**, 25-32.

European Standard (2014): Ambient air – Standard gravimetric measurement method for the determination of the PM10 or PM2.5 mass concentration of suspended particulate matter. Available at: http://www.sipe-rtd.info/directive/

Fang G. C., Chang C. N., Wu Y. S., Fu P. P. C., Yang D. G. and Chu C. C. (1999): Characterization of chemical species in PM2.5 and PM10 aerosols in suburban and rural sites of central Taiwan. *Sci. Total Environ.*, **234**, 203-212.

Fowler D., Brunekreef B., Fuzzi S., Monks P. S., Sutton M. A., Brasseur G. P., Friedrich R., Passante L. G. and Jiménez Domingo J. M. (2012): Air Quality – Research Findings in support of the EU (review). ACCENT Plus.

Fuchs N. A. (1973): Latex Aerosols – Caution! *J. Aerosol Sci.*, **4**, 405-410.

Fuzzi S., Baltensperger U., Carslaw K., Decesari S., Denier van der Gon H., Facchini M. C., Fowler D., Koren I., Langford B., Lohmann U.,Nemitz E., Pandis S., Riipinen I., Rudich Y., Schaap M., Slowik J., Spracklen D. V., Vignati E., Wild M., Williams M. and Gilardoni S. (2015): Particulate matter, air quality and climate: lessons learned and future needs, *Atmos. Chem. Phys. Discuss.*, **15**, 521-744, doi: 10.5194/acpd-15-521-2015.

Ginoux P., Prospero J. M., Gill T. E., Hsu N. C. and Zhao M. (2012): Global scale attribution of anthropogenic and natural dust sources and their emission rates based on MODIS Deep Blue aerosol products. *Rev. Geophys.*, **50**, RG3005, doi: 10.1029/2012RG000388.

Giechaskiel B., Maricq M., Ntziachristos L., Dardiotis Ch., Wang X., Axmann H., Bergmann A. and Schindler W. (2014): Review of motor vehicle particulate emissions, sampling and measurement: From smoke and filter mass to particle number. *J. Aerosol Sci.*, **67**, 48-86.

Griffiths W. D., Mark D., Marshall I. A. and Nichols A. L. (1998): Aerosol particle size analysis: Good Calibration Practises. The Royal Society of Chemistry. ISBN 0-8504-452-3.

Guide to the Demontration of Equivalence of Ambient Air Monitoring Methods (2010): Report by an EC Working Group on Guidance for the Demonstration of Equivalence. Available at: http://ec.europa.eu/environment/air/quality/legislation/

Hetland R. B., Refsnes M., Myran T., Johansen B. V., Uthus N. and Schwarze P. E. (2000): Mineral and/or metal content as critical determinants of particle-induced release of IL-6 and IL-8 from A549 cells. *J. Toxicol. Env. Heal. A*, **60**, 47-65.

Hinds W. C. (1999): Aerosol Technology: Properties, Behavior, and Measurement of Airborne Particles, 2nd Edition. Wiley, ISBN: 978-0-471-19410-1.

Heim H., Mullins B. J., Umhauer H. and Kasper G. (2008): Performance evaluation of three optical particle counters with an efficient "multimodal" calibration method. *J. Aerosol Sci.*, **39**, 1019-1031.

Intergovernmental Panel for Climate Change (IPCC), 5th Assessment Report (2013). Summary for Policy Makers.

ISO 21501-4 (2007): Determination of particle size distribution – Single particle light interaction methods. Part 4: Light scattering airborne particle counter for clean spaces. TSI.

Junge C. (1955): The size distribution and aging of natural aerosols as determined from electrical and optical data on the atmosphere. *J. Meteor.*, **12**, 13-25.

Koelemeijer R., Homan C. and Matthijsen J. (2006): Comparison of spatial and temporal variations of aerosol optical thickness and particulate matter over Europe. *Atmos. Environ.*, **40**, 5304–5315.

Laser Particle Sensor Calibration Manual – Vers. 1.00 - Kanomax Japan, Inc.

Laser Particle Sensor – Modello 3714-00/-01 3715-00/-01 - Manuale di Istruzioni – Pollution Srl.

Liu B. Y. H. (1976): Fine Particles. Aerosol Generation, Measurement, Sampling and Analysis. Academic Press Inc.

Monks P. S., Granier C., Fuzzi S., Stohl A., Williams M. L., Akimoto H., Amann A., Baklanov A., Baltensperger U., Bey I., Blake N., Blake R. S., Carslaw K., Cooper O. R., Dentener F., Fowler D., Fragkou E., Frost G. J., Generoso S., Ginoux P., Grewe V., Guenther A., Hansson H. C., Henne S., Hjorth J., Hofzumahaus A., Huntrieser H., Isaksen I. S. A., Jenkin M. E., Kaiser J., Kanakidou M., Klimont Z., Kulmala M., Laj P., Lawrence M. G., Lee J. D., Liousse C., Maione M., McFiggans G., Metzger A., Mieville A., Moussiopoulos N., Orlando J. J., O'Dowd C. D., Palmer, Parrish D. D., Petzold A., Platt U., Pöschl U., Prévot A. S. H., Reeves C. E., Reimann S., Rudich Y., Sellegri K., Steinbrecher R., Simpson D., ten Brink H., Theloke J., van der Werf G. R., Vautard R., Vestreng V., Vlachokostas Ch. and von Glasow R. (2008): Atmospheric composition change – global and regional air quality, *Atmos. Envir.*, **43**, 5268-5350.

National Ambient Air Quality Standards (NAAQS). Available at http://www.epa.gov/air/criteria.html

Obersdörster G., Obersdörster E. and Obersdörster J. (2005): Nanotoxicology: An Emerging Discipline Evolving from Studies of Ultrafine Particles. *Environ Health Perspect.*, **113**(7): 823–839, doi: 10.1289/ehp.7339.

Park J. Y., McMurry P. H. and Park K. (2012): Production of Residue-Free Nanoparticles by Atomization of Aqueous Solutions. *Aerosol Sci. Technol*., **46**(3), 354-360.

Pastuszka J. S., Kyaw Tha Paw U., Lis D. O., Wlazło A. and Ulfig K. (2000): Bacterial and fungal aerosol in indoor environment in Upper Silesia, Poland. *Atm. Envir*., **34**, 3833-3842.

Pope C. A. and Dockery D. W. (2006): Health Effects of Fine Particulate Air Pollution: Lines that Connect. *J. Air Waste Manage. Assoc.*, **56**, 709-742.

Putaud J.-P. (2003): A European Aerosol Phenomenology: physical and chemical characteristics of particulate matter at kerbside, urban, rural and background sites in Europe. EUR 20411 EN.

Quinn P. K. and Bates T. S. (2011): The case against climate regulation via oceanic phytoplankton sulphur emissions. *Nature*, **480**, 51–56, doi: 10.1038/nature10580.

Raabe O. G. (1968): The Dilution of Monodisperse Suspensions for Aerosolization. *Am. Ind. Hyg. Assoc. J*., **29**(5), 439-443.

Reşitoğlu İ. and Altinişik K. (2015): The pollutant emissions from diesel-engine vehicles and exhaust after treatment systems. *Clean Techn. Environ. Policy*, **17**, 15-27.

Rodriguez S., Querol X., Alastuey A., Kallos G. and Kakaliagou O. (2001): Saharan dust contributions to PM10 and TSP levels in Southern and Eastern Spain. *Atm. Envir*., **35**, 2433-2447.

Schleicher N., Kramar U., Dietze V., Kaminski U. and Norra S. (2010): Geochemical characterization of single atmospheric particles from the Eyjafjallajökull volcano eruption event collected at ground-based sampling sites in Germany. *Atm. Environ*., **48**, 113-121.

Stothers R. B. (1984): The Great Tambora Eruption in 1815 and Its Aftermath. *Science*, **224**, nr. 4654.

Szidat S., Jenk T. M., Synal H.-A., Kalberer M., Wacker L., Hajdas I., Kasper-Giebl A. and Baltensperger U. (2006): Contributions of fossil fuel, biomass-burning, and biogenic emissions to carbonaceous aerosols in Zurich as traced by ^{14}C. *J. Geophys. Res.*, **111**, doi: 10.1029/2005JD006590.

Tan C. C. L., Finney K. N., Chen Q., Russell N. V., Sharifi V. N. and Swithenbank J. (2012): Experimental investigation of indoor air pollutants in residential buildings. *Indoor Built Environ.*

United States Environmental Protection Agency (US EPA). Link: http://www.epa.gov/

Valavanidis A., Fiotakis K. and Vlachogianni Th. (2008): Airborne Particulate Matter and Human Health: Toxicological Assessment and Importance of Size and Composition of Particles for Oxidative Damage and Carcinogenic Mechanisms. *J. Envir. Sci. Health. Part C*, **26**, 339-362.

Vincent J. H. (1989): Aerosol Sampling Science and Practice. John Wiley & Sons Ltd.

Wang S., Ang H. M. and Tade M. O. (2007): Volatile organic compounds in indoor environment and photocatalytic oxidation: State of the art. *Environ. Int.*, **33**, 694–705.

Wang Y., Keun-Hee L., Lin Y., Levy M. and Zhang R. (2013): Distinct effects of anthropogenic aerosols on tropical cyclones. *Nat. Clim. Chang*., **4**, 368-373, doi: 10.1038/NCLIMATE2144.

Acknowledgements

This work would have not been possible without the help provided by: Prof Vincenzo Levizzani (supervisor), Dr Franco Belosi (co-supervisor), Dr Fabrizio Ravegnani (co-supervisor), Dr Gianni Santachiara and Alessia Nicosia. I am thankful to each of them for being always available and patient during the carrying out and the writing of this work.
I am particularly thankful to Pollution Clean Air Systems S.p.A. for providing the two LPS devices, without which a significant part of this work could not have been performed.